Title

ANALYSIS OF IRON FLUORESCENCE FROM VACUUM ULTRA VIOLET PHOTOLYSIS OF IRON PENTACARBONYL

Author

Horak, D.V.

Publication Date

1982-07-01

Lawrence Berkeley Laboratory
UNIVERSITY OF CALIFORNIA

Materials & Molecular Research Division

ANALYSIS OF IRON FLUORESCENCE FROM VACUUM ULTRA VIOLET PHOTOLYSIS OF IRON PENTACARBONYL

David Václav Horák
(Ph.D. thesis)

July 1982

Prepared for the U.S. Department of Energy under Contract DE-AC03-76SF00098

DISCLAIMER

Analysis of Iron Fluorescence from Vacuum Ultra Violet Photolysis of Iron Pentacarbonyl

David Václav Horák

Materials and Molecular Research Division
Lawrence Berkeley Laboratory

and

Department of Chemistry
University of California
Berkeley, CA 94720

ABSTRACT

A quantitative study of the fluorescence and photoionization yields from the VUV photolysis of $Fe(CO)_5$ in a semi-effusive beam was carried out and compared favorably with a limited degree of freedom statistical dissociation model over the 10 to 14 eV range of excitation energies. At 1170 Å the branching ratio between fluorescence and neutral production was computed to be 1.33×10^{-4}, and the branching ratio between ionization and neutral production was determined to lie between 0.0048 and 0.0024. The absorption cross-section at 1170 Å was measured to be 1.3 ± 0.2 Å^2. The cross-section for neutral production was 1.3 ± 0.2 Å^2; for ionization, between 0.006 and 0.003 Å^2; and for fluorescence, $1.7 \pm 0.3 \times 10^{-4}$ Å^2. By comparing experimental data to the model, the total metal-ligand bond dissociation energy of $Fe(CO)_5$ was determined to be 6.10 ± 0.05 eV.

ACKNOWLEDGMENTS

First of all, I would like to thank John S. Winn, my research director, for his support and assistance in my research. 'Thank you' seems too weak a word to offer for his help in editing my thesis. Perhaps, perseverance beyond the call of duty can begin to suffice. I award John the purple heart in the battle, not with my English, but with my lack of it. (Sue and Will are granted each a purple atrium and Professor John Clark, two purple ventricles). My association with John also helped me to realize the importance of being a person first, then a scientist, a concept which is sometimes lost in the scientific community.

I would like to thank the other members of my research group, past and present, for numerous interesting discussions: some about science, some not; some over brews, some not. Making their acquaintance has certainly added color to my stay at Berkeley.

I would like to thank the support staff of U. C. Berkeley Chemistry Department, especially the machine and electronics shops. Charley, George, Bob the welder, Andy, Fred, Bob not the welder, Carl, Chuck, Clay, and Howard of the machine shop not only did excellent work, but also patiently discussed with me my designs. The assistance Don, Steve, and Henry in the electronics shop offered was also second to none and their pet intensive care unit was greatly appreciated. Beyond their technical expertise, they all are a hell of a bunch of guys.

I would like to thank Mike Maier for sharing his thoughts on a wide variety of subjects. His views, often hybrids of science, philosophy and common sense were usually distinctive, sometimes surprising and were always heard with great interest.

I would like to thank Lois for making the bad times at Berkeley bearable and the good times as good as they could be.

Last and most of all I want to thank my parents whose encouragement, guidance and a very painful decision in August 1968 allowed me to get this degree.

This work was supported by the Director, Office of Energy Research, Office of Basic Energy Sciences, Chemical Sciences Division of the U. S. Department of Energy under Contract No. DE-AC03-76SF00098.

TABLE OF CONTENTS

TABLE OF CONTENTS (continued)

CHAPTER I

INTRODUCTION

Transition metal carbonyls have been providing chemists with interesting problems and important chemical information for many years. It has long been recognized that the relatively high vapor pressure of metal carbonyls, much greater than that of the pure parent metal at the same temperature,[1] could facilitate the study of metal chemistry at moderate temperatures. Most recently, numerous studies have documented the catalytic properties of metal carbonyls,[2] have revealed analogies between the properties of carbon monoxide in metal carbonyls and carbon monoxide chemisorbed on metal surfaces,[3] and have shown that metal carbonyls are useful sources of electronically excited metal atoms.[4-8] These investigations have underlined the utility of metal carbonyls in the study of the chemistry of metals.

One of the first experiments to study the decomposition and fragmentation of metal carbonyls was carried out by Winters and Kiser.[9] They investigated the effect of electron impact on iron pentacarbonyl and nickel tetracarbonyl, determined ion fragmentation patterns of these species as a function of electron energy, and measured the ion fragments' appearance potentials. They also experimentally verified that the CO bonds remain intact during the decomposition process. Subsequent photoionization studies confirmed the results of the electron impact data. In studies of the bond energy of various metal carbonyls,[10] CO-metal bond strengths were found to be slightly higher than earlier thermochemical data suggested.[11] Other photoionization studies[12] have shed light on the importance of backbonding to the electronic structure

of transition metal carbonyls. Recently, the ionization process itself has been probed using multiphoton ionization.[13-16]

Interestingly, the production of electronically excited neutral metal atoms has been a relatively unexplored subject. In an early study, Brennen and Kistiakowski[17] reported the observation of emission from electronically excited transition metal atoms produced by seeding metal carbonyls into an active nitrogen afterglow. They explained their data on the basis of a model in which the metal atom was first liberated by successive carbonyl reactions with nitrogen atoms, and then reacted with an excited nitrogen molecule to yield an electronically excited metal atom. Lee and Zare[18] detected ground state uranium atoms in collisions between uranocene and metastable argon atoms. Fluorescence from electronically excited metal atoms produced in multiphoton dissociation has also been observed.[5]

Hartman and co-workers[6,7,19] have observed chemiluminescence from iron and nickel atoms produced by the collision of iron pentacarbonyl and nickel tetracarbonyl with metastable argon, neon, and helium. The similiarity between iron chemiluminescence and N_2 chemiluminescence as a function of argon metastable concentration, the latter known to occur in a bimolecular fashion, led to the postulation that the former also has a first-order dependence on argon metastable concentration. Since iron chemiluminescence also showed a first-order dependence on iron pentacarbonyl, they proposed an overall bimolecular process. The analysis of atomic emission intensities led to the formulation of a limited degree of freedom statistical dissociation model. This model accurately predicted the observed emission spectra, and assumed a very fast metal-ligand bond rupture leading to radial metal-ligand dissociation. The

model was applied successfully by Kobovitch and Krenos[20] and Snyder et al.[21] to the analysis of the iron chemiluminescence intensities obtained under collisionless conditions in crossed molecular beams of iron pentacarbonyl and argon metastables. It was also determined with finality in the crossed beam experiments that the metal fluorescence observed by Hartman was the result of an elementary bimolecular reaction. Neutral excited metal fluorescence was further observed by Hellner et al.[22] by VUV photolysis of iron pentacarbonyl. Their experiment was limited to a few VUV wavelengths. Unfortunately, their measured emission intensities cannot be considered reliable since they were not corrected for the variation in VUV photon flux and fluorescence collection efficiency caused by metal deposition on optical surfaces.

The experiments which are the subject of this thesis were designed to bridge some of the gaps between the other pieces of data in the sparsely filled mosaic of carbonyl chemistry. Through quantitative photolysis over a wide range of VUV wavelengths, fluorescence and photoionization quantum yields have been obtained. In this thesis the quantitative trends will be compared to the limited degree of freedom dissociation model. The work will compare not only the three product channels (ionization, fluorescence, and nonradiative neutrals) to each other, but it will also compare rare gas metastables and VUV photon induced processes. The quantitative applicability of the dissociation model over a range of excitation energies will be explored.

REFERENCES for CHAPTER I

1. John H. Perry, Chemical Engineers' Handbook (McGraw-Hill Book Co., 1963); F. Rosebury, Handbook of Electron Tube and Vacuum Techniques (Addison-Wesley Publishing Company, Inc., Massachusetts, 1965), pp. 143-8.

2. See for example, J. E. Huheey, Inorganic Chemistry: Principles of Structure and Reactivity, 2nd edition (Harper and Row, New York, 1978), p. 528; Charles L. Thomas, Catalytic Processes and Proven Catalysts (Academic Press, N.Y., 1970), p. 219.

3. E. W. Plummer, W. R. Salaneck, and J. S. Miller, Phys. Rev. B18, 1673 (1978).

4. D. W. Trainer and S. A. Mani, Appl. Phys. Lett. 33, 31 (1978).

5. Z. Karney, R. Naaman, and R. N. Zare, Chem. Phys. Lett. 59, 33 (]978).

6. D. C. Hartman and J. S. Winn, J. Chem. Phys. 68, 2990 (1978).

7. D. C. Hartman, W. E. Hollingsworth, and J. S. Winn, J. Chem. Phys. 72, 833 (1980).

8. A. B. Callear and R. J. Oldman, Trans. Faraday Soc. 63, 2888 (1967); A. B. Callear, Proc. Roy. Soc. A265, 71 (1961).

9. R. E. Winters and R. W. Kiser, Inorg. Chem. 3, 699 (1964).

10. G. Distefano, J. Res. Nat. Bur. Stand. (U.S.) 74A, 233 (1970).

11. F. A. Cotton, A. K. Fischer and G. Wilkinson, J. Am. Chem. Soc. 81, 800 (1959).

12. D. R. Lloyd and E. W. Schlag, Inorg. Chem. 8, 2544 (1969).

13. P. C. Engelking, Chem. Phys. Lett. 74, 207 (1980).

14. S. Leutwyler and U. Even, Chem. Phys. Lett. 84, 188 (1981).

15. D. P. Gerrity, L. J. Rothberg, and V. Vaida, Chem. Phys. Lett. 74, 1 (1980).

16. M. A. Duncan, T. G. Dietz, and R. E. Smalley, Chem. Phys. 44, 415 (1979).

17. W. R. Brennen and G. B. Kistiakowsky, J. Chem. Phys. 44, 2695 (1966).

18. H. U. Lee and R. N. Zare, J. Chem. Phys. 64, 431 (1976).

19. D. C. Hartman, Ph.D. Thesis, University of California, Berkeley, LBL Report 11208 (1980).

20. J. Kobovitch and J. Krenos, J. Chem. Phys. 74, 431 (1981).

21. H. L. Snyder, T. P. Parr, D. H. Parr, B. T. Smith, and R. M. Martin, Chem. Phys. Lett. 73, 487 (1980).

22. L. Hellner, J. Masanet, and C. Vermeil, Nouveau Journal de Chimie, 3, 721 (1979); L. Hellner, J. Masanet, and C. Vermeil, Chem. Phys. Lett. 83, 474 (1981).

CHAPTER II

EXPERIMENTAL APPARATUS

Introduction

The apparatus used to study the vacuum ultra-violet photolysis of iron pentacarbonyl brought together numerous experimental techniques. While none of these was new, the chemical and physical properties of iron pentacarbonyl posed considerable obstacles which had to be surmounted in applying them. The apparatus was a windowless, high intensity source of monochromatic VUV photons crossed at right angles by a semi-effusive beam of iron pentacarbonyl. The resulting atomic iron fluorescence was observed along the third perpendicular axis. The apparatus, schematically shown in Figure II-1, can be divided into six major sections:

A. Vacuum Ultraviolet Light Source

B. Seya-Namioka Vacuum Monochromator

C. Gas Flow Conductance Limiter

D. Interaction Chamber

E. Detection and Experimental Control Electronics

F. Experimental Software

The details of the design and operation of each of these major components will be separately discussed.

A. Vacuum Ultraviolet Light Source

Many light sources have been used in vacuum ultraviolet radiation studies.[1] The choice has depended upon the desired application. The photolysis of iron pentacarbonyl to excited iron atoms required photon

energies ≥9.5 eV. This limit is imposed by summing the six energy values required to liberate the iron from its ligands (~6 eV)[2] and excite it to the first state from which UV fluorescence was observed ($z^5D°$), (~3.2 eV).[3] A cold cathode discharge lamp was chosen because it offered the opportunity to use both the lower intensity hydrogen pseudo-continuum (up to ~14.6 eV) as well as the very intense argon, neon, and helium resonance lines at approximately 11.8, 16.8, and 21 eV, respectively.

The sharp molecular band structure of the hydrogen pseudo-continuum[4] starts at approximately 1670 Å and extends to 850 Å. It has the appearance of a many-line spectrum, which has given rise to the commonly used term 'the many-line molecular hydrogen pseudo-continuum spectrum'. Among these molecular emissions are two strong atomic emissions, the Lyman α and Lyman β lines at 1215 and 1066 Å, respectively. The emission from the cold cathode discharge source used in these studies is shown under high resolution in Figure II-2. The sharp line band structure in the output of the light source did not affect our experiment since we did not require high spectral resolution. The section of the low resolution spectrum used in this experiment, which is much smoother, is shown in Figure II-3. The rare gas discharge produces only one or two lines for each gas in the VUV region of the spectrum. The details of these lines are summarized in Table II-1.

The design of the capillary discharge lamp (Fig. II-4) was the same for all four gases mentioned. The lamp can be discussed in terms of three major sections: the anode, the capillary discharge tube itself, and the cathode.

The design of the anode was patterned after that of Ng.[5] It had an all-aluminum, water-cooled electrode which was mechanically attached

directly to the entrance arm of the monochromator. Even though the anode was at electrical ground, it was insulated from the rest of the apparatus in order to isolate the lamp power supply from the detection electronics. The destructive effect of the discharge on metal surfaces other than those of the lamp was minimized by using a replaceable preslit, a stainless steel disc with a monochromator acceptance angle-matched slit in the center. The preslit served not only to allow all usable light to reach the monochromator, but also to confine the discharge within the cavity. This limited the effect of the discharge on delicate metal assemblies such as conductance limiter and the monochromator slit. To minimize the clogging of the preslit, the discharge gas was introduced inside the anode on the discharge cavity side of the preslit and was continuously pumped through the preslit. The gas flow into the discharge region (diagrammed in Fig. II-5) was controlled by a calibrated needle valve. The discharge gas pressure was monitored by a Varian 531 thermocouple gauge in the region directly behind the preslit well away from the discharge channel.

The quartz discharge capillary was a 6 mm ID x 12" long tube surrounded by a water jacket. These rather large dimensions were chosen to maximize light output, which increases linearly with length and with area. The ends of the discharge tube were connected and sealed to the anode and cathode by two Cajon-type O-ring seal fittings.

The aluminum cathode was made up of two sections, the body and a lid, joined by a Viton O-ring seal. This two-piece construction allowed a very large, easily accessible cathode area. To minimize damage by the discharge, a replaceable aluminum sleeve was press-fit into the body of the discharge cavity. The cathode body was water-cooled through a

rectangular helical groove sealed by a sleeve. The lid was water-cooled through a circular passage. An aluminum support rod and two lighter positioning rods were used to secure the cathode assembly. The assembly was electrically insulated from the rods by Teflon spacers.

The anode was pumped through a conductance limiter and the vacuum monochromator entrance slits by the monochromator diffusion pump, as shown in Figure II-4. The remainder of the lamp vacuum system is shown in Figure II-5. The cathode was pumped through an isolation valve V1 by a Welch 1400 mechanical pump. The valve V1 was adjusted to maximize the light output as measured in the reaction chamber. Operating conditions for all gases used are summarized in Table II-1.

The cathode pressure was monitored by a Varian 531 thermocouple gauge at valve V1. The entire assembly was electrically insulated from the cathode by a 50 cm long section of rubber tubing. All water connections were made with Tygon tubing, which performed well under the intense UV radiation and the moderate pressure of a 2 gal/min flow rate. As a safety measure, a grounded aluminum shield was slipped over the entire assembly to protect the experimenter from electrical shock and sunburn.

The electrical connections to the lamp are also shown in Figure II-5. The power supply was unregulated and was able to supply -1000 VDC at 500 mA. In order to regulate the current through the lamp, forced-air-cooled ballasting resistors were placed in series with the lamp. By shorting selected resistors, a ballast resistance could be selected in 50 ohms steps from 50 to 2950 ohms. Under some conditions when further adjustment in the current was desirable, a Variac was used to control the line voltage to the power supply. Since our unregulated power

supply provided a no-load output in excess of -1600 VDC, which was sufficient to initiate the discharge, a separate starter circuit was unnecessary.

B. Vacuum Ultraviolet Monochromator

The discharge lamp produced a distribution of VUV wavelengths (which depended on the gas). A Jarrell-Ash Model 78660 one meter Seya-Namioka monochromator was used to select a narrow range of excitation wavelengths. Since the monochromator was used with an approximately 10 Å band pass, the limited resolution inherent to the Seya-Namioka design was no shortcoming. To achieve a high throughput, a grating (Bausch and Lomb Model 35-52-25-722, MgF_2 coated, 1200 grooves/mm, 1200 Å blaze angle) with the large ruled area of 96 x 56 mm was used.

In order to minimize scattered light, a single optical baffle was placed close to the grating, masking all but the ruled part of the grating. In the exit arm, a network of baffles were placed to allow only the desired focused image to reach the exit slit.

The monochromator vacuum was maintained by a 4" CVC (700 l/sec) diffusion pump. Freon-cooled baffles were placed between the monochromator and the diffusion pump to protect the grating from backstreaming oil. A background pressure of less than 5×10^{-6} torr, as monitored by an Electron Technology, Inc. ionization gauge (Model 4336P), could be obtained in a sealed monochromator.

A four-way interlock mechanism was designed that would turn off the diffusion pump if unsafe operating conditions were detected. The interlock could not be overridden. Sensors monitored the diffusion pump cooling water flow, the foreline gas pressure, and the diffusion pump and freon baffle temperatures.

Monochromator scanning was accomplished through a sine drive integral to the monochromator which allowed scan speeds of 5 to 2500 Å/min. All scans were carried out in the direction of increasing wavelength.

C. Gas Flow Conductance Limiter

In order to separate the one torr region of the discharge lamp from the 10^{-6} torr region of the monochromator, some type of pressure isolation had to be used. Since no window materials exist that transmit throughout the 1300 to 584 Å region, a conductance limiting device was inserted between the lamp anode and the entrance slit of the monochromator. The shape and position of the conductance limiter are shown in Figure II-6. To aid in the design of this device, an accurate determination of the pumping speed for a 1000 μm wide entrance slit was made using two thermocouple gauges separated by a tube of known conductance. By monitoring the pressure across the tube, a pumping speed of 0.5 l/sec was determined.

The six mm internal height of the conductance limiter was determined by the lamp capillary internal diameter. A 3° wedge was used to match the acceptance angle of the monochromator. The width of the narrow end of the opening was matched to the monochromator entrance slit width (1000 μm). The appropriate length was determined by the conductance necessary to produce the desired pressure drop between the lamp and the monochromator. With a length of one inch, pressures in excess of one torr could be maintained in the lamp, while maintaining the monochromator pressure below 5×10^{-4} torr, well below the pressure that would stall the monochromator diffusion pump.

D. Interaction Chamber

The major constraints on the design of this chamber were:

i) the total isolation of the VUV monochromator from $Fe(CO)_5$ molecules,

ii) a very high density of $Fe(CO)_5$ in the interaction region,

iii) the ability to pump large quantities of $Fe(CO)_5$ without a prolonged down time,

iv) an efficient collection of fluorescent photons, and

v) the ability to monitor the VUV photon flux during the experiment.

The description of the interaction chamber and equipment attached to its ports will be divided into the following sub-sections:

1) Chamber and Pumping,

2) Vacuum Ultraviolet Photon Monitoring,

3) Fluorescence Monitoring,

4) $Fe(CO)_5$ Source and Sink Assembly,

5) $Fe(CO)_5$ Disposal System,

6) Photoionization Detection, and

7) Beam Density Monitoring.

Unless otherwise noted, refer to Figures II-7, II-8, and II-9 for specific details.

1) Chamber and Pumping

The interaction chamber was constructed from one-half inch thick, Type 304 stainless steel plates polished to a 32 μ-inch finish on the inside. These plates were assembled with continuous welds on the inside

and tack welds on the outside. Access inside the interaction chamber was provided by a removable lid and five ports with O-ring seals.

The main pumping system, a CVC four-inch diffusion pump (pumping speed 700 1/sec) backed by a Welch 1402 mechanical pump, was attached to the bottom port. Liquid nitrogen cooled chevron baffles were placed between the chamber and the DP. The entire pumping system could be isolated from the interaction chamber by a gate valve. A background pressure of 2×10^{-6} torr, as measured by an Electron Technology, Inc., VG1B/2 ionization gauge could routinely be achieved. A Varian 531 thermocouple gauge was used to monitor higher pressures. Both gauges could be isolated from the main chamber by a valve. The power to the diffusion pump was controlled by an interlock system which would turn off the power if the foreline pressure, as monitored by another Varian 531 thermocouple gauge, rose too high, if the DP cooling water flow was too low, or if the DP temperature was too high.

Each of the four vertical sides of the chamber contained one major port. The exit arm of the VUV monochromator was mounted to the chamber at one port. Alignment between the two was insured by guide pins, and they were held together through a collar, shaft and bolt assembly. An O-ring in the chamber wall facilitated the vacuum seal between the chamber and the exit arm. A gate valve was provided on the inside of the chamber wall facing the monochromator, allowing the interaction chamber to be vented without affecting the monochromator vacuum. Of the three remaining side ports, one was for fluorescence observation, a second for monitoring the VUV photon flux with a scintillator, and the third for a window used in beam density measurements. Each will be discussed in detail separately.

2) Vacuum Ultraviolet Photon Monitoring

Various modes of interaction between radiation and matter provide the underlying principles for all photon detectors. For vacuum UV photons, these interactions involve the photoionization of gases, photoconductivity, the ejection of photoelectrons from metals, thermal effects, fluorescence, and chemical changes. The fluorescence technique was concluded to be the most practical for our application. This technique combined the use of a scintillating target and a photomultiplier. Since continuous monitoring of the VUV light was necessary, the scintillator-photomultiplier assembly, shown in Figure II-10, was placed on the port opposite the monochromator.

Sodium salicylate scintillating material was used for both its photochemical properties, as well as for its ease of application and low cost.[6] The sodium salicylate was dissolved in ethanol and sprayed in a fine mist onto a quartz window. The window not only served as a physical support for the scintillating material, but also as a vacuum seal. As long as the surface density of the scintillating material remained between 2 to 10 mg/cm^2, the response of this material (Fig. II-11a)[7] was flat over the range of the experiment and reproducible from experiment to experiment. The sodium salicylate fluorescence spectrum (Fig. II-11b) closely matched the response curve of the EMI 9824B photomultiplier used to monitor this fluorescence. The dynode chain used with the PMT, shown in Figure II-14a, worked extremely well in conjunction with the discriminator used. The supply voltage was usually held at -1250 V, giving a dark count of about eight counts/sec.

As shown in Figures II-12a[8] and 12b,[9] another significant advantage of sodium salicylate was its almost constant quantum efficiency over the

entire range of this experiment (550 to 1300 Å). The quantum efficiency of sodium salicylate is unity for a new scintillator and drops with age; the spectral response remains constant. Since only relative measurements of VUV photon flux were needed, efficiency degradation was not important.

The scintillation efficiency was so great that two ways of attenuating the signal were required. First, a horizontal slit was placed directly in front of the scintillator to attenuate VUV light in the (non-dispersed) vertical direction. Secondly, a combination of Kodak Wratten neutral density gelatin filters (Cat. 1496330, 1496363 and 1496405) of values 0.3, 0.6, and 1.0 respectively were used. They were placed in various combinations between the quartz window supporting the scintillating material and the photomultiplier. These filters had a constant attenuation over the spectral range of the fluorescence and a blue cut-off, which in conjunction with the PMT response, lowered the response to unwanted UV light. During a given experiment, substituting ND filters rather than varying the gain of the photomultiplier was used due to the inherently higher reproducibility of the filters.

3) Fluorescence Monitoring

Fluorescence was observed through a port orthogonal to the VUV light path. This port (Fig. II-15) had to be very flexible in its geometry and function to satisfy experimental needs. One of the byproducts of VUV photolysis of $Fe(CO)_5$ is gaseous iron atoms, which deposit on any and all surfaces. If the surface was an optical window, there was a tendency to form a mirror, which was unacceptable. The position of the quartz window was adjusted such that iron deposition was all but eliminated while photon collection still occurred efficiently. An O-ring seal

was constructed around a positioning tube containing the window, and a locking collar held the tube in place against the pull of the vacuum.

For undispersed fluorescence measurements, a RCA C31034 photomultiplier was placed directly behind the quartz window. Figure II-14b shows the pulse counting dynode chain used in conjunction with this tube. This photomultiplier was chosen for its high quantum efficiency and excellent response over the range 2000 - 8500 Å. The photocathode was held at -1600 V, which optimized the signal-to-noise ratio. A mu-metal shield connected through a 0.1 MΩ resistor to the negative high voltage served as a Faraday cage protecting the tube from stray electromagnetic fields. To minimize background, the tube was cooled with dry ice, yielding a dark count of 2-3 counts/sec. The fluorescence light path was purged with dry nitrogen to eliminate water condensation on any cold optical surface.

For dispersed fluorescence, a 0.25 m JA monochromator Model 82-422, fitted with a 2360 grooves/mm grating blazed at 300 nm, was inserted between the RCA PMT and the observation port. A grating drive was also added to facilitate scanning. Slits were kept at 1000 μm, which yielded very low resolution, but high transmittance. The monochromator was also purged with dry nitrogen.

4) $Fe(CO)_5$ Source and Sink Assembly

To solve the problem of localizing a high density of $Fe(CO)_5$ (Alfa products, 99.5%) in conjunction with windowless optical pathways, a dynamic source-sink arrangement was used. The source was a nozzle which produced a semi-effusive beam of $Fe(CO)_5$. The sink was a high efficiency cryopump.

The entire beam assembly was supported by the chamber lid; the valve and pumping assembly can be seen in Figure II-9. A 500 ml round bottom glass flask fitted with a 5 mm glass-Teflon greaseless stopcock served as the liquid $Fe(CO)_5$ reservoir. The only $Fe(CO)_5$ purification step was one freeze-pump-thaw cycle. To maintain the beam flux as constant as possible, the flask was immersed in a constant temperature water bath at 31.7°C. This temperature produced a vapor pressure of ~40 torr and an $Fe(CO)_5$ beam flux of 13 g/min, equivalent to 6.6×10^{20} molecules/sec or approximately one millimole/sec. The flow of $Fe(CO)_5$ could be turned on or off (not pulsed) by an air-cooled Anzo solenoid valve operated at 70 V AC (not the recommended 117), and controlled through an interface to a PET 2001 microcomputer. The lowered valve voltage was sufficient for fast action, and decreased the power dissipation in the valve. This aided substantially in maintaining the valve temperature below 80°C, the thermal decomposition temperature of $Fe(CO)_5$. To monitor pressure and flow, a Matheson (Model 63-5601) mechanical pressure gauge was inserted between the $Fe(CO)_5$ reservoir and the solenoid. Inside the vacuum chamber, the beam emanated from a 1/4" ID x 1" long nozzle.

The main body of the cryopump, shown in Figure II-16, consisted of a liquid nitrogen container which was welded from 5/16" OFHC copper and was fed through two tubes protruding through the chamber lid. To increase the cold surface area in the direction of maximum beam flux, an 8" long, 3" OD copper tube was welded into the body of the LN_2 container. The feed tubes were constructed from 1/2" OD stainless steel tubing hard-soldered to the container body. At the top, a 1" OD stainless steel tube was welded over the smaller one making double-walled construction. A Cajon O-ring fitting welded onto the lid vacuum-sealed the 1" sleeve

to the chamber. The double-walled construction was used to reduce the possibility of freezing the sealing O-ring.

Four baffles made of 3/16" OFHC copper were screwed onto the top of the LN_2 container in planes orthogonal to the VUV light path. Each baffle had an opening in it, the width of which was set to the width of the VUV light beam based on the distance of the baffle from the exit slit and the VUV monochromator acceptance angle. Care was taken to ensure alignment of these openings. Misalignment in conjunction with their slow closure due to solid $Fe(CO)_5$ deposition would introduce an unacceptable systematic error into the VUV photon absorption measurement. Finally, a copper cover was screwed over the entire assembly.

This assembly was lowered into the vacuum chamber and rested on three pins, the heights of which were adjusted to give the cryopump the correct vertical position. Once the lid was lowered and the feed tubes aligned through the Cajon vacuum seals, the cryopump was positioned in the horizontal plane.

The vertical position of the nozzle (schematically shown in Fig. II-18) was determined by the flow pattern of the beam. Since the nozzle did not generate a purely effusive beam (our nozzle opening was much larger than the mean free path of the molecules), we could not assume a straight and collisionless path for molecules emanating from the nozzle.[10] Just outside of the nozzle, the molecules experienced a region of expansion with collisions diminishing in frequency as they moved downstream, culminating in a collisionless regime. The net result was that far downstream, the molecules appeared to emanate from a virtual effusive beam source positioned a distance $x°$ downstream from the real nozzle. For γ, the heat capacity ratio, of 1.2857, the ratio $x°/D$, where

D is the nozzle diameter, was empirically determined to be 0.85.[10] This calculation showed that the nozzle had to be positioned at least 1/4" above the point of origin of a straight-line path through the openings in baffles one and two, ensuring at least one collision of each $Fe(CO)_5$ molecule with the cryopump surface. To build in a margin of safety, 1/2" was used. The efficiency of this configuration was so good that an ionization gauge registered no pressure fluctuations as the beam was valved on and off.

The cryopump required about twelve liters of LN_2 to attain 77 K, as monitored by three iron-constantan thermocouples. Four cartridge heaters were attached to the body of the cryopump to accelerate its warmup at the end of an experiment.

5) $Fe(CO)_5$ Disposal

The cryopump solved the $Fe(CO)_5$ pumping problem temporarily during the experiment. However, the $Fe(CO)_5$ still had to be removed from the cryopump once it was warmed to room temperature. This dilemma was solved by taking advantage of the low thermal decomposition temperature of $Fe(CO)_5$. Once the interaction chamber was isolated from its primary pumping system and the monochromator, the cryopump was slowly warmed by the four cartridge heaters. Copper mesh and foil increased heat transfer from the heaters to the body. To eliminate 'hot spots' and decomposition of the iron pentacarbonyl, the heater power was limited to a total of 40 watts. The $Fe(CO)_5$ vapor was pumped by a small mechanical pump through a pyrolyzer, shown on Figure II-17, where it was decomposed into Fe and CO as it contacted a hot pyrex tube. The iron was deposited on the glass surface and the carbon monoxide was pumped away. The glass

tube was heated radiatively from an outer stainless steel jacket heated to 240°C. Once the disposable glass tube was full of iron, it was easily replaced. The deposited iron was extremely brittle and hard and showed signs of crystal growth. The iron 'rods' were so hard that a standard metal saw would not even scratch the surface. Another interesting feature of these rods was that NO oxidation was apparent after exposure to air for a year. Care had to be taken when the pyrolyzer was vented since small explosions could easily occur as oxygen came in contact with the very hot and very small particles which formed around the main chunk of solid iron.

6) Photo-ionization Detection

A simple experimental apparatus was used to detect photo-ions produced by VUV photolysis, as shown in Figure II-18. The system consisted of a negatively biased collection electrode positioned on the nozzle (but out of the $Fe(CO)_5$ beam) and held at room temperature. This was the only place where $Fe(CO)_5$ would not coat the ion collector. The no-load 96 V bias was supplied by two 45 V Eveready batteries. Special care had to be taken to insulate the paper covering of the batteries from electrical ground with 1/4" thick Plexiglas separators to eliminate electrical leakage.

To detect the photocurrent, a Keithley Model 610B electrometer was used on a sensitivity range of 10^{-9} A full scale. This range was internally coupled with a multiplier range from 3 to 0.03. The smallest currents measured were on the order of one to two pA. To keep the ion signal electrically quiet at these sensitivities, the cryopump surrounding the interaction region was directly grounded, producing a Faraday cage around the collector. Moreover, all connections were made

with short coaxially shielded cables. The experimental data were recorded on a strip chart recorder in the form of ion current versus wavelength recordings.

7) Beam Density Monitoring

In order to determine the $Fe(CO)_5$ beam density in the interaction region, an absorption experiment was done in a wavelength region where the $Fe(CO)_5$ extinction coefficient is known and is large enough for easy experimental detection, i.e., 2000-3500 Å. The light in this wavelength region entered the interaction chamber through a quartz window mounted in a flange fitted to a port directly opposite the fluorescence collection port. This configuration allowed simultaneous absorption measurements in the VUV on one axis using the scintillator and in the UV on the other axis using the RCA 31034 PMT operated at low gain.

Two separate light source configurations were used in the measurement. The simultaneous density measurement in two axes also allowed absorption spectrum monitoring for accurate absorption curve determinations.

The light source used in conjunction with the scintillator was the hydrogen lamp emission at 1170 Å. Two different light sources were used in the UV. The first was the light from an Oriel mercury pen lamp dispersed by a JA 0.25 m monochromator (Model 82-422) using the 2536.5 Å line of Hg. The second was the light from a low pressure deuterium lamp (Heathkit light source Model EU-701-50) dispersed by the same monochromator. This configuration yielded continuous usable signal from 2200 Å to over 3500 Å. For some measurements, an Oriel G-774-3300 band pass filter was inserted between the deuterium lamp and the monochromator to minimize scattered light.

E. Detection Electronics and Experimental Control

Since there were relatively low signal levels in the fluorescence channel and numerous data manipulation steps, a digital counting technique was adopted. The signal from a PMT was discriminated and the counts gathered in a given period of time were stored in the computer memory for direct access. The electronics used can be separated into two sections:

1) data gathering and

2) experimental control.

Each one had its own interface to a PET 2001 8 K microcomputer. The electronics are pictured schematically in Figure II-19. On the detection side, two independent channels were used to monitor the iron atom fluorescence and the scintillator simultaneously. In the first channel, the fluorescence signal from the RCA C31034 photomultiplier was passed through a PAR Model 1120 discriminator coupled to a PAR Model 1105 data converter. The ECL pulse from the data converter was transformed to a TTL pulse sent to the counting interface. In the second channel, the scintillation signal from the EMI 9824B PMT was processed by a NE 4630 amplifier/discriminator. This signal was amplified 1000 fold with a 0.3 μs time constant before discrimination. The output from this unit was then fed directly to the second channel of the counting interface.

The counting interface itself is shown in Figure II-20 and had as main components a Datel 8253 three-channel, 16 bit down counter and a Datel 8255 communication/control chip. The three channels on the 8253 and 8255 could be directly accessed as memory locations in the PET through the use of BASIC PEEK and POKE commands. These locations are shown in the table below.

The 8255 controlled the actions of the 8253 counting chips as well as controlling the pulses that the 8253 was allowed to count. Port A on the 8255 was set by the PET to read, and ports B and C, to write.

MEMORY LOCATION	FUNCTION
28720	8255 Port A
28721	8255 Port B
28722	8255 Port C
28723	8255 Mode Port
28724	8253 Counter 1 (not used)
28725	8253 Counter 2 (scintillator)
28726	8253 Counter 3 (fluorescence)
28727	8253 Counter Control

Port A was used with a PEEK command to indicate to the data acquisition program if overflow (i.e., a count greater than 65535) had occurred in one of the 8253 counters. Bit 1 of Port A was high (i.e., equal to one) if counter 1 overflowed, and bit 2 was high if counter 2 overflowed. These bits in Port A could be used as a warning of overflow or as a seventeenth bit of each counter, doubling their counting range. There were also LED's provided for each channel to show if an overflow had occurred since the LED's were last reset.

Only three bits of Port C merit discussion. Bit 0 of Port C was used to place the 8253 chip in a read mode to allow the PET to access the data stored in the counters. Bit 4 was used to gate signals into both counters simultaneously. Bit 5 was used to reset the overflow LED's mentioned earlier. One-shot pulse shapers were inserted between the gates and the 8253 to insure pulses were always of the correct shape for registry by the 8253.

A single channel on the experiment control side governed the actions of the beam solenoid valve. The PET controlled this channel through one TTL line in the PET user port. This signal controlled the solenoid through a buffered Teledyne zero-voltage crossing solid state switch and a Variac variable transformer. The computer valve control could be manually overridden through a switch. The time response of this arrangement allowed valve switching faster than 0.1 sec, significantly faster than required by the experiment.

F. Experimental Software

The software developed for data acquisition is a single, extremely flexible program, designed to run on a PET 2001 8 K microcomputer. To enable the reader to understand the listing in Appendix I, some of the features of this program are outlined below:

1) The data gathering interface is accessed by PEEK and POKE commands through the memory expansion port.
2) The experimental control interface is accessed through the PET user port, a built-in eight bit bidirectional parallel port.
3) The precise timing required in a real time experiment is achieved using the 'jiffy' clock internal to the PET 2001 computer, allowing a time resolution of $1/60^{th}$ of a second. Through the implementation of a machine language timing routine, the accuracy of the timing is on the order of the execution time of a couple of machine language instructions, i.e., ~10 μsec. This leads to timing accuracy better than one part in 1000.
4) In order to save memory, no remarks or comments are included in the program.

5) The program can store simultaneously four sets of data, each of which has space for 91 data points (channels). These sets are:

	CHANNEL 1 (Fluorescence)	CHANNEL 2 (Scintillator)
$Fe(CO)_5$ beam on	Data set 1	Data set 2
$Fe(CO)_5$ beam off	Data set 3	Data set 4

6) The program has seven operating modes which are accessed through the keyboard by keying the underlined code letters shown below:

a) Load - (Lines 6000-6100) The internal microcode (discussed later) is loaded.

b) Clear - (Lines 7000-7500) All four data channels are cleared.

c) Write - (Lines 4000-4950) All four data channels are written on cassette 1 formatted for use by the data handling program.

d) Display - (Lines 3000-3950) The four data channels are displayed in parallel on the screen.

e) Activate - (Lines 5000-5500) Once in this mode, the PET will read the two counter channels at a rate of 1 Hz and display the data on the screen. Pressing key 1 or 0 will activate or deactivate, respectively, the $Fe(CO)_5$ beam. The data are not stored.

f) Set-up - (Lines 2000-2950) The data gathering conditions are established in conjunction with the data taking

pattern (microcode). Time per channel is either entered in seconds or computed from the scan speed and Å/channel. The length of the time unit is computed by comparing the total amount of time allocated to a channel and the total number of time units requested by the microcode per channel.

g) Run - (Lines 100-740) The execution of the experiment is initiated. Once in the run mode, the synchronization of the computer with the monochromators is accomplished with a press of any key. Termination of the experiment will occur at the end of the channel during which any key was pressed. This procedure should be executed once before running the experiment to allow the PET to assign all the variables.

7) The flexibility of this program lies in the use of a microcode that controls the data gathering pattern. It consists of a sequence of eight bit instructions denoted as:

$$X_7X_6X_5X_4X_3X_2X_1X_0.$$

$X_4X_3X_2X_1X_0$ represents in binary the duration of the current instruction from 2 to 31 in number of time units.

X_5 controls the beam and the data set to which data are added. If zero, the beam valve is closed at the start of the current instruction. If one, the beam valve is opened.

X_6 determines whether data are retained or not. If one, data will be added to the current channel; if zero, data will not.

X_7 is the end of the microcode bit. Normally zero, it is set to one in the last micro-instruction of the channel.

Through the use of this microcode, the sixteen bit counters can count up to 10^7 counts in a period of a minute with a loss of only 30% of the data during transfer from counters to the PET. The lower the counting rate required, the lower the data loss will be.

REFERENCES for CHAPTER II

1. James A. R. Samson, Vacuum Ultraviolet Spectroscopy (John Wiley and Sons, Inc., N.Y., 1967).
2. F. A. Cotton, A. K. Fischer, and G. Wilkinson, J. Am. Chem. Soc. 81, 800 (1959).
3. C. H. Corliss and J. L. Tech, Nat. Bur. Stand. (U.S.) Monogr. 108 (1968).
4. A. N. Zaidel' and E. Ya. Shreider, Vacuum Ultraviolet Spectroscopy (Ann Arbor-Humphrey Science Publishers, Michigan, 1970).
5. Cheuk-Yiu Ng, Ph.D. Thesis, University of California, Berkeley; LBL Report 5439 (1976).
6. F. S. Johnson, K. Watanabe, and R. Tousey, J. Opt. Soc. Am., 41, 702 (1951).
7. M. Seya and F. Masuda, Sci. Light, 12, 9 (1965).
8. J. A. R. Samson, Unpublished Data (1965).
9. J. A. R. Samson, J. Opt. Soc. Am. 54, 6 (1964).
10. J. H. DeLeeuw, Rarefied Gas Dynamics, Vol II (Academic Press, N.Y., 1966).

Table II-1

Typical VUV Lamp Operating Conditions

	Emission Wavelength Å	Transitions	Discharge Gas Pressure (μ) (Uncorrected Thermocouple) Anode	Cathode	Lamp Current (ma)	Valve V1 Condition (see Fig. II-5)
H_2 *** (Pacific Oxygen Co)	850-1650	molecular	2200*	800*	500**	Open
	1215.668	Lyman α				
	1025.722	Lyman β				
Ar (Liquid Carbonic)	1048.219	$^1P_1 - {}^1S$	95	95	165	Closed
	1066.659	$^3P_1 - {}^1S$				
Ne (90% neon-10% Helium) Union Carbide Spark Chamber Grade	735.895	$^1P_1 - {}^1S$	800*	800*	500**	Closed
	743.718	$^3P_1 - {}^1S$				
He (Oil Free Helium)	584.334	$^1P^o - {}^1S$	1200*	1200*	500**	Closed

* Highest Allowed.

** Highest Available.

*** Operating conditions optimized for molecular emission.

Figure II-1. A block diagram of the crossed VUV-molecular beam fluorescence apparatus.

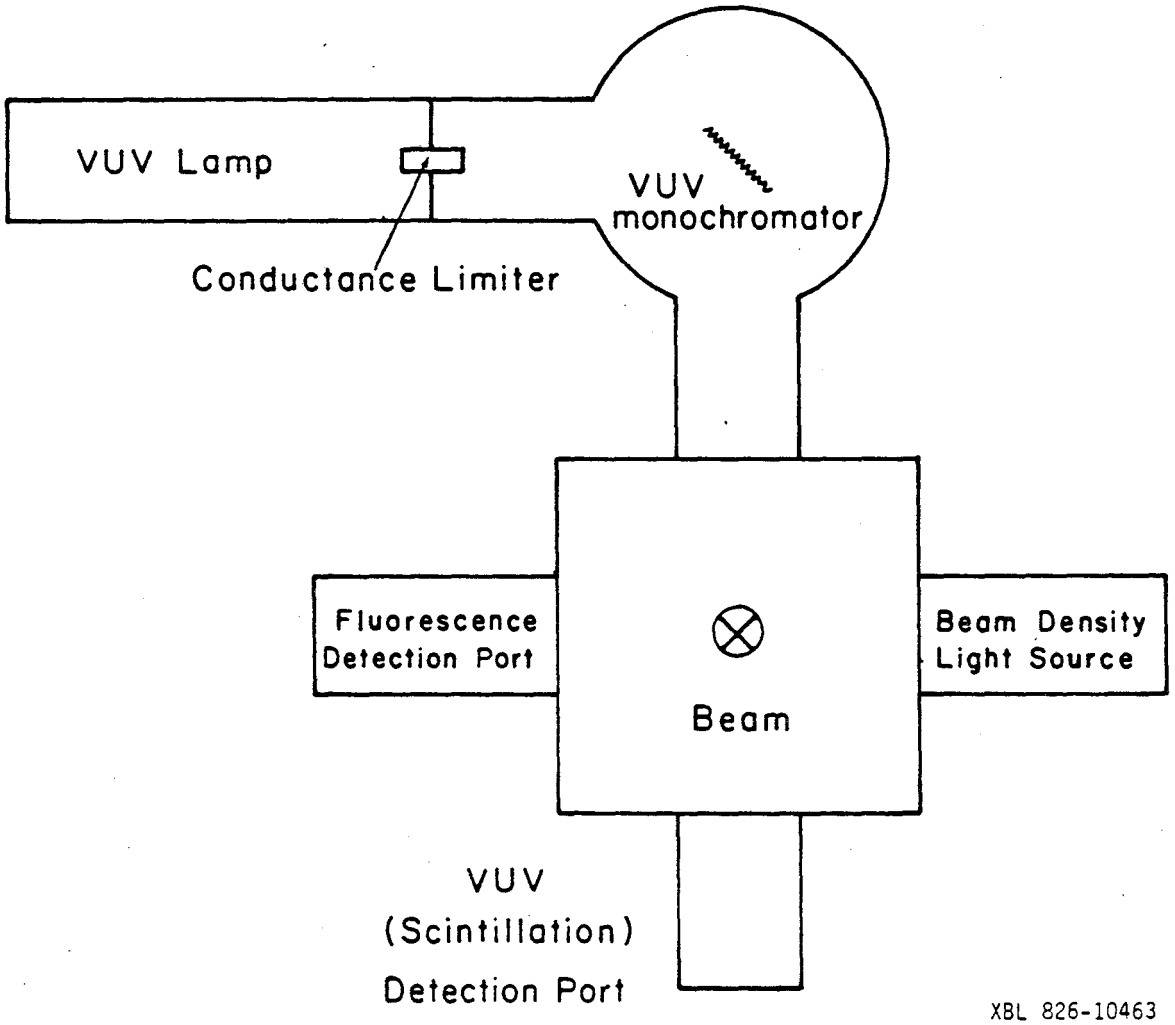
VUV Lamp
Conductance Limiter
VUV
monochromator
Fluorescence
Detection Port
Beam
Beam Density
Light Source
VUV
(Scintillation)
Detection Port
XBL 826-10463

Figure II-1

Figure II-2. High resolution H_2 discharge spectrum.

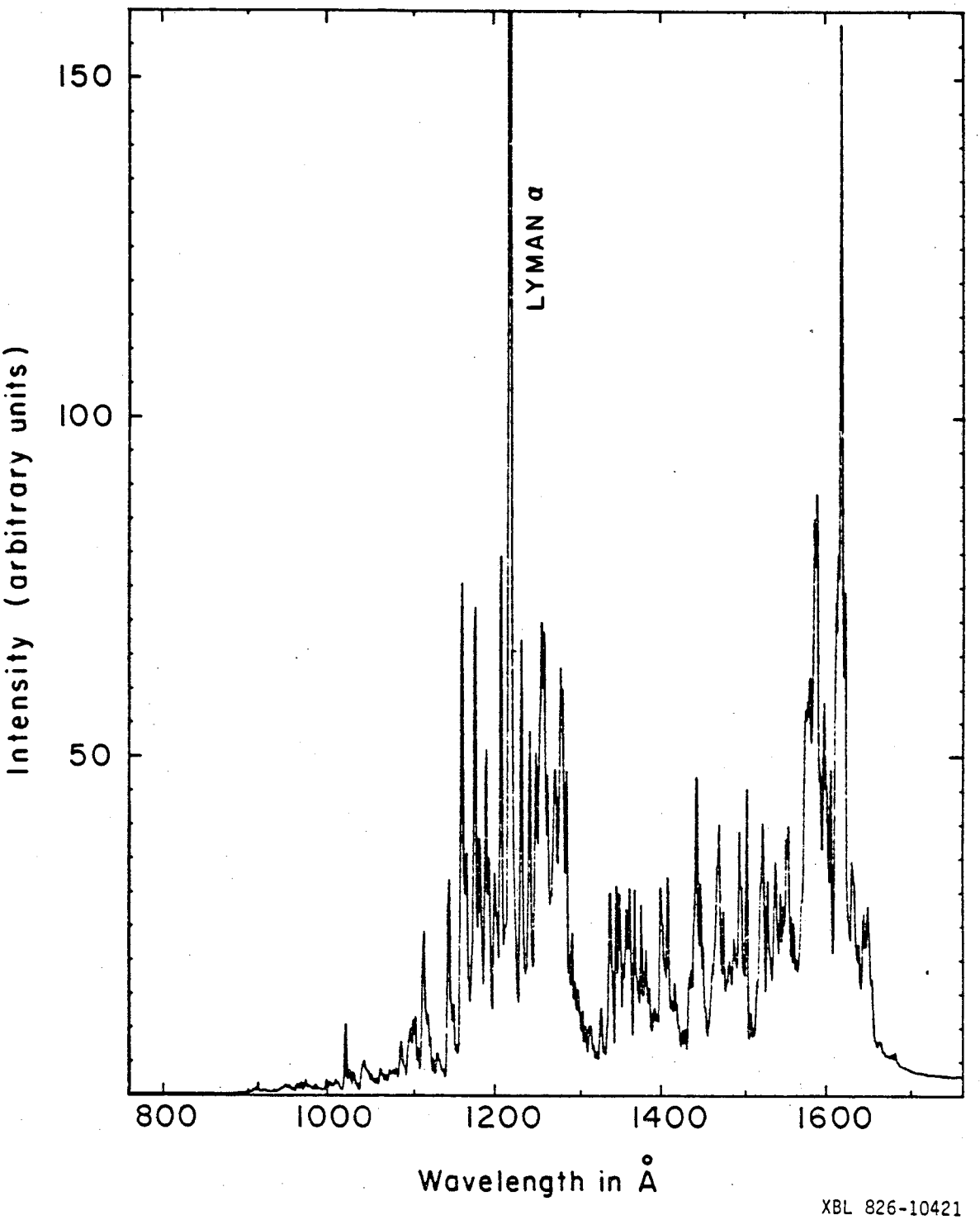
150
100
50
Intensity (arbitrary units)
LYMAN α
800
1000
1200
1400
1600
Wavelength in Å
XBL 826-10421

Figure II-2

Figure II-3. Experimental resolution H_2 discharge spectrum.

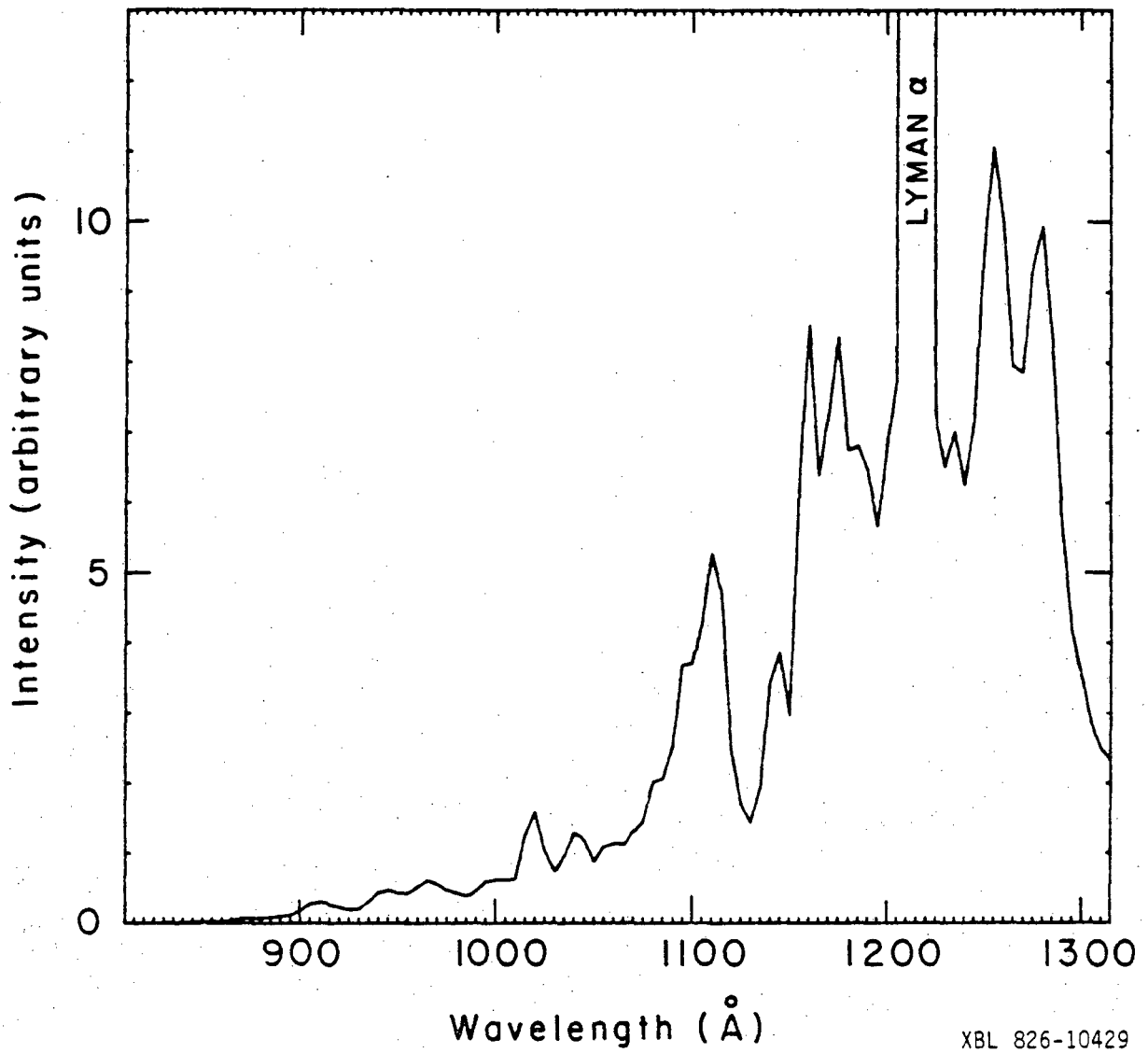
LYMAN α
Intensity (arbitrary units)
0
5
10
900
1000
1100
1200
1300
Wavelength (Å)
XBL 826-10429

Figure II-3

Figure II-4. Discharge lamp.

A) Cooling water connections

B) Cathode body

C) Cathode lid

D) Cathode protective insert

E) Cathode support rod

F) Insulator spacers

G) Quartz discharge tube

H) Discharge gas inlet

I) Protective shield

J) Conductance limiter

K) Anode body

L) Side view of the monochromator entrance slit

M) Thermocouple pressure sensor connection

N) Monochromator exit arm flange

O) Preslit

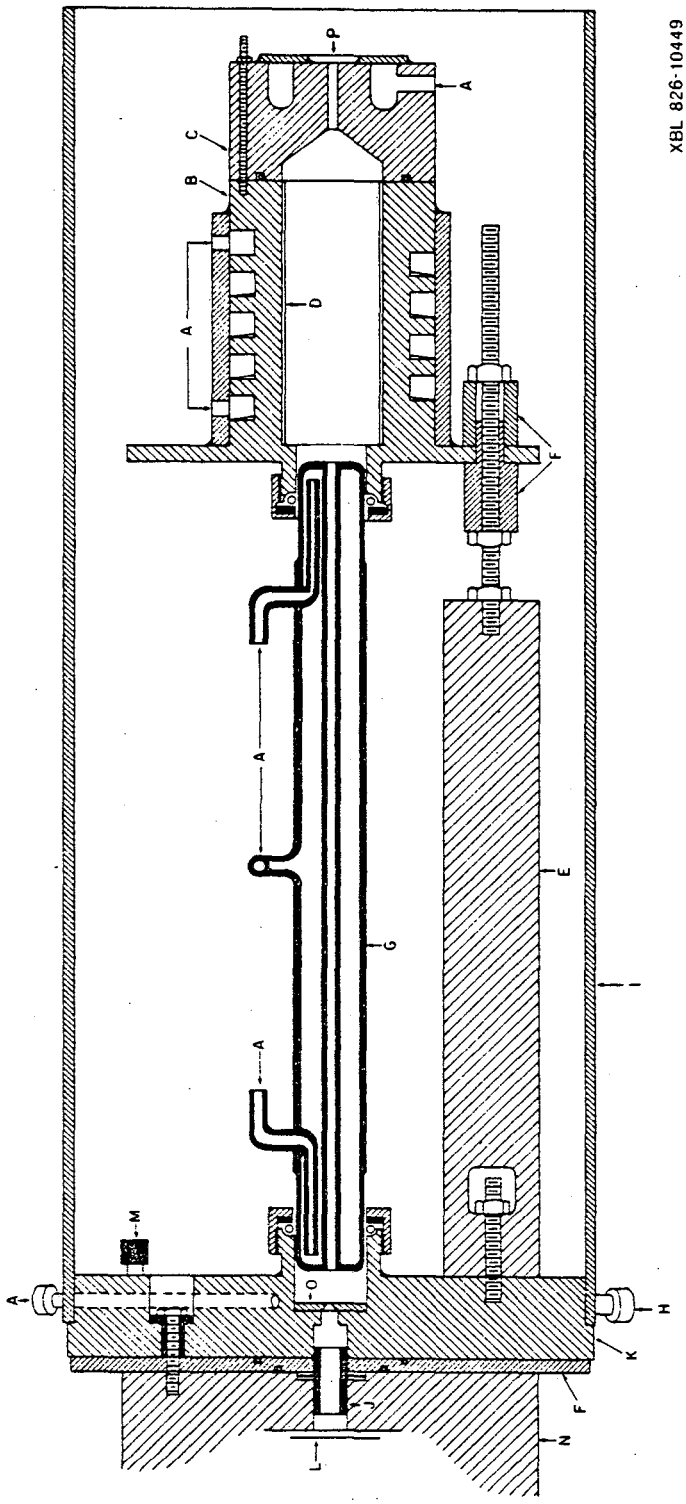

Figure II-4

Figure II-5. Pumping system and electrical connections to the discharge lamp.

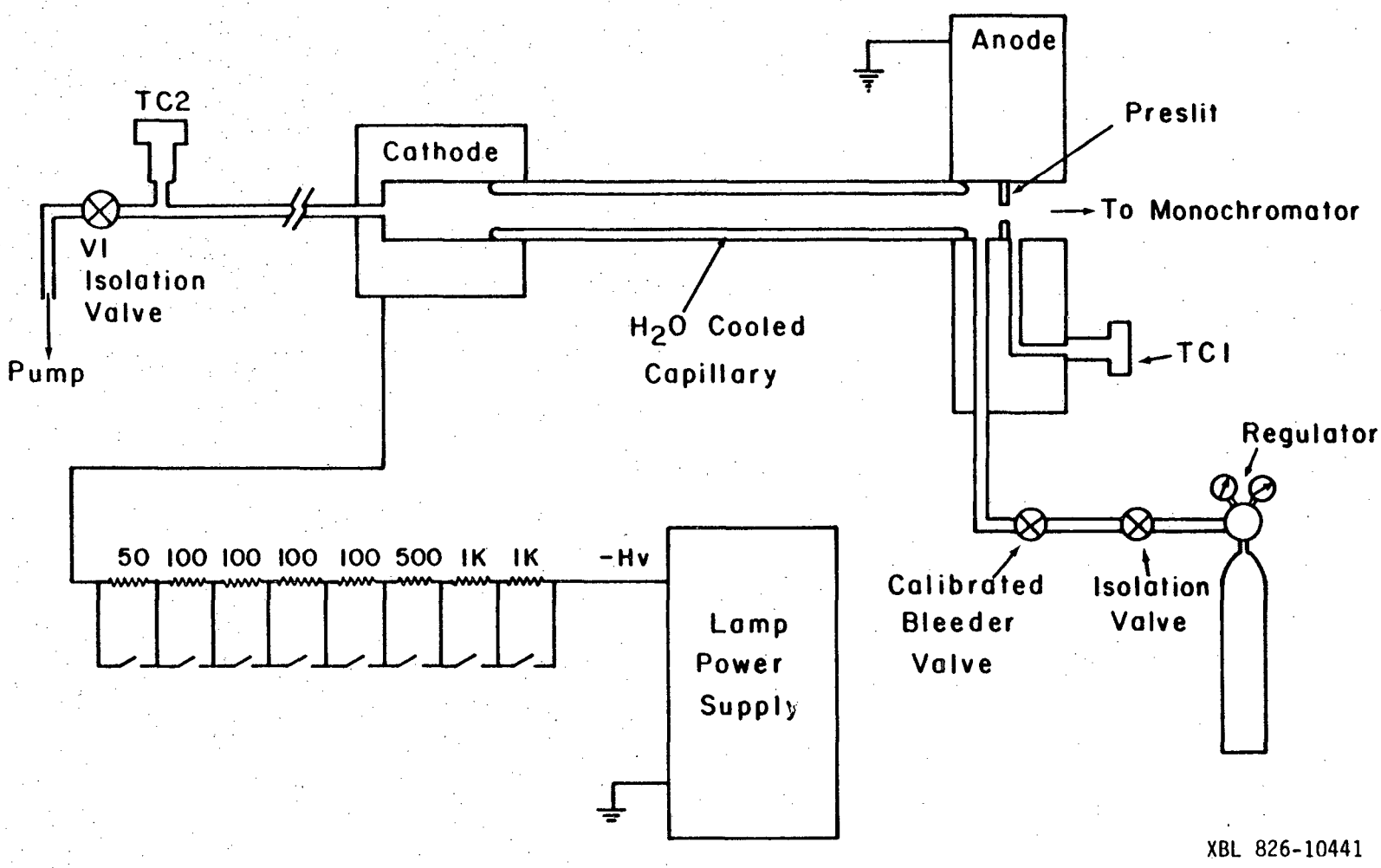
Anode
TC2
Preslit
Cathode
To Monochromator
VI
Isolation
Valve
Pump
H_2O Cooled
Capillary
TCI
Regulator
50 100 100 100 100 500 1K 1K
-Hv
Lamp
Power
Supply
Calibrated
Bleeder
Valve
Isolation
Valve
XBL 826-10441

Figure II-5

Figure II-6a. Conductance limiter.

b. Conductance limiter assembly.

A) Monochromator entrance arm flange

B) Entrance slits

C) Conductance limiter retainer rings

D) Conductance limiter

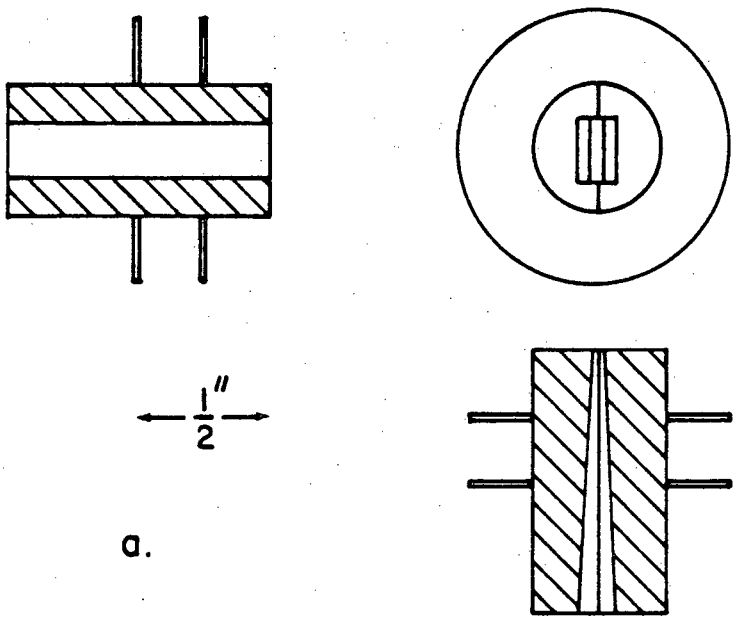

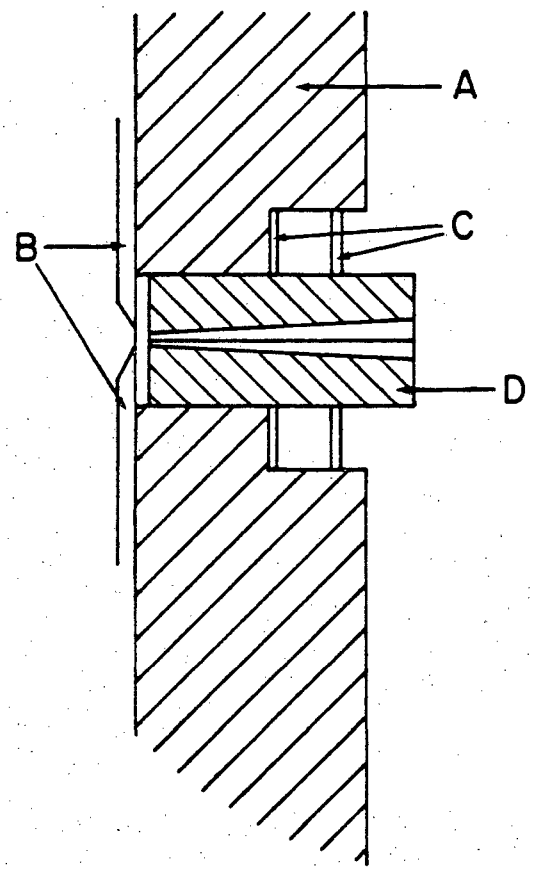

XBL 826-10431

Figure II-6

Figure II-7. Horizontal cross-section of the interaction chamber

A) Monochromator exit arm flange

B) Exit slits

C) Cryopump baffle #1

D) Cryopump baffle #2

E) Cryopump baffle #3

F) Cryopump baffle #4

G) Cryopump slip-on cover

H) Beam absorption port

I) VUV photon flux (scintillation) detection port

J) Fluorescence detection port

K) LN_2 feed tubes

L) Interaction chamber wall

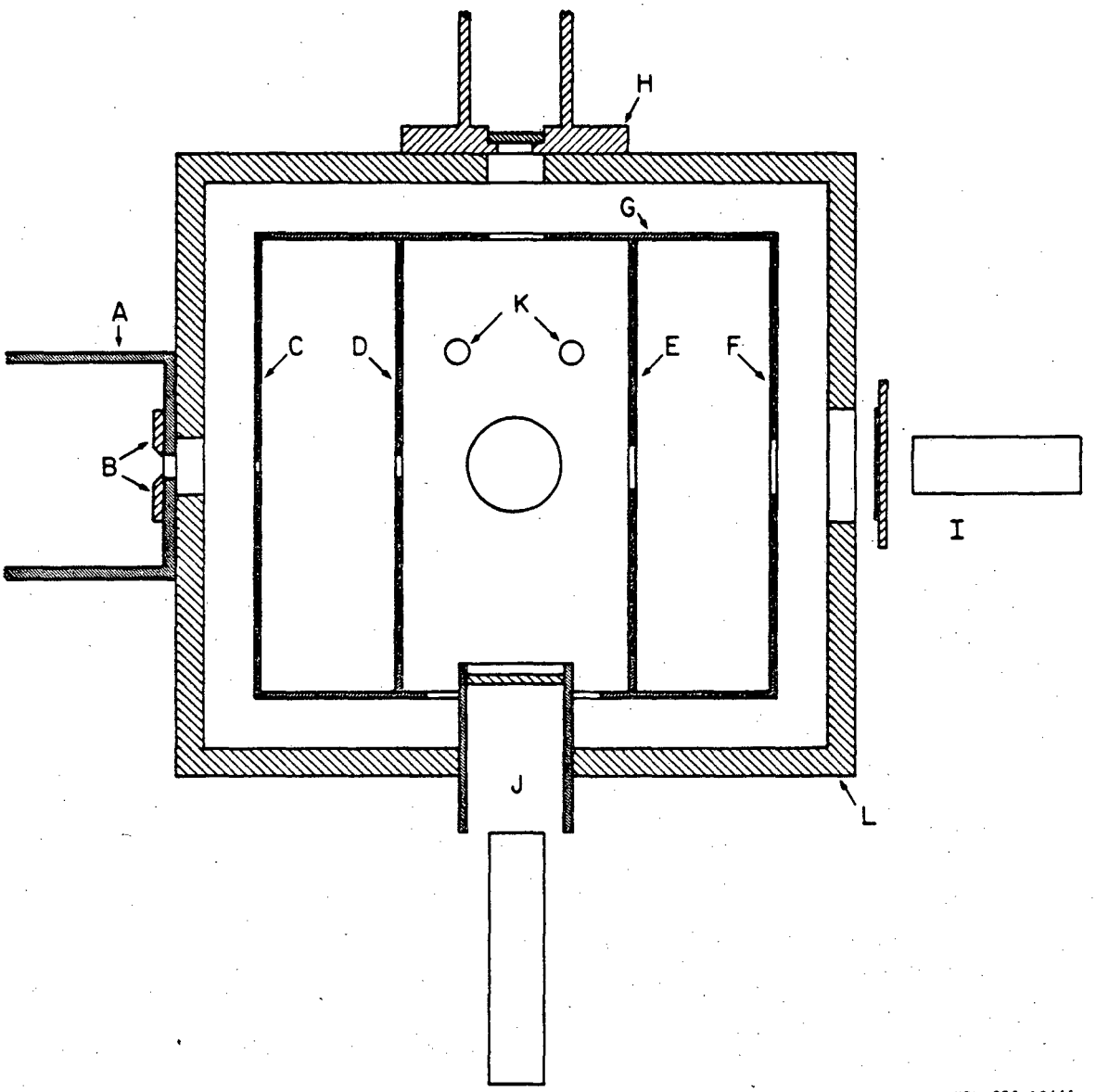

Figure II-7

Figure II-8. Vertical cross-section of the interaction chamber.

A) Monochromator exit arm flange

B) Exit slits

C) Cryopump baffle #1

D) Cryopump baffle #2

E) Cryopump baffle #3

F) Cryopump baffle #4

G) Cryopump body

H) Beam nozzle

I) VUV photon flux (scintillation) detection port

J) Cryopump support pillars

K) LN_2 feed tubes

L) Interaction chamber wall

M) Cryopump slip-on cover

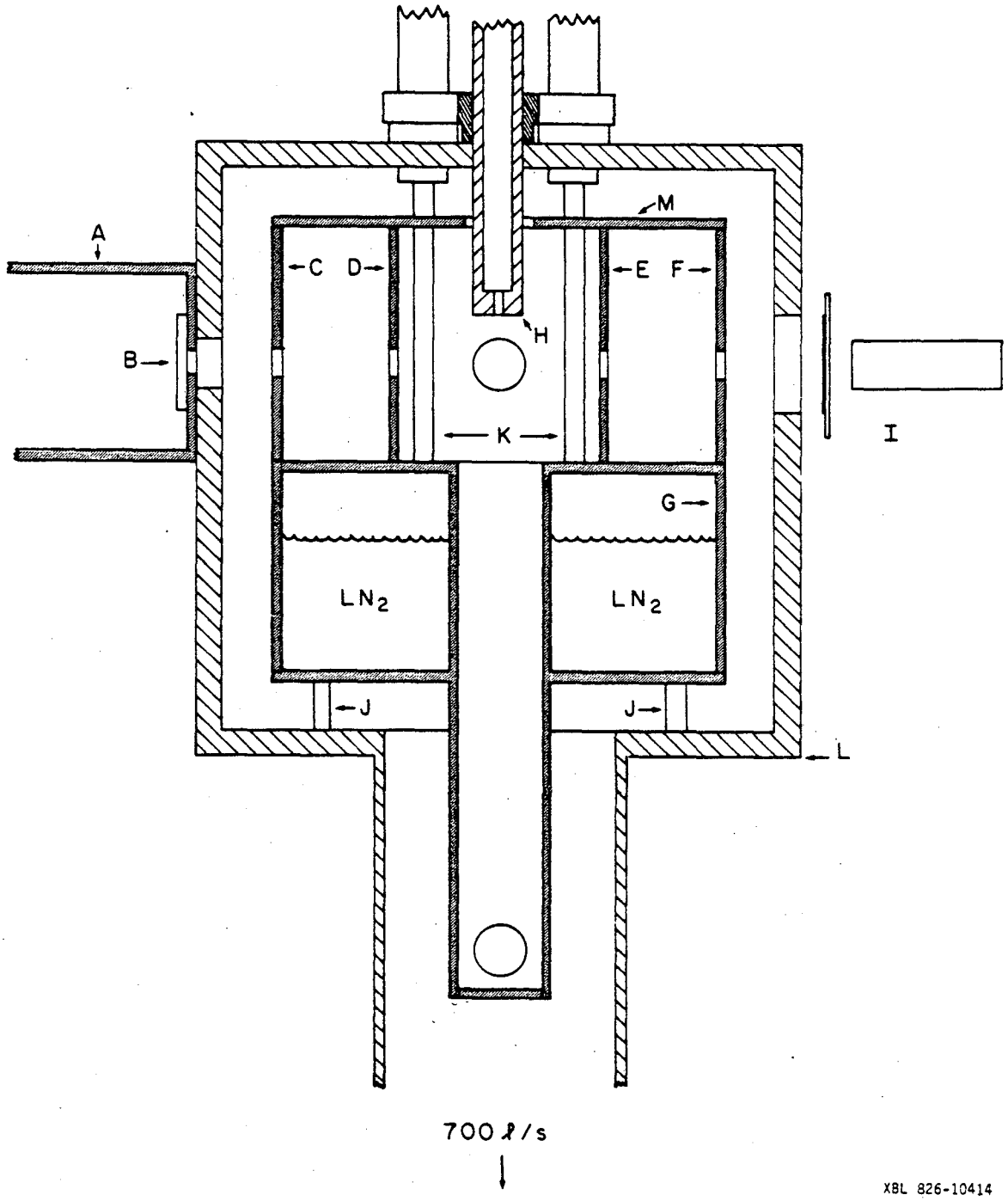

Figure II-8

Figure II-9. Interaction chamber and beam source pumping system.

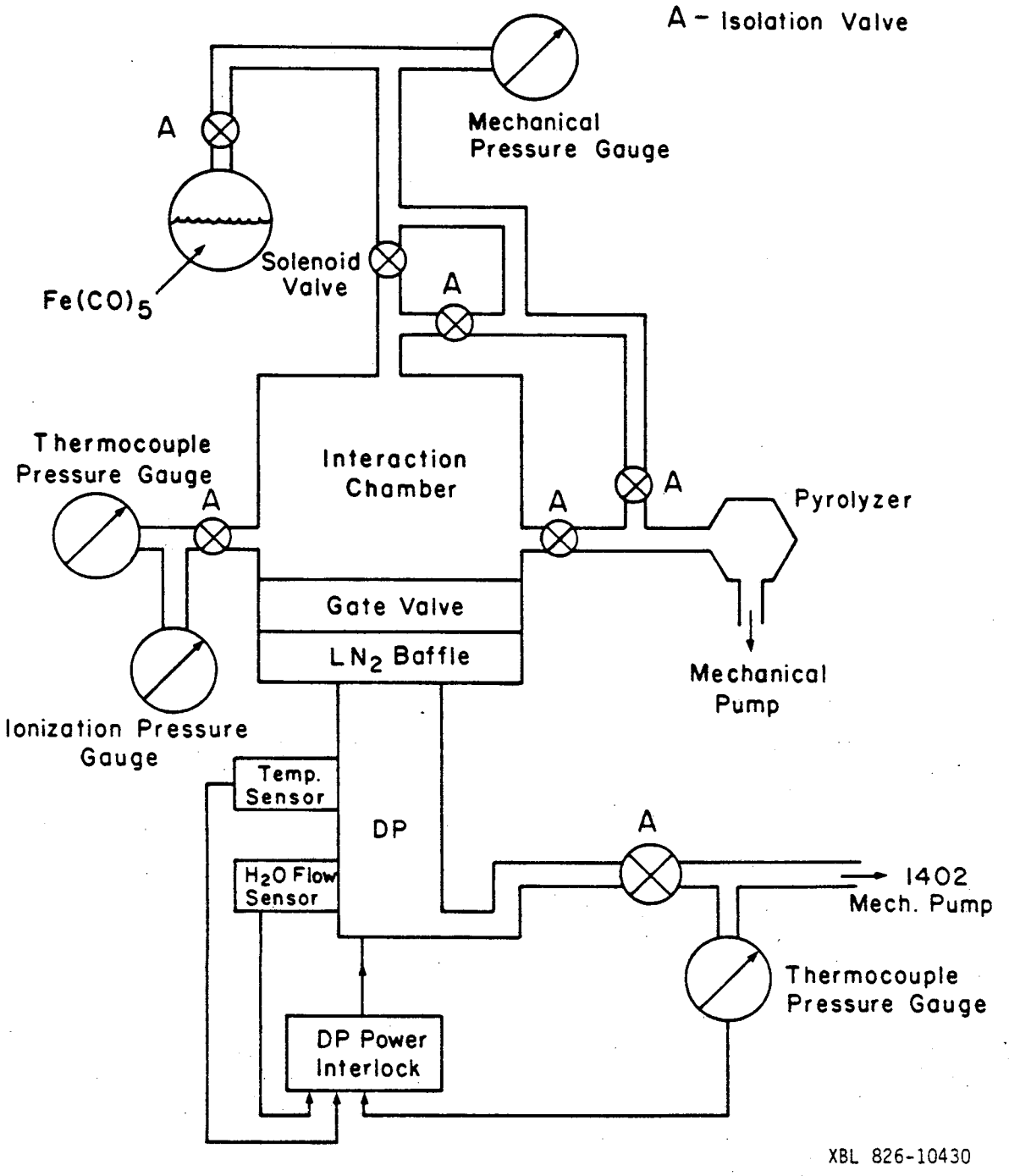
A – Isolation Valve
A
Mechanical
Pressure Gauge
Solenoid
Valve
A
Fe(CO)5
Thermocouple
Pressure Gauge
A
Interaction
Chamber
A
A
Pyrolyzer
Gate Valve
LN2 Baffle
Mechanical
Pump
Ionization Pressure
Gauge
Temp.
Sensor
DP
A
H2O Flow
Sensor
1402
Mech. Pump
Thermocouple
Pressure Gauge
DP Power
Interlock
XBL 826-10430

Figure II-9

Figure II-10. Assembly diagram of VUV photon flux (scintillation) detection port.

1) VUV solid slit attenuator
2) Interaction chamber wall
3) Quartz scintillator support and vacuum seal
4) Quartz window pressure plate
5) Scintillator support flange
6) Neutral density filter(s)
7) Photomultiplier chamber support flange
8) Chamber-flange vacuum O-ring seal
9) Flange-scintillator support O-ring seal
10) Sodium salicylate scintillator layer
11) Photomultiplier chamber
12) EMI magnetic shield
13) EMI 9824B photomultiplier tube
14) EMI photomultiplier socket B14B
15) Dynode chain holder
16) Photomultiplier housing
17) Photomultiplier housing endcap
18) SHV 1702-1 high voltage connector

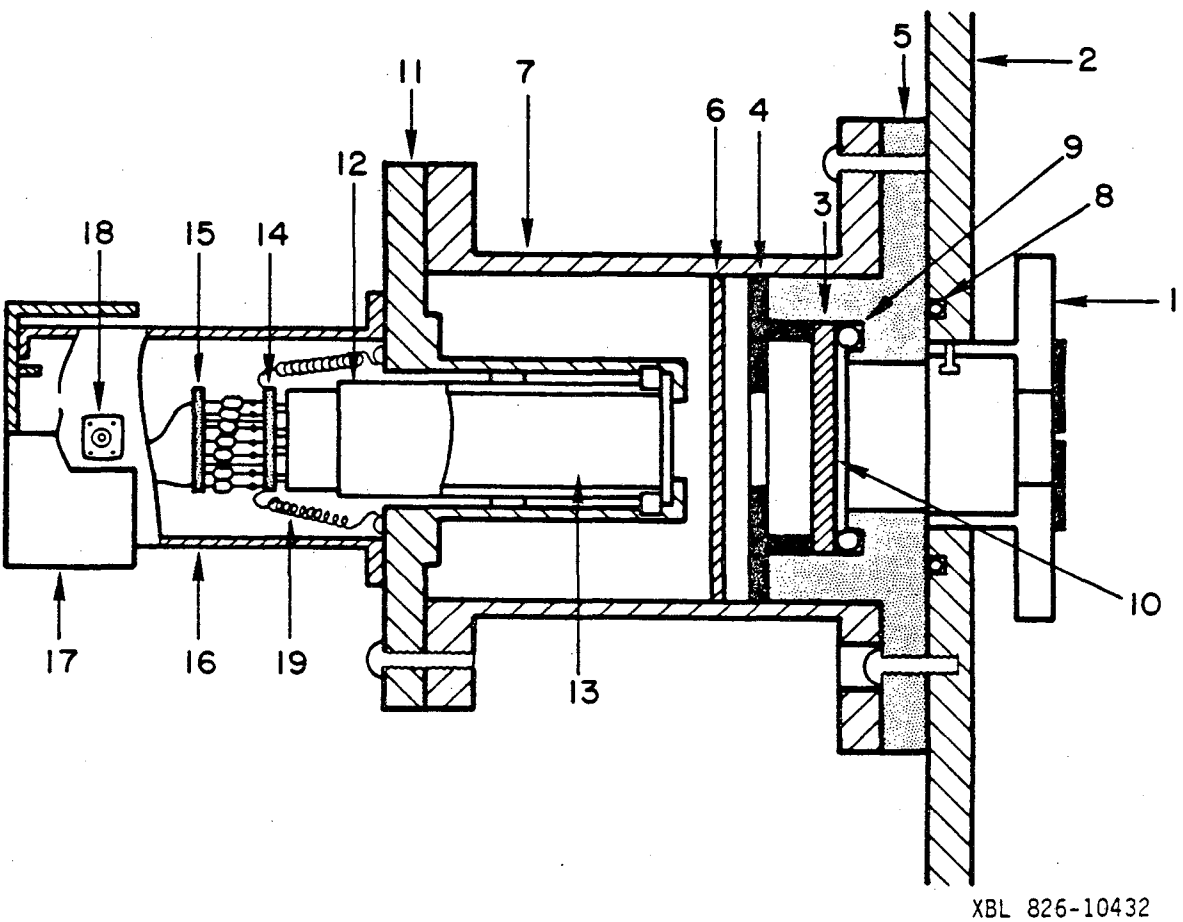

Figure II-10

Figure II-11a. Relation between response and thickness of sodium salicylate layer at 1200 Å.

b. Fluorescence emission spectrum of sodium salicylate.

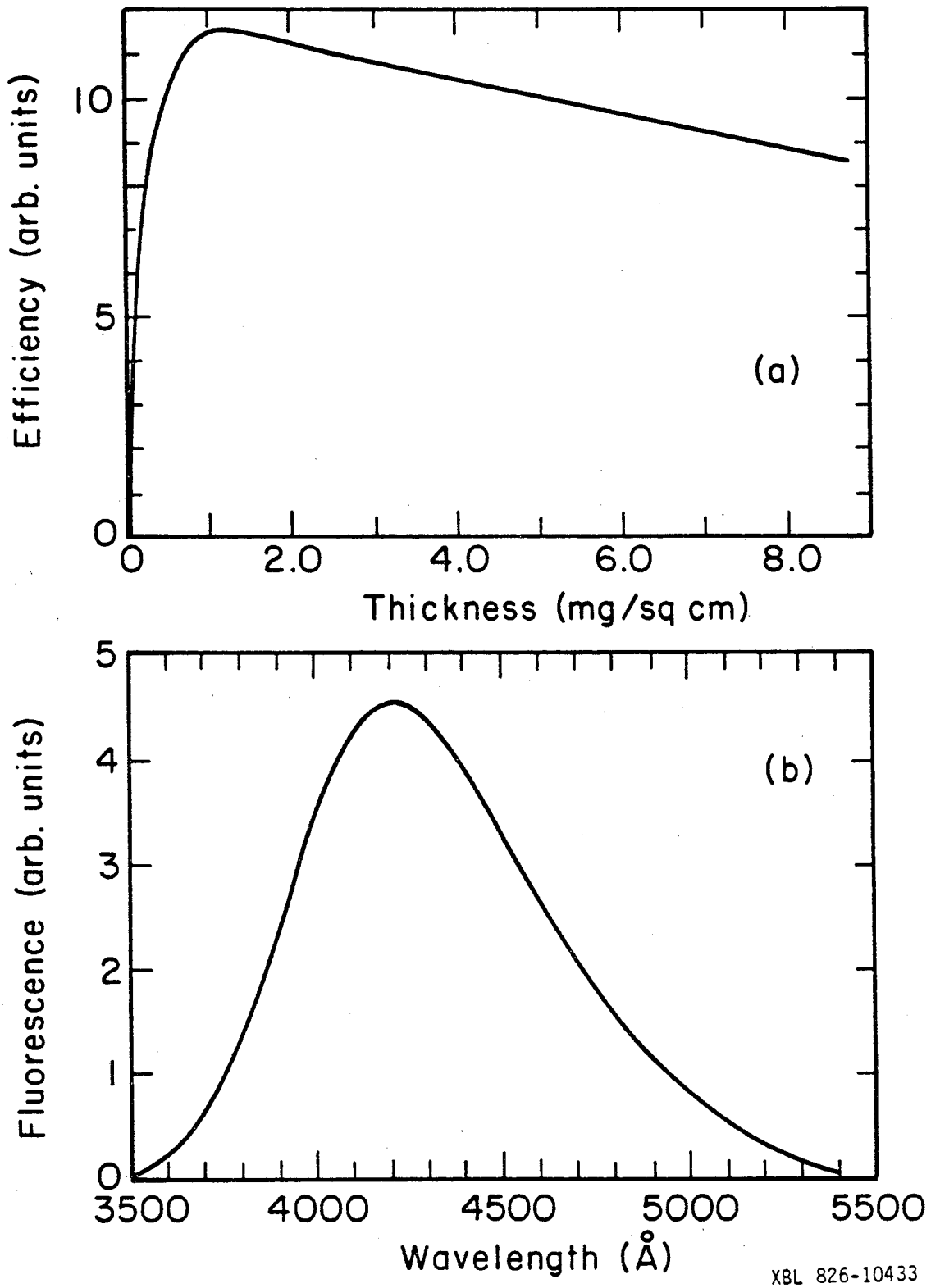
Efficiency (arb. units)
10
5
0
0
2.0
4.0
6.0
8.0
Thickness (mg/sq cm)
(a)
Fluorescence (arb. units)
5
4
3
2
1
0
3500
4000
4500
5000
5500
Wavelength (Å)
(b)
XBL 826-10433

Figure II-11

Figure II-12a. Relative quantum efficiency of sodium salicylate between 200 and 1000 Å.

b. Relative quantum efficiency of sodium salicylate between 900 and 1700 Å. Coating ages are indicated.

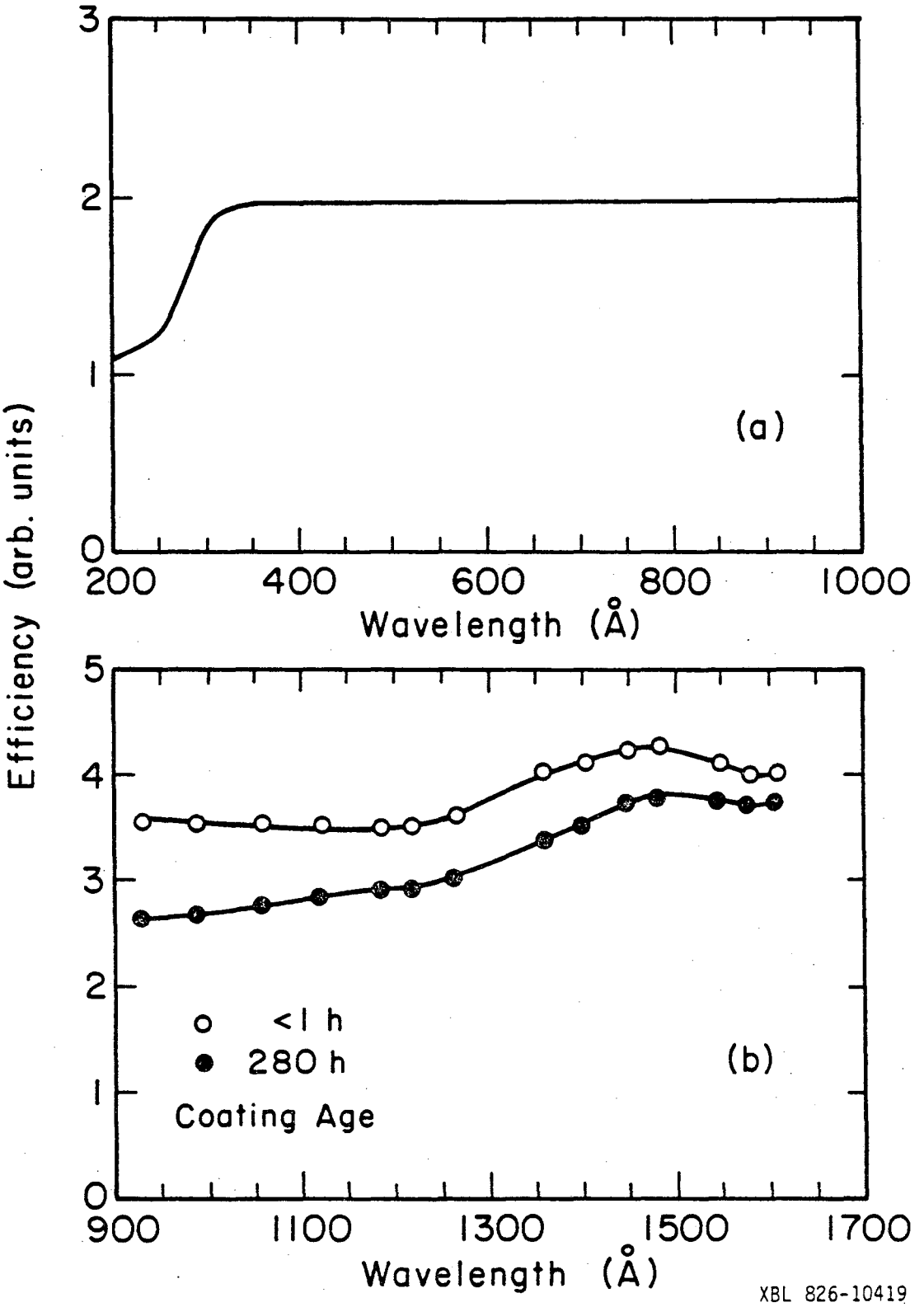
Efficiency (arb. units)
3
2
1
0
200
400
600
800
1000
Wavelength (Å)
(a)
5
4
3
2
1
0
900
1100
1300
1500
1700
Wavelength (Å)
< 1 h
280 h
Coating Age
(b)
XBL 826-10419

Figure II-12

Figure II-13a. Wavelength dependence of neutral density filter: 0.3.

b. Wavelength dependence of neutral density filters: 1.0 + 0.6 combination.

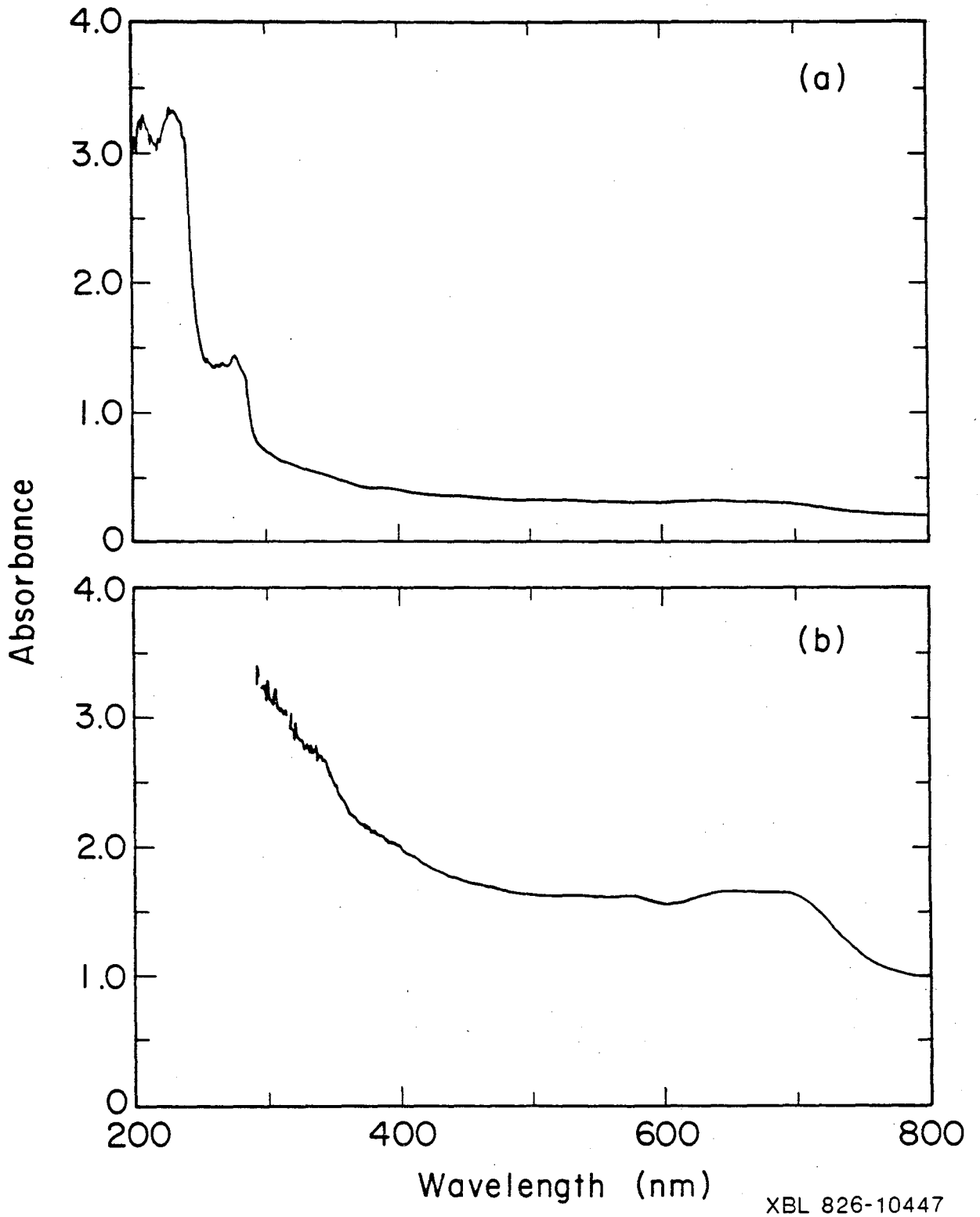
4.0
3.0
2.0
1.0
0
(a)
4.0
3.0
2.0
1.0
0
(b)
Absorbance
200
400
600
800
Wavelength (nm)
XBL 826-10447

Figure II-13

Figure II-14a. Dynode chain wiring diagram for EMI 9824B photomultiplier.

b. Dynode chain wiring diagram for RCA C31034 photomultiplier.

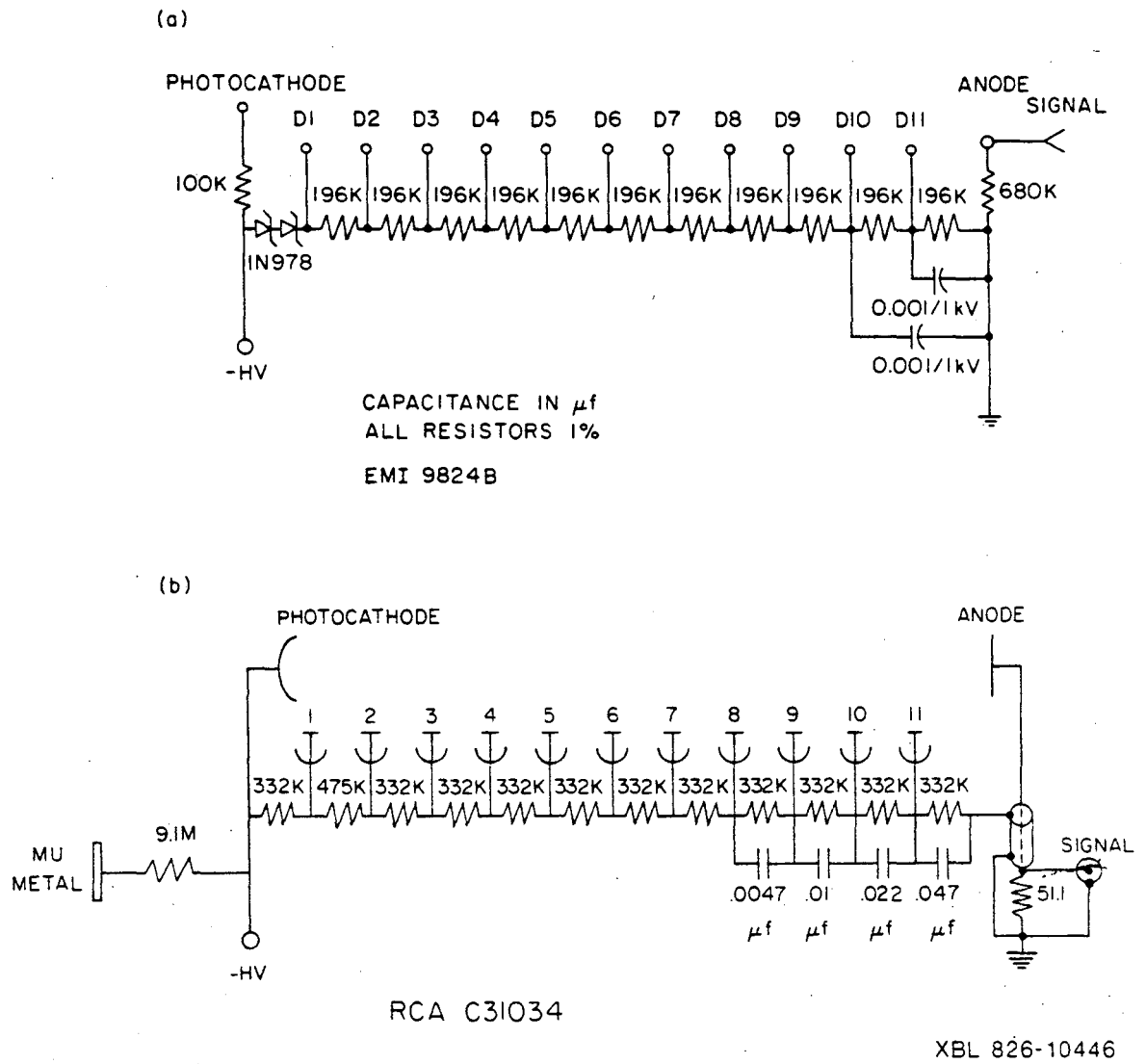
(a)
PHOTOCATHODE
ANODE
SIGNAL
D1 D2 D3 D4 D5 D6 D7 D8 D9 D10 D11
100K
196K 196K 196K 196K 196K 196K 196K 196K 196K 196K 196K
680K
IN978
0.001/1kV
0.001/1kV
-HV
CAPACITANCE IN μf
ALL RESISTORS 1%
EMI 9824B
(b)
PHOTOCATHODE
ANODE
1 2 3 4 5 6 7 8 9 10 11
332K 475K 332K 332K 332K 332K 332K 332K 332K 332K 332K 332K
9.1M
MU METAL
SIGNAL
.0047 μf
.01 μf
.022 μf
.047 μf
51.1
-HV
RCA C31034
XBL 826-10446

Figure II-14

Figure II-15. Assembly diagram of fluorescence access port.

1) Pressure distribution ring
2) Window support housing
3) Window support housing-flange O-ring seal
4) Interaction chamber-flange O-ring seal
5) Positioning pressure support clamp
6) Quartz window pressure plate
7) Quartz window O-ring seal
8) Quartz window
9) Interaction chamber wall
10) O-ring pressure ring
11) O-ring pressure applicator

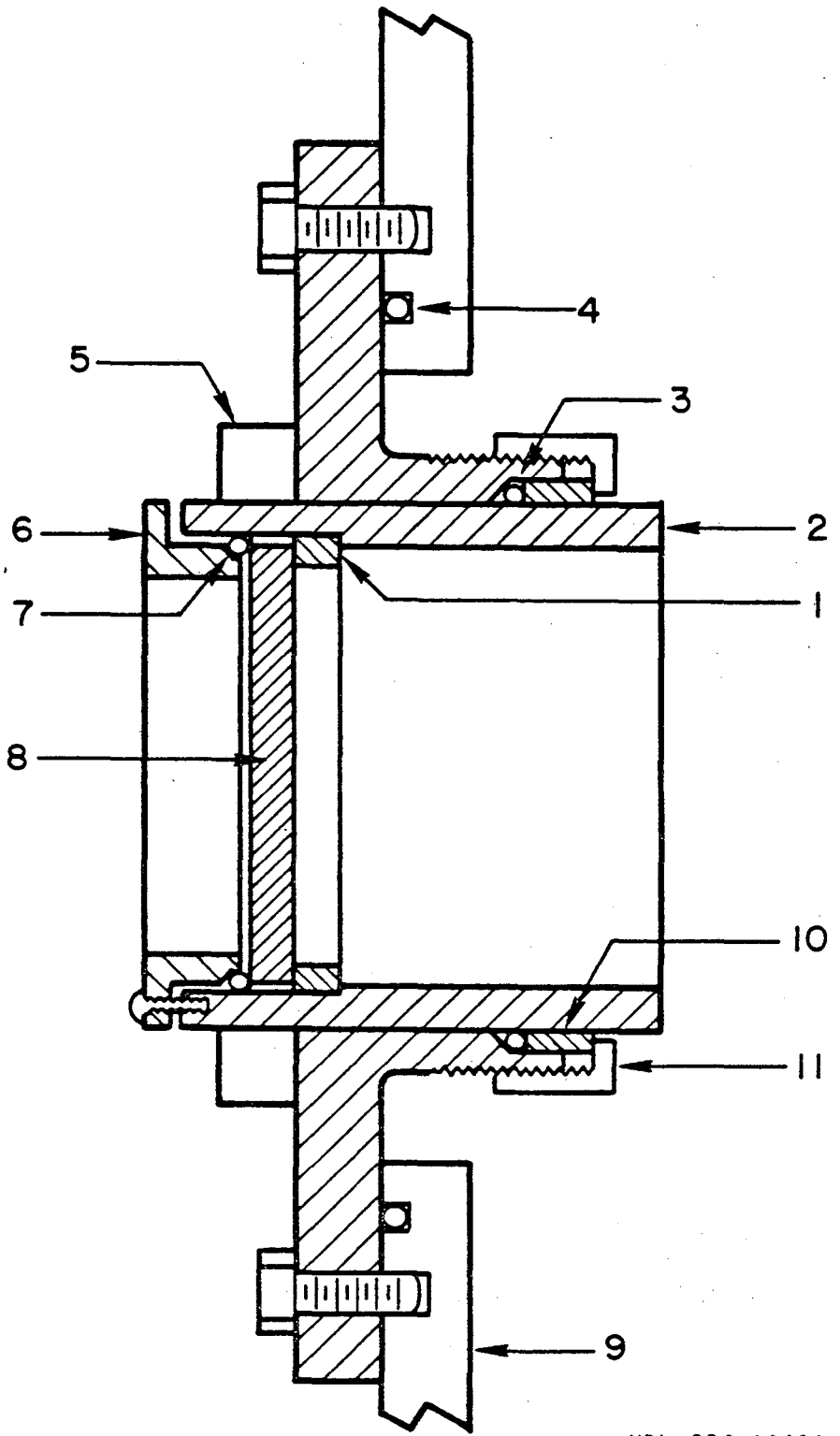

Figure II-15

Figure II-16. Blowup drawing of the cryopump assembly.

A) Cryopump body

B) Cryopump baffle #1

C) Cryopump baffle #2

D) Cryopump baffle #3

E) Cryopump baffle #4

F) LN_2 feed tubes

G) Cryopump slip-on cover

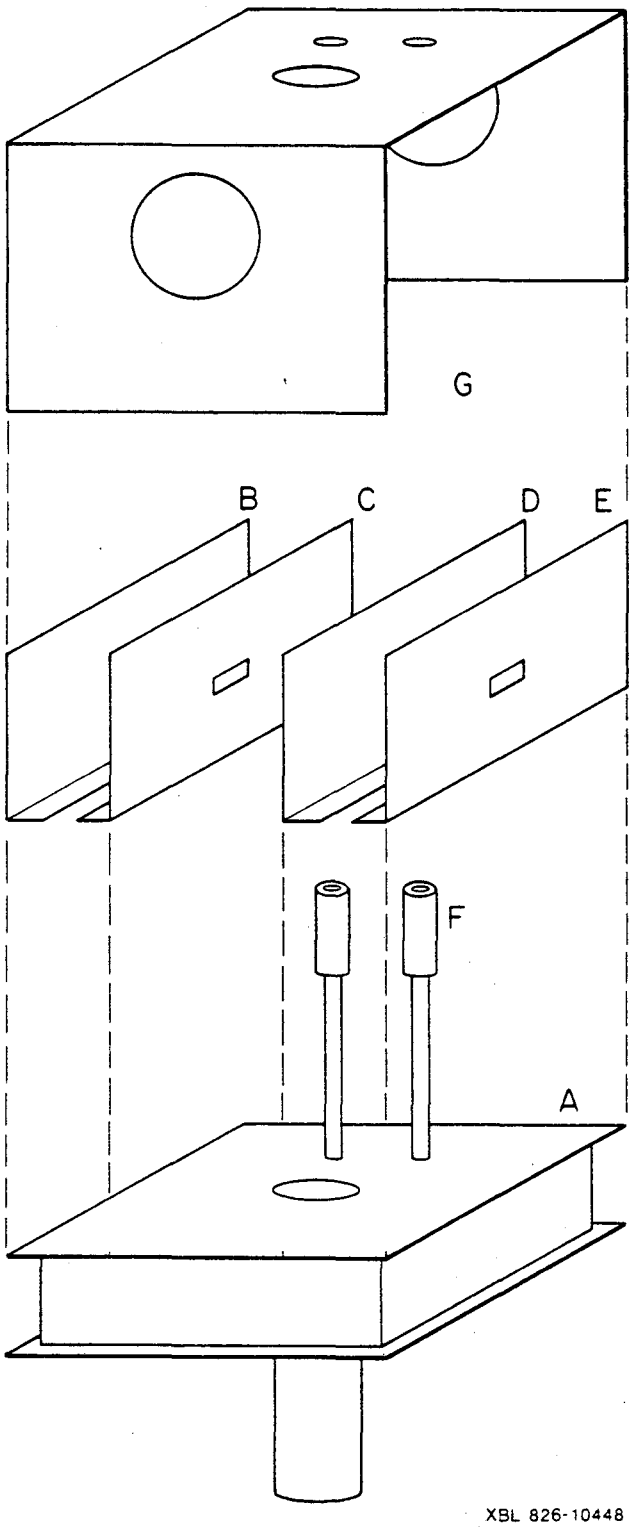

Figure II-16

Figure II-17. Assembly drawing of the pyrolyzer.

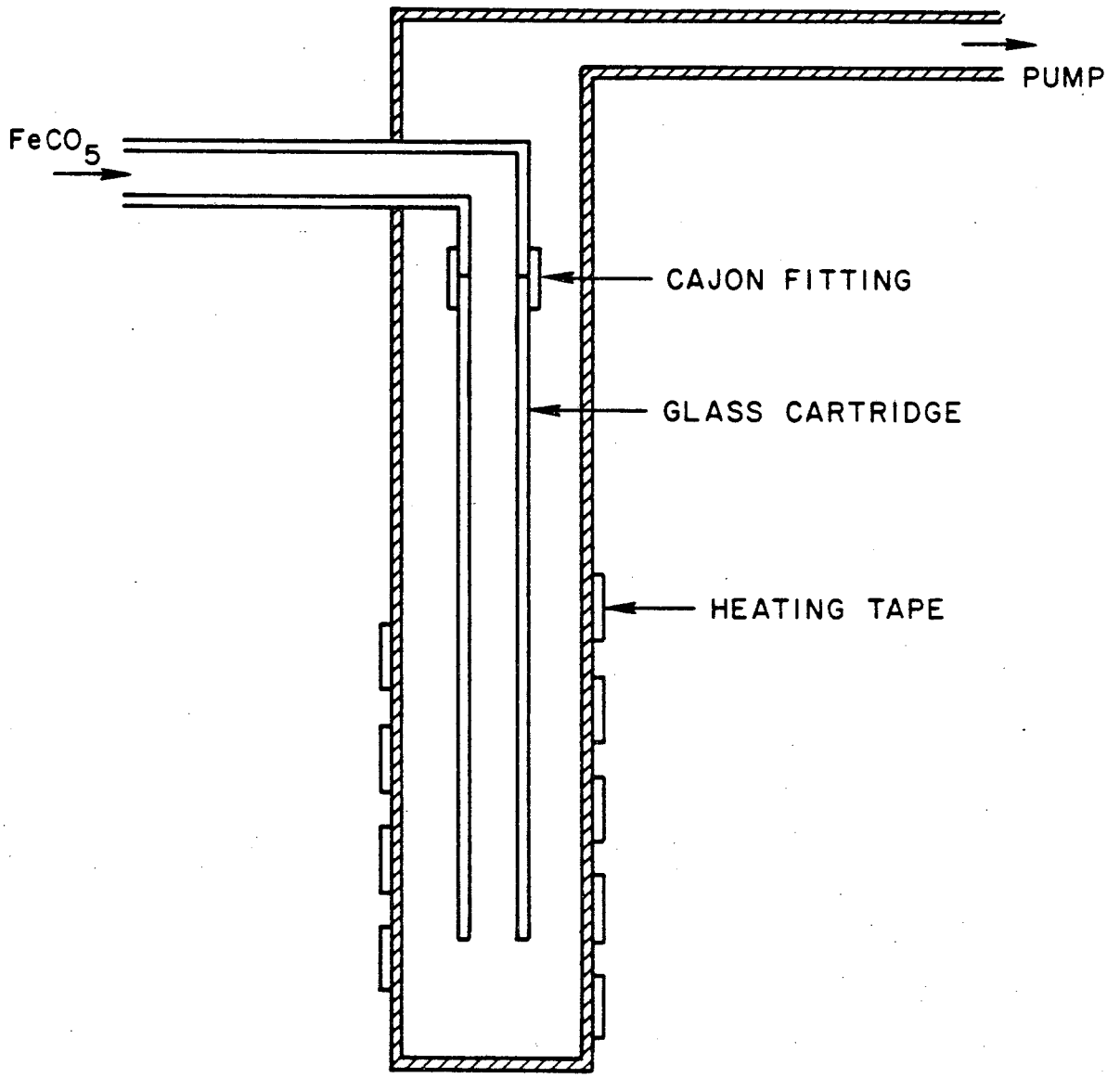
PUMP
$FeCO_5$
CAJON FITTING
GLASS CARTRIDGE
HEATING TAPE
XBL 826-10425

Figure II-17

Figure II-18. Assembly drawing and positioning of the beam nozzle and ion collection electrode with electrical connections.

1) Cryopump baffle #1

2) Cryopump baffle #2

3) Cryopump body

4) Beam nozzle positioning tube

5) Teflon insulator

6) Polished copper ion collection electrode

7) Beam nozzle

8) Virtual beam source

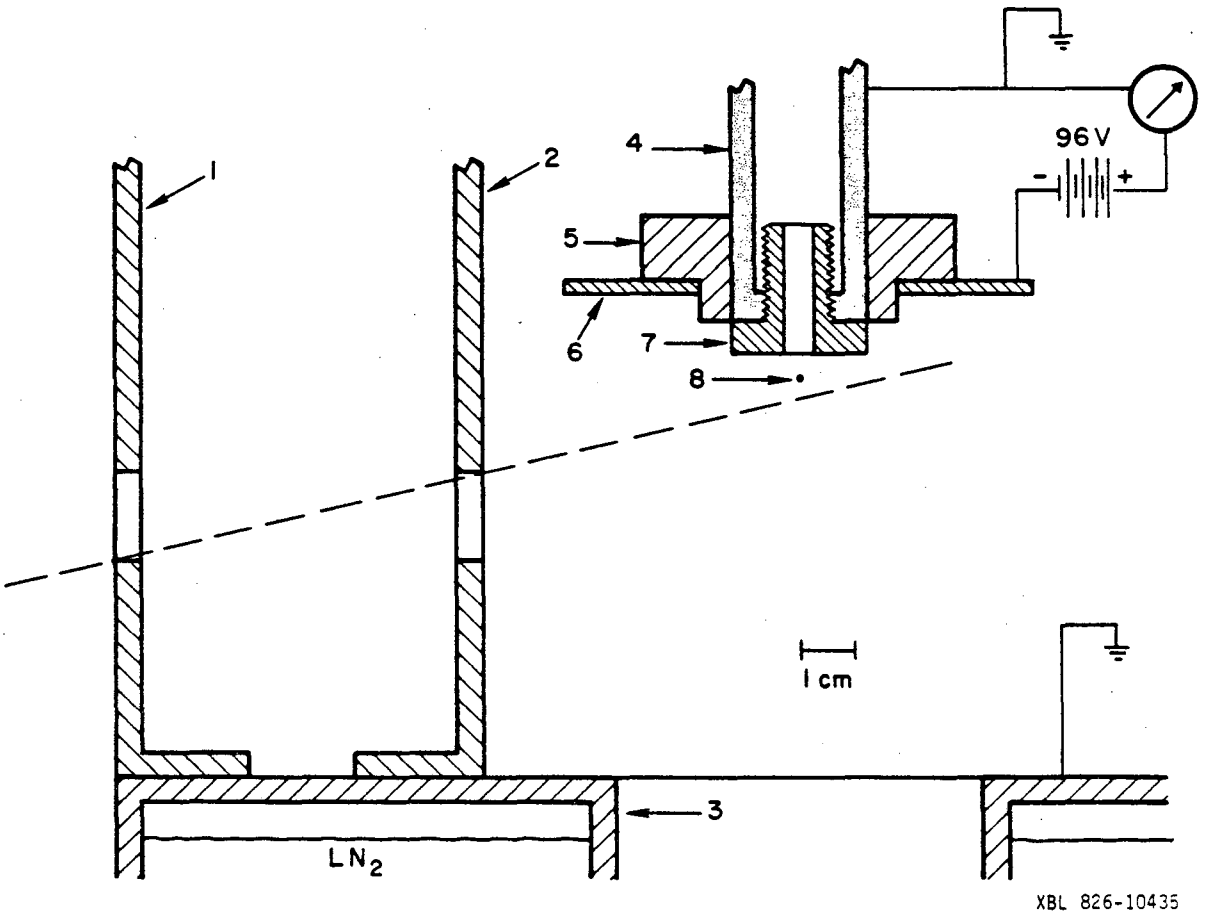

Figure II-18

Figure II-19. Block diagram of detection and experimental control electronics.

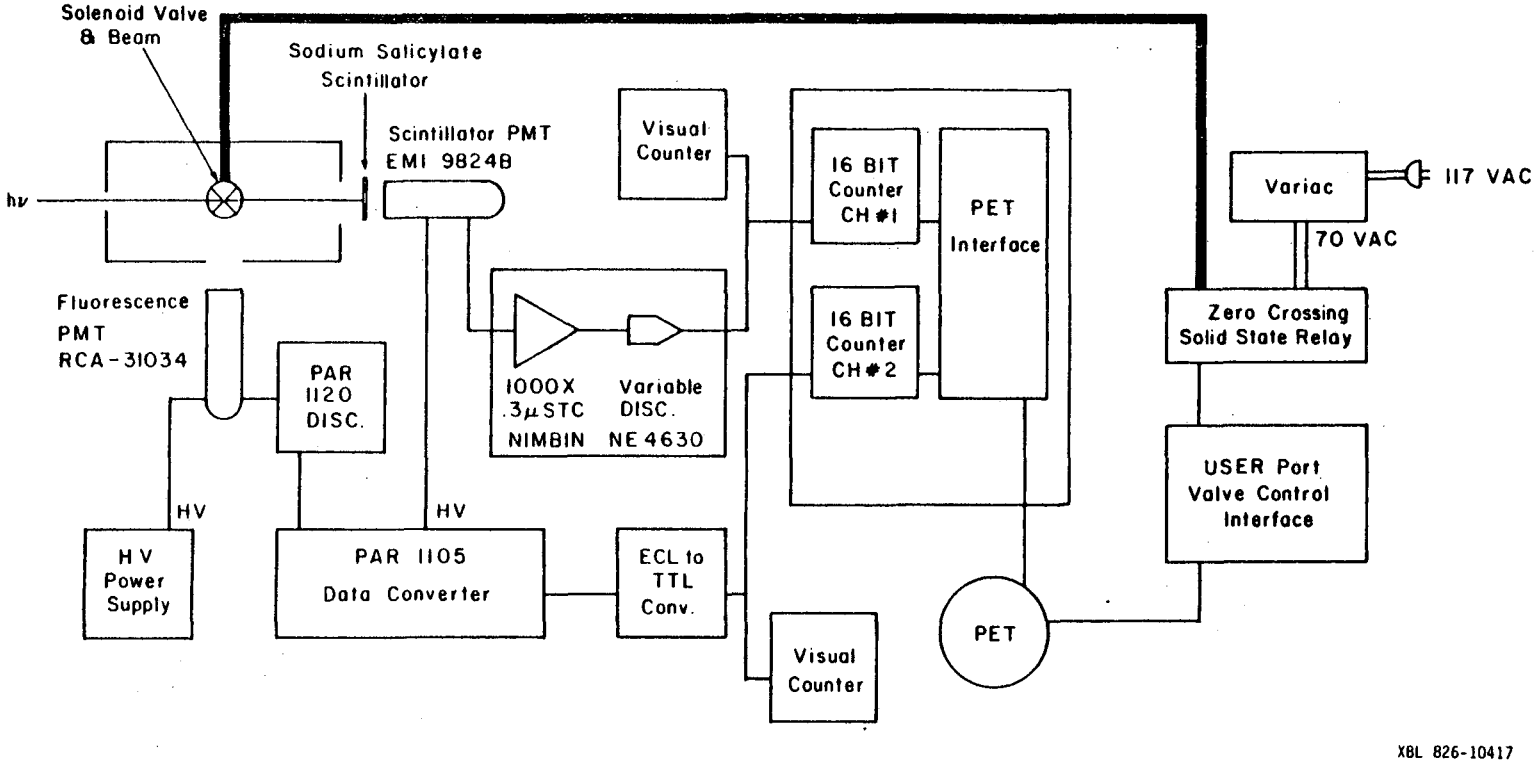
Solenoid Valve
& Beam
Sodium Salicylate
Scintillator
Scintillator PMT
EMI 9824B
hν
Visual
Counter
16 BIT
Counter
CH#1
PET
Interface
Variac
117 VAC
70 VAC
Fluorescence
PMT
RCA-31034
PAR
1120
DISC.
1000X
.3μSTC
NIMBIN
Variable
DISC.
NE4630
16 BIT
Counter
CH#2
Zero Crossing
Solid State Relay
USER Port
Valve Control
Interface
HV
HV
HV
Power
Supply
PAR 1105
Data Converter
ECL to
TTL
Conv.
Visual
Counter
PET
XBL 826-10417

Figure II-19

Figure II-20. Block diagram of the counting interface.

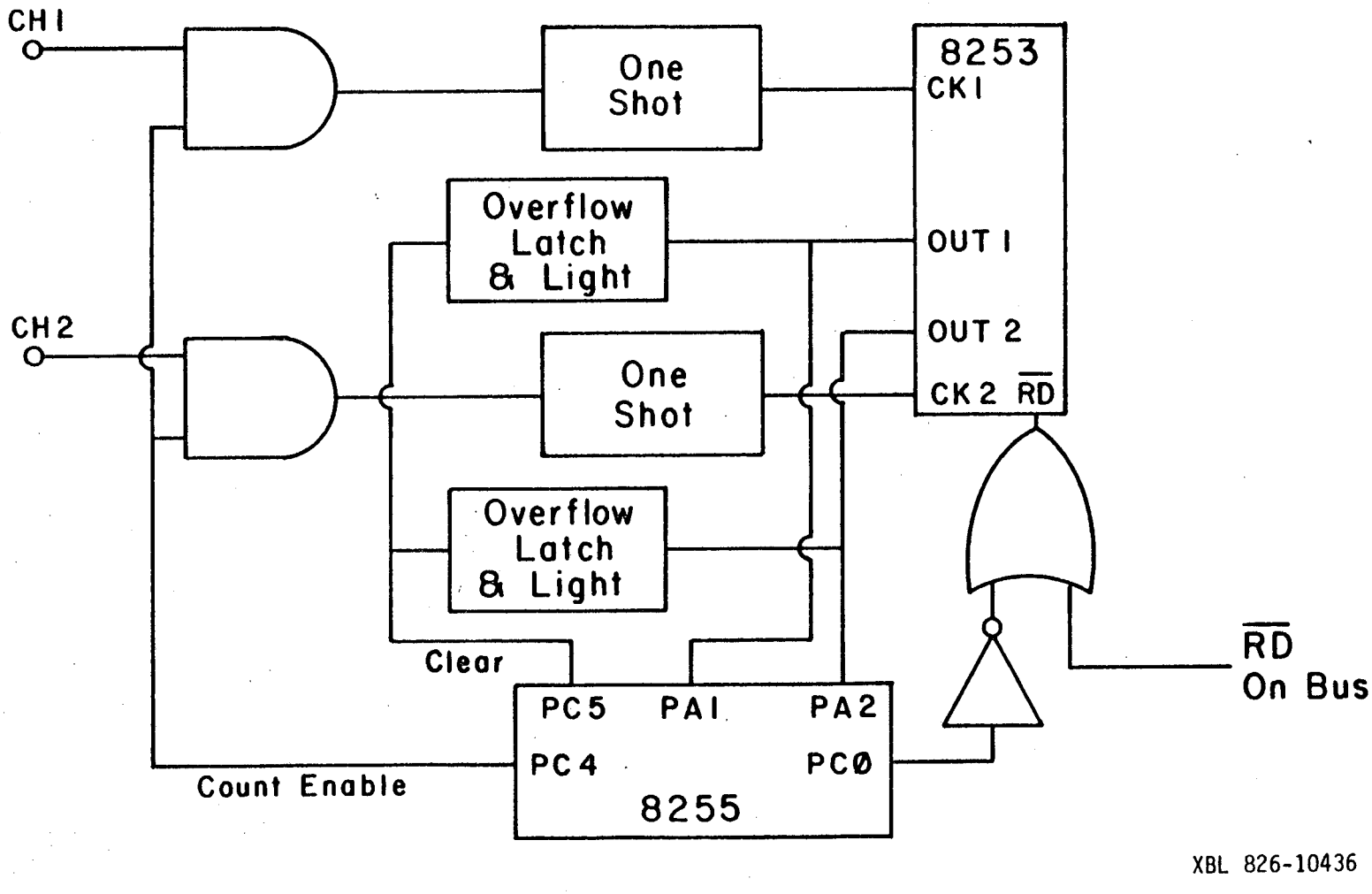
CH1
CH2
One Shot
Overflow Latch & Light
One Shot
Overflow Latch & Light
8253
CK1
OUT 1
OUT 2
CK2 RD
Clear
PC5
PA1
PA2
PC4
PC0
8255
Count Enable
RD On Bus
XBL 826-10436

Figure II-20

CHAPTER III

EXPERIMENTAL PROCEDURE AND RESULTS

The experiments performed to understand the interaction between VUV radiation and $Fe(CO)_5$ can be grouped into four distinct sections:

A) undispersed quantum fluorescence yield experiments,

B) dispersed fluorescence and chemiluminescence yield experiments,

C) quantum photoionization yield experiment, and

D) beam absorption experiment.

Each section is further divided into discussions of experimental procedure and data reduction and results. A discussion of all the results and an analysis of them will follow in Chapter IV. While each section will be discussed in detail separately, the operation of the discharge lamp and beam apparatus is described first since they are used in all four sections.

Lamp Operation

In all experiments where VUV light was used, the lamp was operated as follows:

1) Turn on the power supply for warm-up.

2) Close and seal the slit in the entrance arm of the Seya-Namioka monochromator.

3) Open the cathode pump valve V1 (see Fig. II-5) and adjust the discharge gas pressure (see Table II-1) inside the lamp.

4) Select maximum ballast resistance.

5) Start discharge by applying high voltage (~-1000 V) to the cathode and turn the cooling water on.

6) Run for ~20 minutes.

7) Open slit to the monochromator and adjust voltage, current, pressure and pumping configuration for maximum light output.

8) Allow to run for ~20 minutes.

9) Repeat steps 7 and 8 until light output is stable and optimized. Typical maximum light output conditions are shown in Table II-1.

Beam and Cryopump Operation

In all the experiments where the $Fe(CO)_5$ beam was required, the operation sequence was as follows:

1) Turn on the interaction chamber diffusion pump to bring the chamber pressure to ~1 x 10^{-6} torr.

2) Cool and fill the cryopump with LN_2.

3) Bring the $Fe(CO)_5$ bulb to 31.7°C via the hot water bath.

4) Allow the system to equilibrate for about two hours to allow the nozzle temperature to rise to ~20°C. (The N_2 boil-off during cryopump cooling cools the entire beam assembly, resulting in nozzle temperatures of 10°C or less.)

5) Pump out the excess CO accumulated in the $Fe(CO)_5$ bulb directly to the pyrolyzers.

6) Slowly open the manual valve between the $Fe(CO)_5$ bulb and the interaction chamber so as not to trip the pressure interlock on the DP.

7) Repeat step 6 in ten minute intervals until no increase in pressure registers in the interaction chamber, with full beam flux.

8) After satisfying the conditions in the previous step, open the gate valve into the monochromator.

A. Undispersed Quantum Fluorescence Yield Experiments

1) Experimental procedure

To determine the relative quantum fluorescence yield, a ratio of the relative number of photons emitted to the relative number absorbed has to be measured. This ratio has to be determined over the pertinent range of available vacuum ultraviolet excitation energies. The approach is slightly different for the hydrogen continuum source and rare gas resonance lines, and each will be discussed separately.

a) Hydrogen lamp excitation undispersed quantum fluorescence yield

The timing sequence used to gather data for each channel is shown in Figure III-1. A channel duration of 60 seconds in conjunction with a VUV monochromator scan speed of 5 Å/min was chosen giving 5 Å/channel. This was judged a sufficiently low scan rate considering that the band pass of the VUV monochromator with 1000 μm slits was approximately 10 Å. Further, the sampling rate per channel was effectively doubled by splitting the beam-on-time segments equally between the beginning and the end of the channel. This timing sequence was chosen over a true doubling of sampling rate (beam on, off, on, off) to eliminate the need for a second 'dead time' in the sequence. Following the beam valve shutoff, a time window, during which no accumulation of data occurs, was required to allow all the $Fe(CO)_5$ to leave the 20 cm conduction tube between the solenoid shutoff valve and the nozzle, so that a true beam-off condition was achieved.

The range of excitation wavelengths had to be divided between two experiments, one from 850 to 1100 Å, and the second, 1100 to 1300 Å, for two reasons. First, the length of the experiment was limited to

approximately 30 minutes of $Fe(CO)_5$ beam-on time. This translates to a total scan of 300 Å (60 channels). This time limit was imposed by the observation that condensation of solid $Fe(CO)_5$ in the cryopump starts to close off the openings in the second and third baffles. After 60 to 70 channels were collected, the signal to noise ratio begins to decrease drastically. Secondly, the hydrogen lamp output significantly increases above 1100 Å, requiring an insertion of an additional neutral density filter between the scintillator and the EMI PMT. To ensure correct normalization between these two scans, a third scan was run from 950 to 1200 Å.

In order to complete the data reduction discussed in Section III-A-2, an additional measurement of scattered light was carried out prior to the start of each scan. The same timing pattern was used, but the VUV monochromator was tuned to 800 Å, where the hydrogen lamp produces no radiation. Six channels were recorded at this wavelength to provide statistically better data.

b) Rare gas lamp excited undispersed quantum fluorescence yield

The data acquisition for experiments using rare gas emission lines used the same data taking pattern as experiments which used hydrogen pseudo-continuum excitation. The difference was that the VUV monochromator was not scanned, but tuned to the desired VUV emission wavelength for the duration of six channels each. The wavelengths for the eight data sets recorded are shown in Table III-1. If the comparison of data sets gathered for different discharge gases is to be valid, the data have to be gathered under identical experimental conditions. To guarantee this consistency, both fluorescence and scintillation measurements for all five rare gas emission wavelengths were gathered during the same experiment.

2) Data reduction and results

Since the experimental excitation wavelength used in these experiments was in the VUV, the scattered light component of the overall radiation emitted from the monochromator is much greater than at UV or visible wavelengths. In order to eliminate the scattered light contributions to the data sets, an in-depth analysis of the signal contributions to each data set was required. The light from the Seya-Namioka monochromator was separated into two parts - the selected wavelength and scattered light.

The label 'scattered light' is used rather loosely to include any photon energies other than the one selected by the monochromator. They will include VUV, UV and visible photons. Because of this, their actions in absorption and excitation had to be separated from the actions of the selected photons. The results are shown in Figures III-2 and III-3. Variables are labelled following the convention shown in the table below.

Symbol	Position	Meaning
F	Main	Fluorescence
S	Main	Scintillation
+	Superscript	Beam on
-	Superscript	Beam off
λ	Subscript	Selected wavelength
SC	Subscript	Scattered light
DC	Subscript	Dark counts
$\Sigma+$	Subscript	Pulse count while selected excitation photons are present
$\Sigma-$	Subscript	Pulse count while selected excitation photons are absent

The four sets of data acquired during either the scans of the hydrogen lamp or the resonance light excitation experiments are shown below:

$$F^{+}_{\Sigma+} = F^{-}_{\lambda} + F^{-}_{SC} + F^{+}_{\lambda} + F^{+}_{SC} + F_{DC} \qquad \text{(III-1)}$$

$$F^{-}_{\Sigma+} = F^{-}_{SC} + F^{-}_{\lambda} + F_{DC} \qquad \text{(III-2)}$$

$$S^{+}_{\Sigma+} = S^{+}_{SC} + S^{+}_{\lambda} + S_{DC} \qquad \text{(III-3)}$$

$$S^{-}_{\Sigma+} = S^{-}_{SC} + S^{-}_{\lambda} + S_{DC} \,. \qquad \text{(III-4)}$$

The desired quantity, the quantum fluorescence yield, is defined as the ratio:

$$\frac{\text{Total \# of photons emitted}}{\text{Total \# of photons absorbed}}$$

or

$$\frac{F^{+}_{\lambda}}{S^{-}_{\lambda} - S^{+}_{\lambda}} \,. \qquad \text{(III-5)}$$

In the first step of data reduction, a subtraction is carried out yielding:

$$\begin{aligned} F^{+}_{\Sigma+} - F^{-}_{\Sigma+} &= (F^{-}_{\lambda} + F^{-}_{SC} + F^{+}_{\lambda} + F^{+}_{SC} + F_{DC}) - (F^{-}_{SC} + F^{-}_{\lambda} + F_{DC}) \\ &= F^{+}_{\lambda} + F^{+}_{SC} \end{aligned} \qquad \text{(III-6)}$$

and

$$\begin{aligned} S^{-}_{\Sigma+} - S^{+}_{\Sigma+} &= (S^{-}_{\lambda} + S^{-}_{SC} + S_{DC}) - (S^{+}_{\lambda} + S^{+}_{SC} + S_{DC}) \\ &= S^{-}_{\lambda} + S^{-}_{SC} - S^{+}_{\lambda} - S^{+}_{SC}. \end{aligned} \qquad \text{(III-7)}$$

The quotient of (III-6) to (III-7) is usually accepted during UV and visible fluorescence experiments because the scattered light contributions (F^+_{SC}, S^-_{SC}, and S^+_{SC}) are negligible. However, in VUV photolysis, particularly at the higher energies used in our experiment, the scattered light terms can no longer be neglected. They are factored out using the four additional data sets gathered when the VUV monochromator was tuned to 800 Å (where the lamp had no VUV emission). These data gave the following four quantities:

$$F^-_{\Sigma-} = F^-_{SC} + F_{DC} \tag{III-8}$$

$$F^+_{\Sigma-} = F^-_{SC} + F^+_{SC} + F_{DC} \tag{III-9}$$

$$S^-_{\Sigma-} = S^-_{SC} + S_{DC} \tag{III-10}$$

$$S^+_{\Sigma-} = S^+_{SC} + S_{DC} \,. \tag{III-11}$$

Carrying out subtractions as above yields

$$\begin{aligned} F^+_{\Sigma-} - F^-_{\Sigma-} &= (F^-_{SC} + F^+_{SC} + F_{DC}) - (F^-_{SC} + F_{DC}) \\ &= F^+_{SC} \end{aligned} \tag{III-12}$$

and

$$\begin{aligned} S^-_{\Sigma-} - S^+_{\Sigma-} &= (S^-_{SC} + S_{DC}) - (S^+_{SC} + S_{DC}) \\ &= S^-_{SC} - S^+_{SC} \,. \end{aligned} \tag{III-13}$$

Subtracting Equation (III-12) from (III-6) and (III-13) from (III-7) yields

$$F^+_{\Sigma+} - F^-_{\Sigma+} - (F^+_{\Sigma-} - F^-_{\Sigma-}) = F^+_{\lambda} \tag{III-14}$$

and

$$S^-_{\Sigma+} - S^+_{\Sigma+} - (S^-_{\Sigma-} - S^+_{\Sigma-}) = S^-_{\lambda} - S^+_{\lambda} \,. \tag{III-15}$$

The ratio of (III-14) to (III-15) gives the quantum fluorescence yield as defined in Equation (III-5). During this data analysis, an assumption was made that F_{SC}^{+} and $S_{SC}^{-} - S_{SC}^{+}$ were constant over the entire range of the data treatment. In the case of data gathered using rare gas lines for excitation, this assumption is easily justified by the small wavelength difference in the setting of the VUV monochromator between the $\Sigma-$ and the $\Sigma+$ data sets. However, this is not the case with the hydrogen lamp data where the $\Sigma+$ and $\Sigma-$ data sets were separated by as much as 600 Å. Here the validity of the assumption lies in the magnitude of the numbers involved. The non-linearity of F_{SC}^{+} and $S_{SC}^{-} - S_{SC}^{+}$ would not be a factor if their contribution to the signal were small, i.e., if

$$S_{\lambda}^{-} - S_{\lambda}^{+} >> S_{SC}^{-} - S_{SC}^{+}, \text{ and} \qquad \text{(III-16)}$$

$$F_{\lambda}^{+} >> F_{SC}^{+}.$$

These conditions were satisfied except in two regions of the hydrogen lamp excited quantum fluorescence curve. The first is the region below 1000 Å where the lamp output is very low, causing conditions (III-16) to be violated. However, this region is sufficiently close to 800 Å, the wavelength where the $\Sigma-$ data were taken, so that the original assumption of linearity can still be considered valid. The second region is above 1250 Å, where the fluorescence signal is very small due to a small fluorescence cross-section. This causes the violation of the condition in Equation (III-17). Since there was no way of obtaining the values for F_{SC}^{+} in this region, the data had to be discarded.

The composite quantum fluorescence yield data on iron pentacarbonyl are shown in Figure III-4. The relative positioning of the rare gas-excited data points and the hydrogen-excited scans is accomplished by scaling

the data sets with respect to each other until the relative quantum fluorescence yield values are equal. The error bars represent statistical error. The rare gas data and hydrogen data between 10.3 and 12.5 eV (containing ~70% of the data) have statistical errors <3%.

Conveniently, the relative quantum fluorescence yield data obtained here are independent of the variation in the long term beam density and VUV photon flux (long term being long with respect to the one minute sampling rate), but are sensitive to their short term fluctuations (which were on the order of the data sampling rate, ~15 sec). The beam density fluctuations were of a longer term and are discussed in detail in Section III-D. On the other hand, the VUV photon flux has both long and short term fluctuations. The long term decrease is mainly due to the 'aging' of lamp electrodes and to the restriction of the light path by solid $Fe(CO)_5$ accumulation on the second baffle of the cryopump. The short term fluctuations are due primarily to the instability in the lamp discharge, which was impossible to control without a current regulated power supply. These fluctuations are responsible for the 'wiggles' on the quantum fluorescence yield curve.

B. Dispersed Fluorescence and Chemiluminescence Yield Experiments

The study of dispersed iron emission was divided into two sections:

1) dispersed VUV-induced iron fluorescence and

2) dispersed rare-gas-metastable-induced iron chemiluminescence.

The latter is a duplication of the experiment first done by Hartman[1] using different data acquisition techniques.

1) VUV excitation

a) Experimental procedure

The experiments which involved gathering dispersed iron fluorescence were plagued by one major problem: a very low signal. This imposed the following limitations on our experiment. The low intensity of the hydrogen pseudocontinuum as a light source was unacceptable. limiting experiments to the discrete energies of the rare gas emissions in neon and argon. For neon, the VUV monochromator was tuned to 1066 Å, the most intense emission. With argon, the VUV monochromator had to be turned to zero order for the experiment to produce sufficient iron fluorescence. This allowed both 10.67 and 10.87 eV radiation as well as a host of UV and visible lines into the interaction region. Since none of the UV lines were between 3500 and 3900 Å, they did not interfere with the experiment.

In order to maximize the amount of fluorescence being gathered, the 0.25 m JA monochromator was fitted with 1000 μm slits. This resulted in a decrease in resolution to about 15 Å FWHM while increasing the total transmission. The detection monochromator bandwidth measurement, shown in Figure III-5, was achieved by observing mercury pen lamp emission lines through the fluorescence detection setup. The pertinent range of fluorescence dispersal is from ~3500 to 3900 Å. Given the very low signal, this region was divided into only 20 channels of 20 Å each. A 5 Å/min monochromator scan speed allowed four minutes of counting time per channel, yielding a larger signal-to-noise ratio. The data gathering pattern is shown in Figure III-6. A 60-second data gathering sequence is repeated within each channel increasing the sampling rate four-fold.

b) Data reduction and results

The four data sets gathered during these experiments with the appropriate symbols are:

i) dispersed fluorescence signal, beam on, $F^{+}_{\Sigma+}$

ii) dispersed fluorescence signal, beam off, $F^{-}_{\Sigma+}$

iii) VUV photon flux, beam on, $S^{+}_{\Sigma+}$

iv) VUV photon flux, beam off, $S^{-}_{\Sigma+}$.

These four data sets are all that were required for data reduction. Condition (III-16) was satisfied in the neon lamp excitation because the VUV monochromator was tuned to a resonance line which is by far the strongest contribution to the signal. In the argon lamp case, when the monochromator was tuned to zero order, the scintillator not only registered the VUV lines, but also a host of lines between 3949 and 4334 $\mathring{A}^2$. (The lines to the red of the 6965 $\mathring{A}$ line were not monitored since the EMI PMT is blind in that region.) The result is a violation of condition (III-16), necessitating the use of the beam density profile gathered in the neon lamp experiment to correct the argon excited dispersed fluorescence signal for beam flux variation. This substitution is valid because the curves showed excellent qualitative reproducibility, from experiment to experiment.

Condition (III-17) was satisfied in both experiments since no lamp emission in the region from 3500 to 3900 $\mathring{A}$ could reach the interaction region, leaving inelastic scattering as the only scattered light contributor. Not only is the inelastic scattering cross-section small, but when it was dispersed, its contribution to $F^{+}_{\Sigma+}$ could be eliminated. This allows one to write:

$$F^{+}_{\Sigma+} = F^{-}_{\lambda} + F^{-}_{SC} + F^{+}_{\lambda} + F_{DC} \qquad \text{(III-18)}$$

$$F^{-}_{\Sigma+} = F^{-}_{\lambda} + F^{-}_{SC} + F_{DC} \qquad \text{(III-19)}$$

$$S^{+}_{\Sigma+} = S^{+}_{\lambda} + S_{DC} \qquad \text{(III-20)}$$

$$S^{-}_{\Sigma+} = S^{-}_{\lambda} + S_{DC}. \qquad \text{(III-21)}$$

In this data reduction, simple subtraction and ratioing give the quantum fluorescence as defined in (III-5). The dispersed quantum fluorescence spectra of $Fe(CO)_5$ excited by a neon and an argon lamp are shown in Figures III-7a and III-8a, respectively. The low signal gathered in the argon excitation allowed the data for only one peak to be statistically significant.

2) Metastable excitation

a) Experimental procedure

As a comparison to VUV photon induced fluorescence, a rare gas metastable excited chemiluminescence spectrum was measured with the apparatus described by Hartman.[1] In short, rare gas metastables are produced in a hollow cathode discharge at pressures of ~1 torr. After a 35 cm drift length, they collide with $Fe(CO)_5$ which was allowed to enter the chamber through a metered valve. The resultant chemiluminescence was observed through a window by the detection system with the same resolution used to gather data in Section III-B-1. However, since the signal was considerably stronger than the VUV counterpart, a 250 Å/min scan speed with a 4.8 sec/channel dwell time was used to produce the desired 20 Å/channel resolution.

b) Data reduction and results

The experimental apparatus had no provision for monitoring both the signal and the background within the same channel, i.e., no provision to turn the $Fe(CO)_5$ flow on and off. This necessitated two

separate scans over the same wavelength range, one with $Fe(CO)_5$ and the other without, yielding two data sets, $F^+_{\Sigma+}$ and $F^-_{\Sigma+}$. The difference between these data sets is all that was required for a chemiluminescence spectrum because the concentration of rare gas metastables was constant over the duration of the experiment. The low resolution chemiluminescence spectrum obtained for $Fe(CO)_5$ upon collision with metastable neon is shown in Figure III-7b and with metastable argon in Figure III-8b.

C. Photoionization Yield Experiment

1) Experimental procedure

The major constraint imposed on the data collection in the experiment measuring quantum photoionization of $Fe(CO)_5$ was the long time constant associated with the current measurement. It was ~10 sec, a value inherent to the Keithley electrometer used to measure the photoion current. The wavelength scan of the hydrogen lamp was accomplished by manually stepping the VUV monochromator in 20 Å steps. The data taking pattern is shown in Figure III-9. A 10 sec (600 jiffies) dead time was provided at the start of each channel to allow 1) $Fe(CO)_5$ to dissipate from the nozzle, producing a true no beam situation, and 2) the experimenter to step the monochromator manually to a new wavelength.

The experiment yielded three data sets:

i) net photocurrent,

ii) VUV photon flux, beam on, and

iii) VUV photon flux, beam off.

2) Data reduction and results

The quantum ionization yield is simply the ratio of

$$\frac{\#\text{ ions out}}{\#\text{ photons in}} \qquad \text{(III-22)}$$

The average result of the photoionization experiment is shown in Figure III-10.

D. Beam Absorption

1) Experimental procedure

The timing sequence is identical to that used for the quantum fluorescence yield and is shown in Figure III-1. The 0.25 m JA monochromator was either kept at one wavelength (in the case of the mercury line absorption) or scanned to the red at 20 Å/min (in the case of deuterium lamp absorption). Such a high scan speed is acceptable because the deuterium spectrum has only long term fluctuations associated with its photon flux.

2) Results

The results from the mercury lamp absorption gave an I/I_o value at 2536.5 Å of 0.925. The VUV value for I/I_o at 1170 Å was 0.511. These values are only meant as guides for beam density estimates, since I/I_o is extensive and varies with the beam density. A normal temporal variation of beam density is shown in Figure III-11. It is apparent that the constant temperature bath was inadequate to keep the beam flux constant. The shape of the beam density variation with time appears to be the result of changes in the rate of heat transfer to the liquid from the bath as well as the rate of mass transfer from the liquid to the gas phase, as the level of liquid $Fe(CO)_5$ changed. However, the ratio

$$\frac{\left(\frac{I - I_o}{I}\right)_{2536.5\ \text{Å}}}{\left(\frac{I - I_o}{I}\right)_{1170\ \text{Å}}} = 0.153 \pm 0.012$$

is an intensive quantity independent of beam density and relates to the extinction coefficient at these wavelengths. The uncertainty in this value results from the spread in ratios taken at various times throughout a temporal beam profile such as shown in Figure III-5.

The measurement of the absorption profile in the UV was plagued by scattered light making a data analysis similar to that used in quantum fluorescence necessary. However, again $(I - I_o)/I_o$ in the UV is an extensive variable and had to be corrected by a value proportional to the beam density, i.e., the time dependent $(I_o - I)/I_o$ at 1170 Å. The result was intensive but unitless, serving only to indicate the qualitative absorption profile.

REFERENCES for CHAPTER III

1. D. C. Hartman, Ph.D. Thesis, University of California, LBL Report # 11208 (1980).

2. Typical Spectra of Oriel Spectral Lamps; (Oriel Optics Corp., Connecticut), (supplied with Oriel Pen Lamp Kit #C-13-02).

Table III-1

Data Sets Collected for Rare Gas Excited Undispersed Quantum Fluorescence Yield Experiments

Data Set #	Discharge Gas	Transition	Monochromator Wavelength (Å)
1	Argon	$^1P_1 - {}^1S$	1048.2
2	Argon	$^3P_1 - {}^1S$	1066.7
3	Argon	Scat. Light	1165.0
4	Neon	$^1P_1 - {}^1S$	735.9
5	Neon	$^3P_1 - {}^1S$	743.7
6	Neon	Scat. Light	690.0
7	Helium	$^1P^o - {}^1S$	584.3
8	Helium	Scat. Light	640.0

"for number sequence only"

Figure III-1. Timing sequence used in nondispersed quantum fluorescence data acquisition.

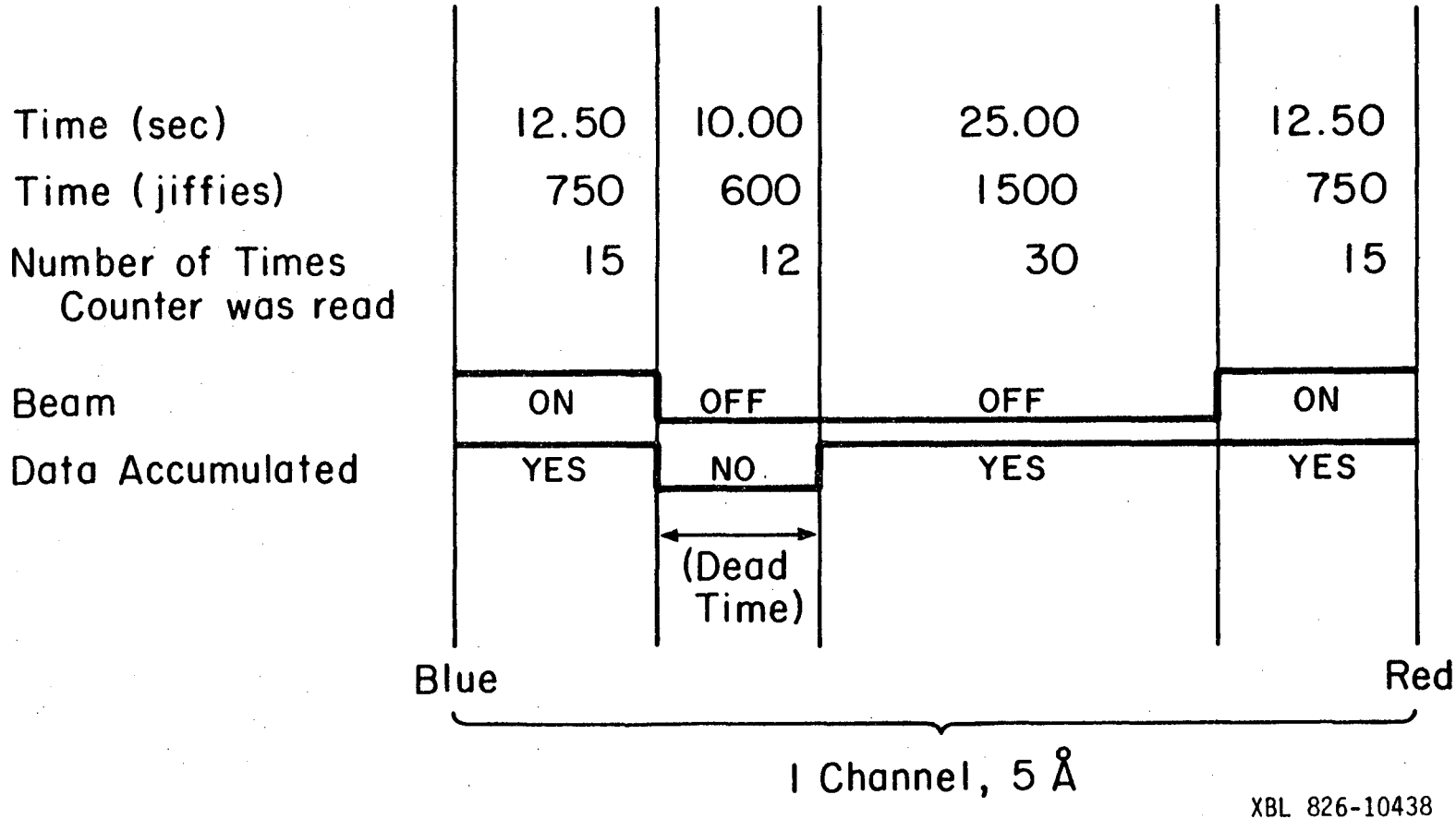
Time (sec)
12.50
10.00
25.00
12.50
Time (jiffies)
750
600
1500
750
Number of Times Counter was read
15
12
30
15
Beam
ON
OFF
OFF
ON
Data Accumulated
YES
NO
YES
YES
(Dead Time)
Blue
Red
1 Channel, 5 Å
XBL 826-10438

Figure III-1

Figure III-2. Pictorial breakdown of contributions to counts gathered in nondispersed quantum fluorescence with $Fe(CO)_5$ beam on.

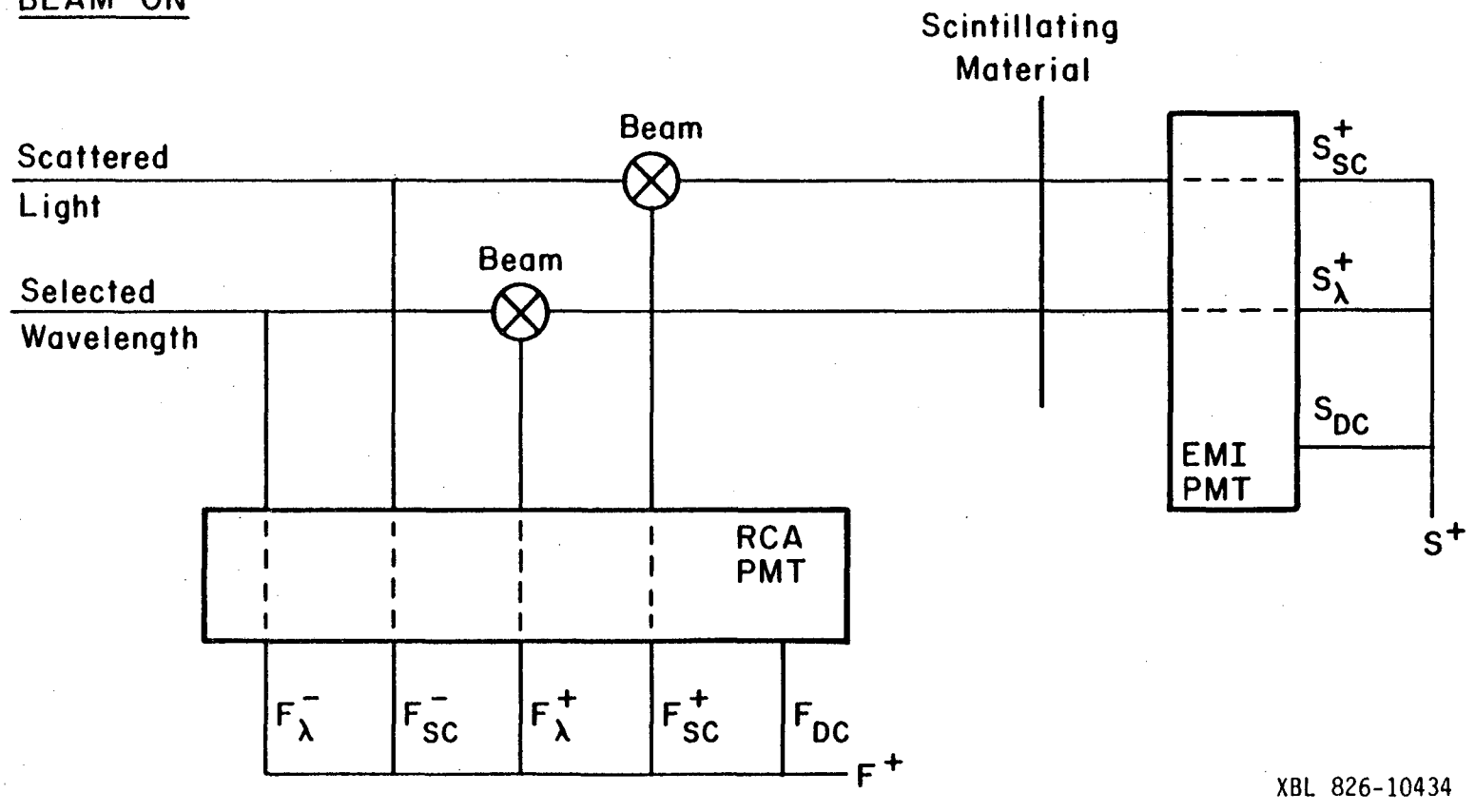
BEAM ON
Scintillating Material
Beam
Beam
Scattered Light
Selected Wavelength
S^+_{SC}
S^+_λ
S_{DC}
EMI PMT
S^+
RCA PMT
F^-_λ
F^-_{SC}
F^+_λ
F^+_{SC}
F_{DC}
F^+
XBL 826-10434

Figure III-2

Figure III-3. Pictorial breakdown of contributions to counts gathered in nondispersed quantum fluorescence with $Fe(CO)_5$ beam off.

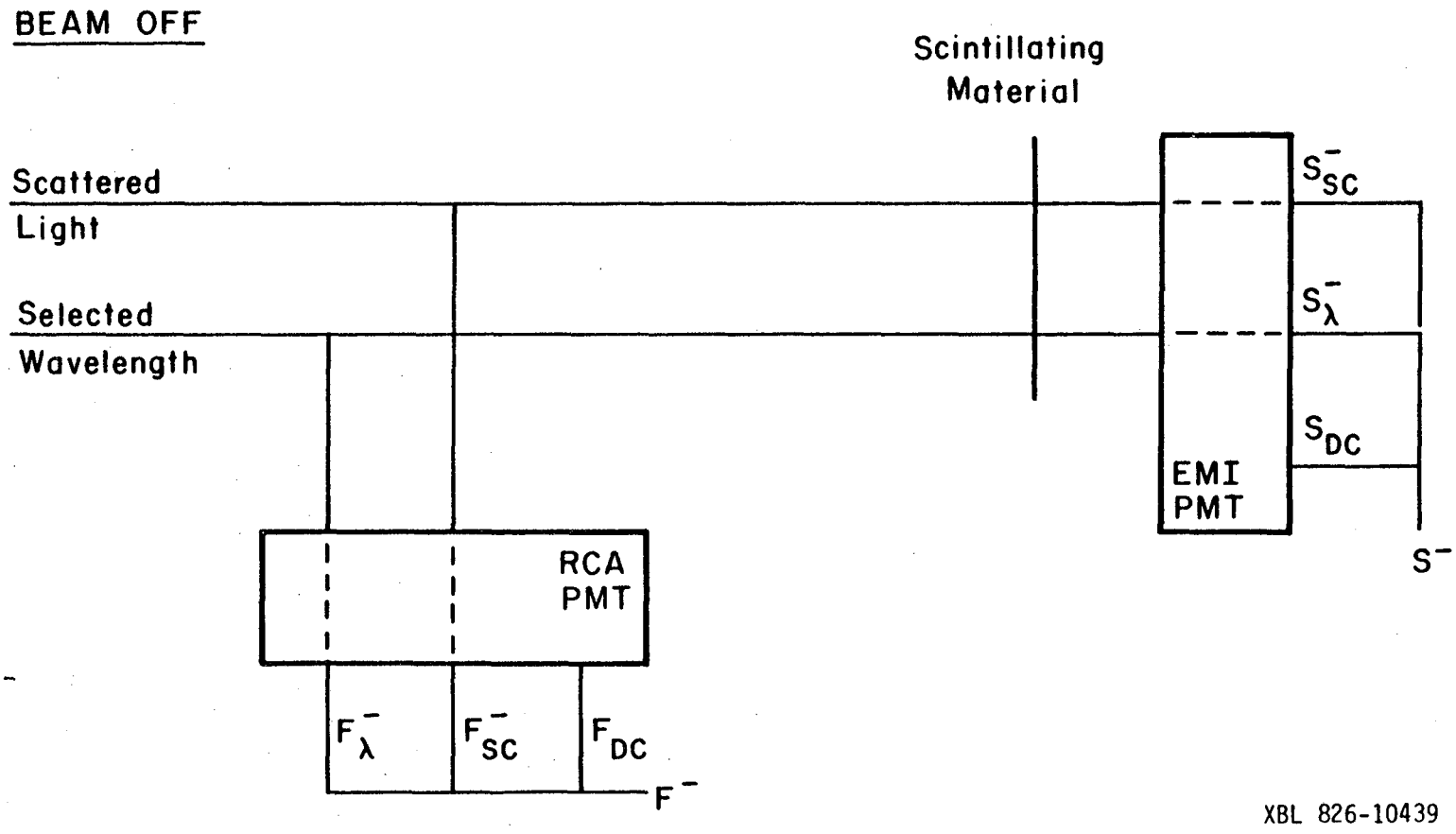
BEAM OFF
Scintillating
Material
Scattered
Light
Selected
Wavelength
S^-_{SC}
S^-_{λ}
S_{DC}
EMI
PMT
S^-
RCA
PMT
F^-_{λ}
F^-_{SC}
F_{DC}
F^-
XBL 826-10439

Figure III-3

Figure III-4. Composite quantum fluorescence yield spectrum of $Fe(CO)_5$. The solid line is the hydrogen lamp excited data with appropriate error bars at high energy end. The points are data corresponding to excitation by lines from Ar, Ne, and He. The statistical error in these data, as well as that for hydrogen excited data from 10.3 to 12.5 eV, is <3%.

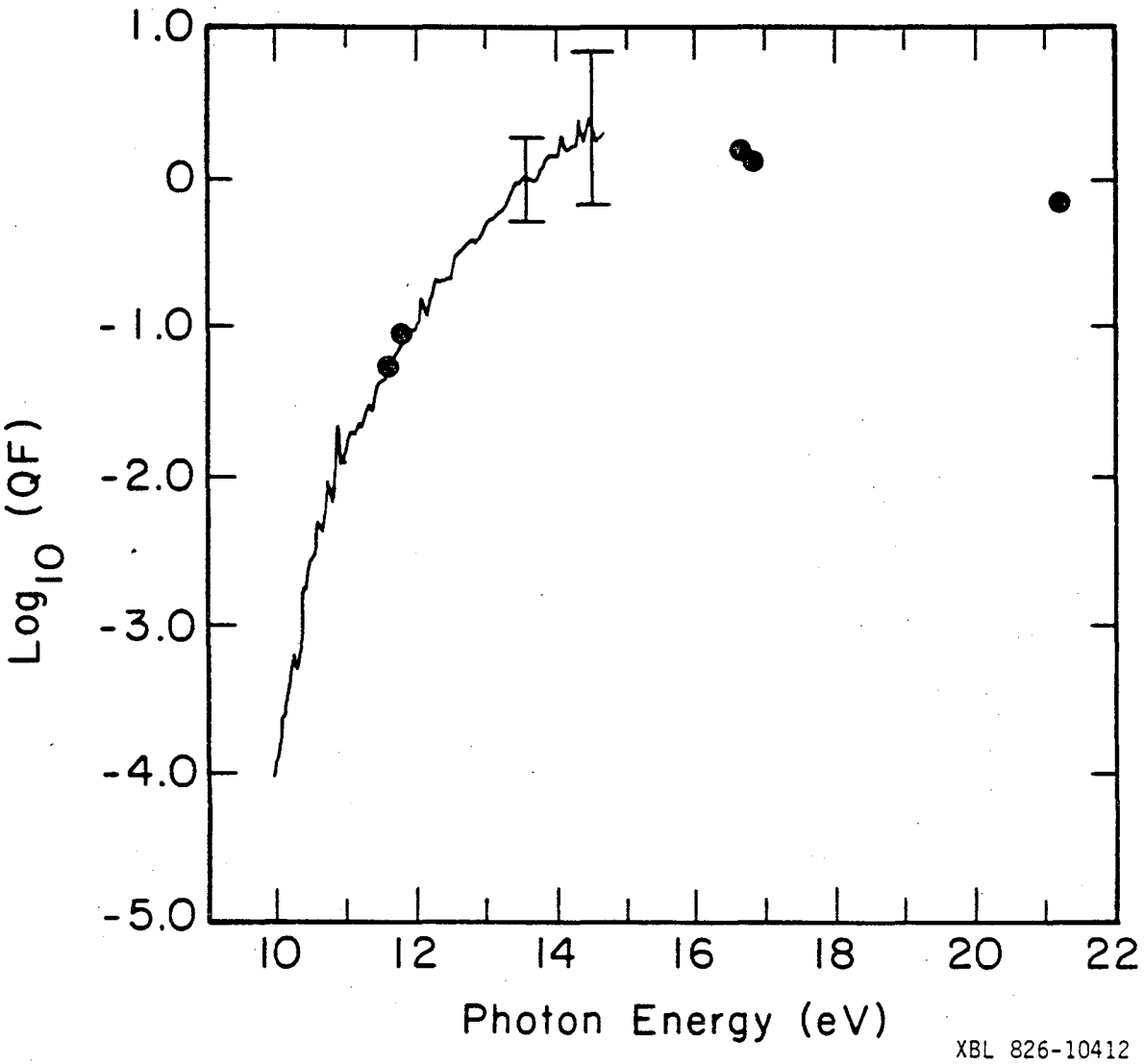
1.0
0
-1.0
-2.0
-3.0
-4.0
-5.0
Log10 (QF)
10
12
14
16
18
20
22
Photon Energy (eV)
XBL 826-10412

Figure III-4

Figure III-5. Band pass measurement of the 0.25 m JA monochromator in the configuration used for dispersed quantum fluorescence yield measurements.

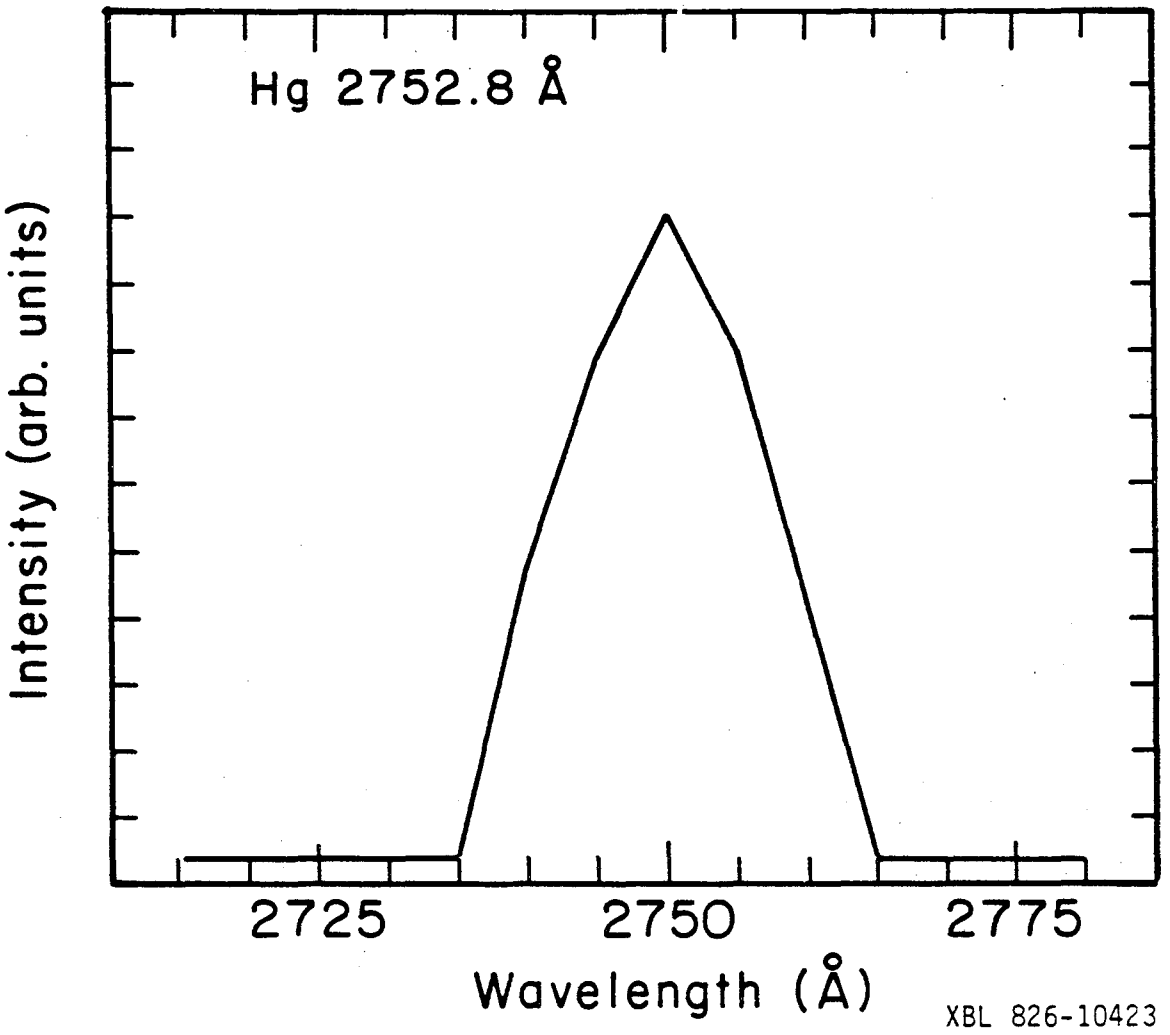
Hg 2752.8 Å
Intensity (arb. units)
2725
2750
2775
Wavelength (Å)
XBL 826-10423

Figure III-5

Figure III-6. Timing sequence used for dispersed quantum fluorescence data acquisition.

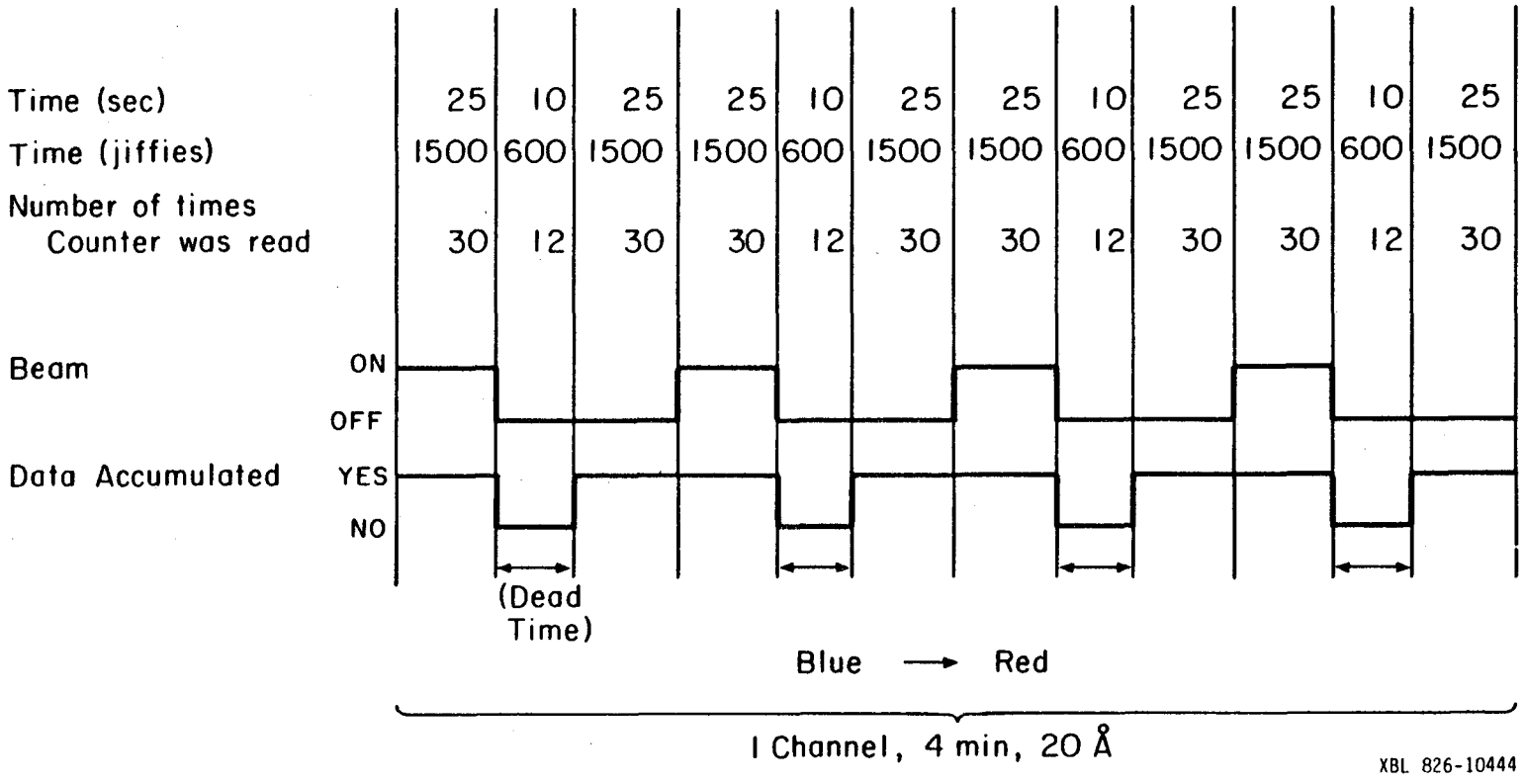
Time (sec)
Time (jiffies)
Number of times Counter was read
25 10 25 25 10 25 25 10 25 25 10 25
1500 600 1500 1500 600 1500 1500 600 1500 1500 600 1500
30 12 30 30 12 30 30 12 30 30 12 30
Beam
ON
OFF
Data Accumulated
YES
NO
(Dead Time)
Blue → Red
1 Channel, 4 min, 20 Å
XBL 826-10444

Figure III-6

Figure III-7a. Dispersed neon lamp induced iron fluorescence yield.

b. Dispersed neon metastable induced iron chemiluminescence yield.

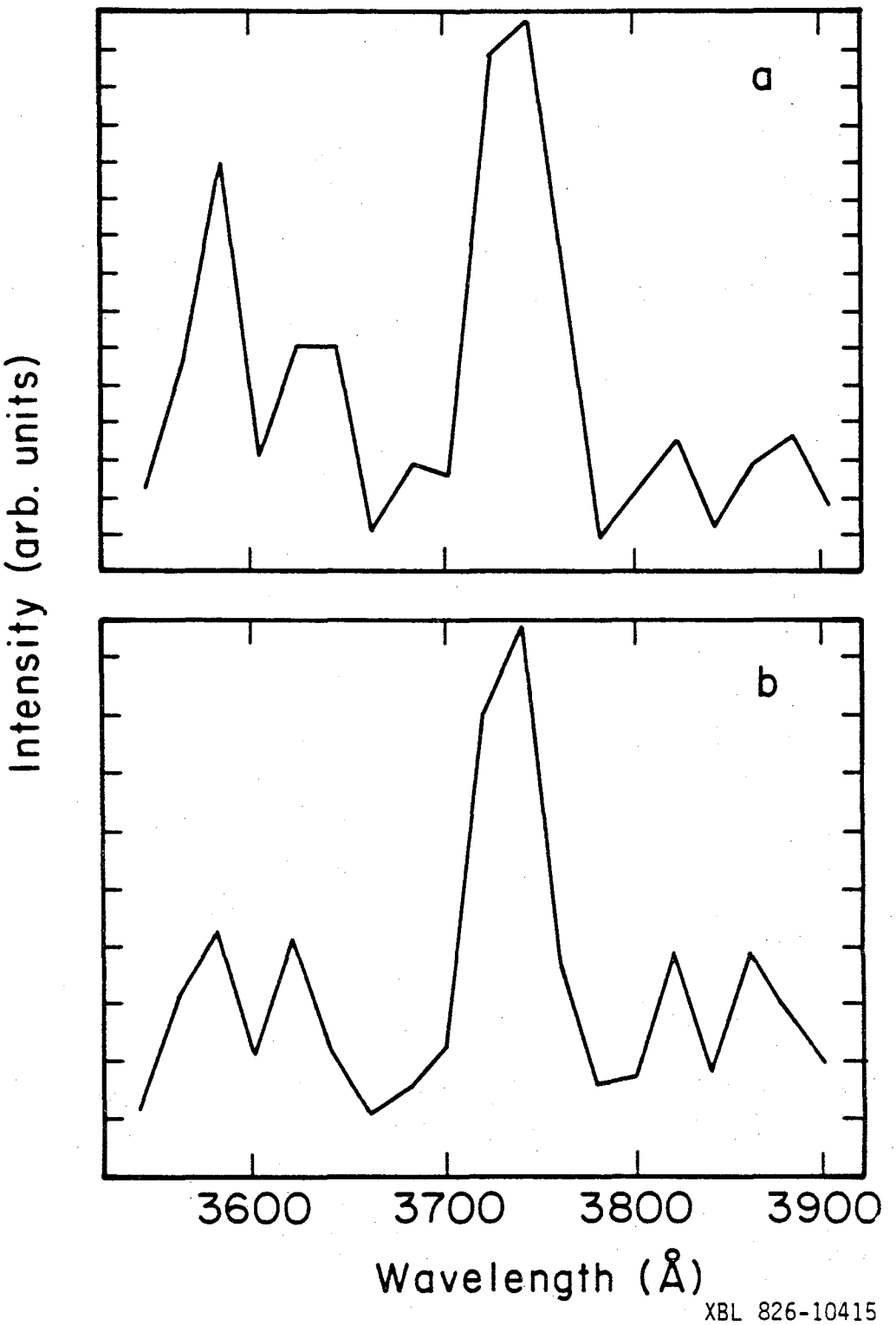
a
b
Intensity (arb. units)
3600
3700
3800
3900
Wavelength (Å)
XBL 826-10415

Figure III-7

Figure III-8a. Dispersed argon lamp induced iron fluorescence yield.

b. Dispersed argon metastable induced iron chemiluminescence yield.

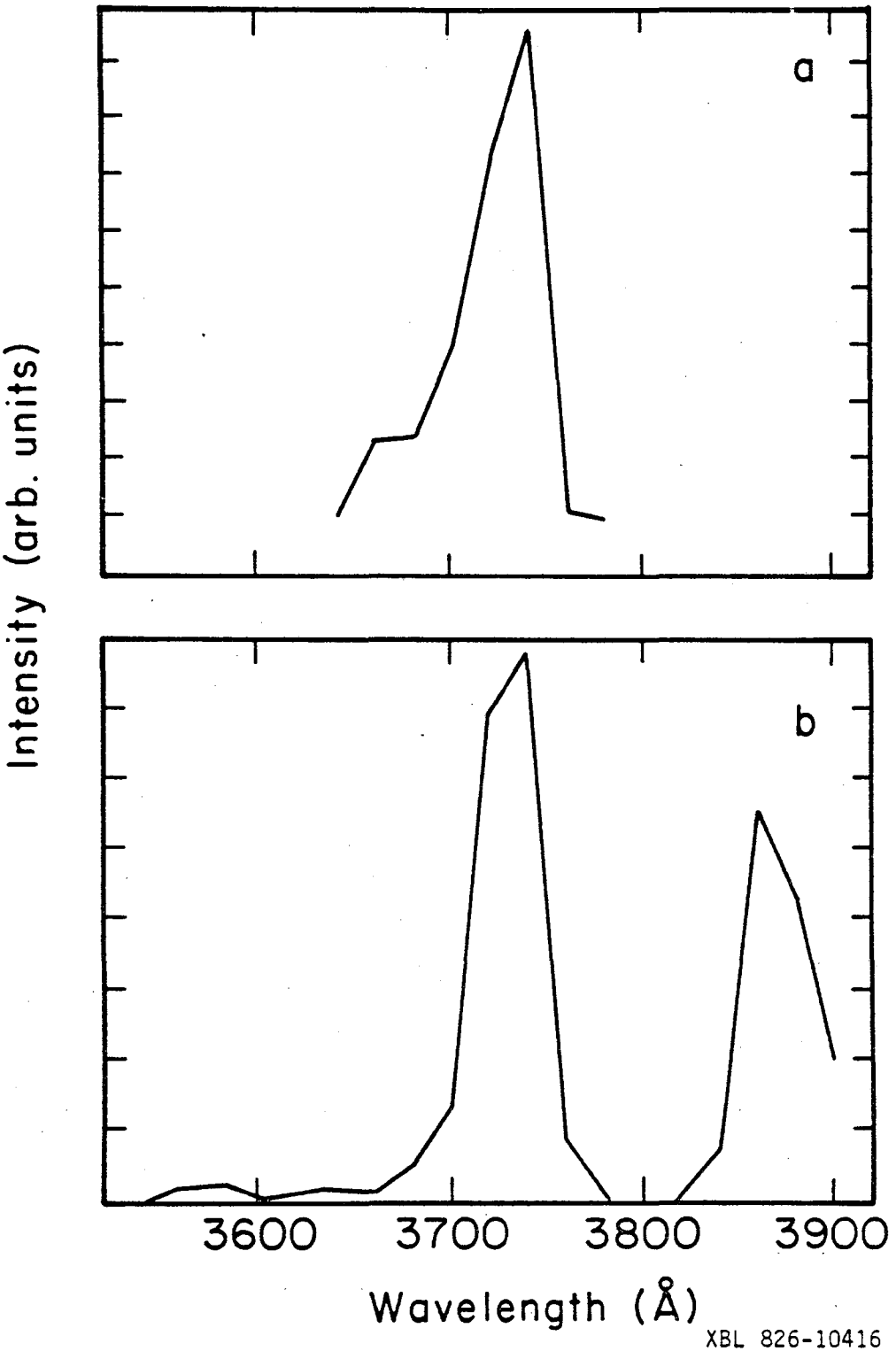
a
b
Intensity (arb. units)
3600
3700
3800
3900
Wavelength (Å)
XBL 826-10416

Figure III-8

Figure III-9. Timing sequence used for quantum photoionization data acquisition.

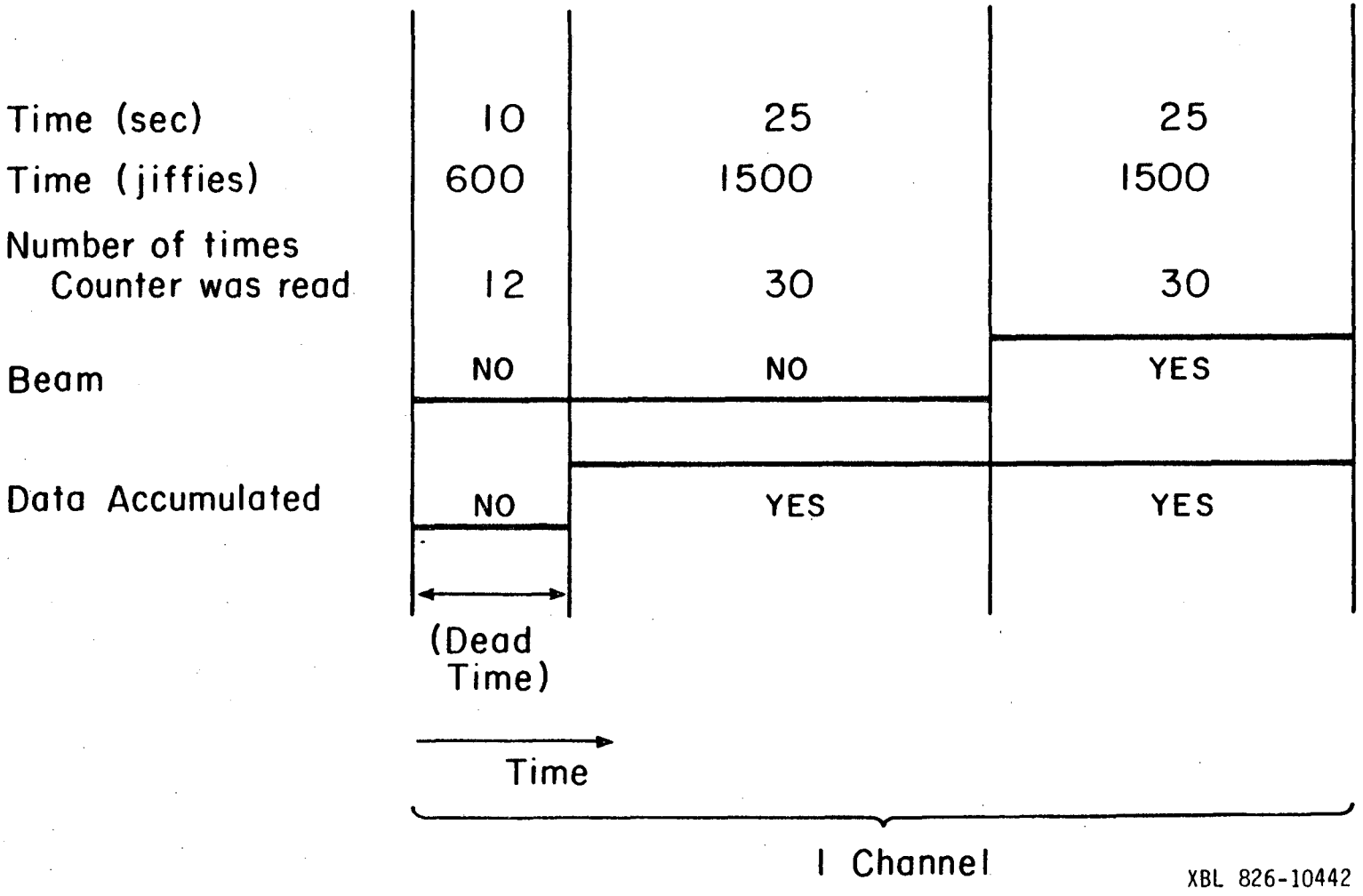
Time (sec)
Time (jiffies)
Number of times Counter was read
Beam
Data Accumulated
10
600
12
NO
NO
25
1500
30
NO
YES
25
1500
30
YES
YES
(Dead Time)
Time
1 Channel
XBL 826-10442

Figure III-9

Figure III-10. Quantum photoionization yield spectrum of $Fe(CO)_5$.

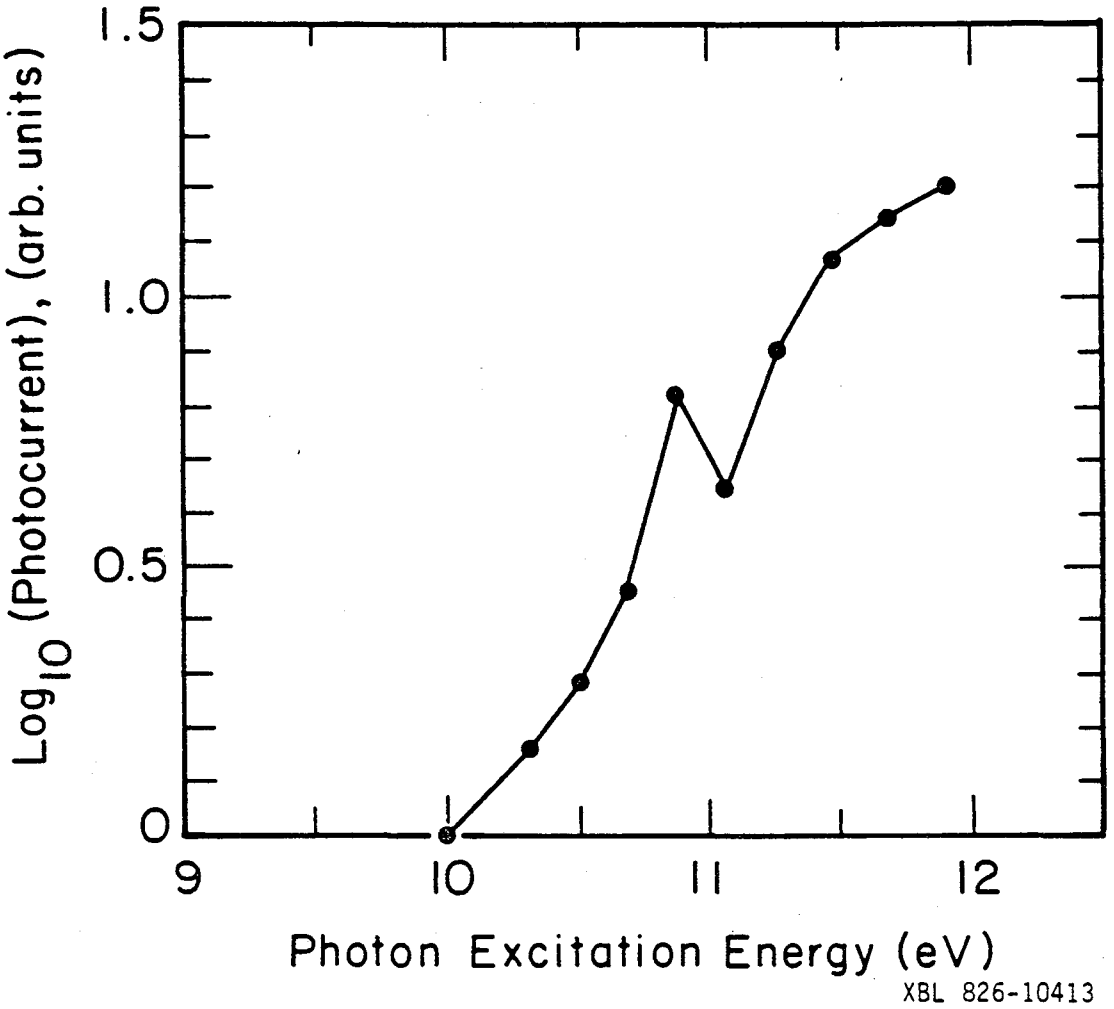

Figure III-10

Figure III-11. Beam density profile plotted as % absorption versus time (timing sequence in Fig. III-9 is used).

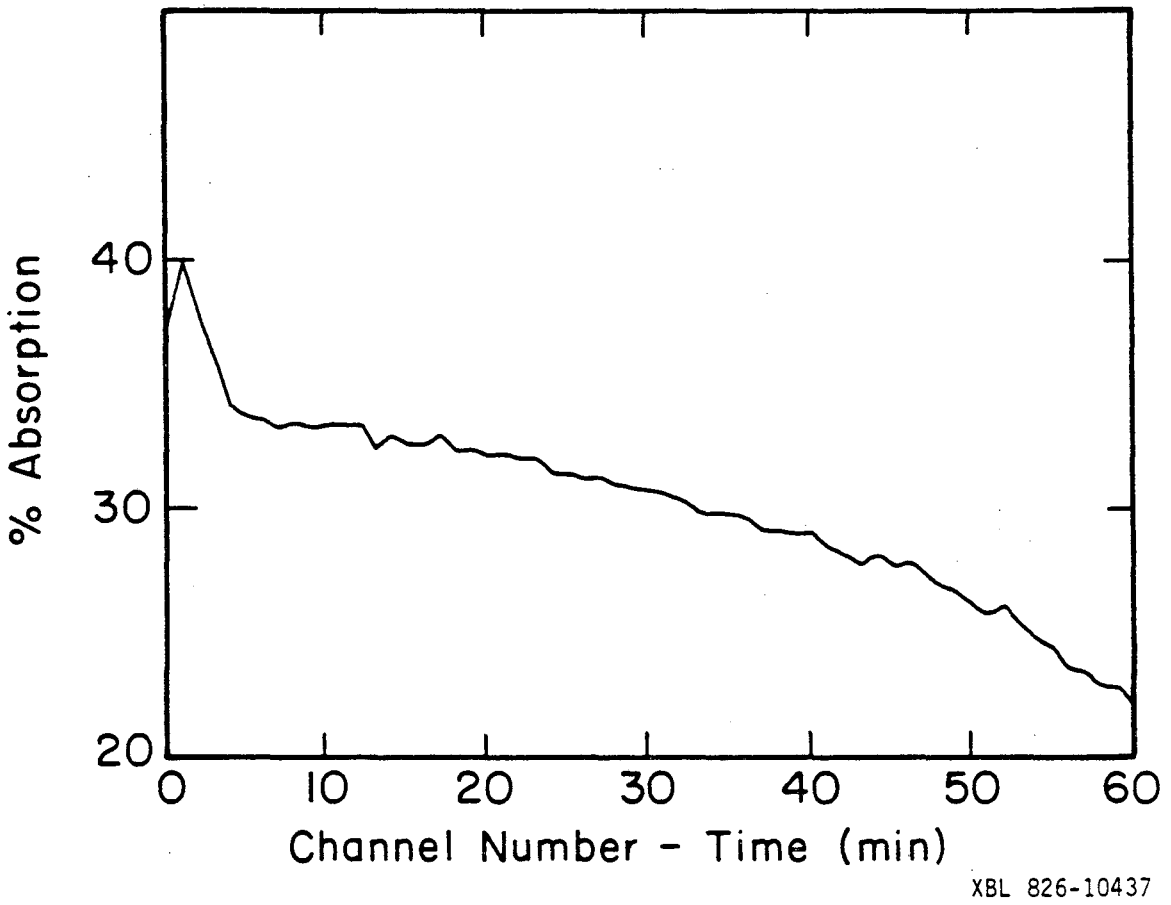

Figure III-11

CHAPTER IV

DISCUSSION AND THEORY

The first step in data analysis is to establish the order of the interaction between $Fe(CO)_5$ and VUV photons. The VUV photon flux in the interaction region was not directly measured. However, based on numerical calculations of the flux which are discussed in detail later, a flux of 5×10^{11} photons/sec/cm^2 in the most intense part of the hydrogen pseudocontinuum and a flux about a factor of 10 more for the rare gas resonance lines are good estimates. Due to these relatively low intensities, it is obvious that the primary $Fe(CO)_5$-photon interaction has to be first order in photons. In order to insure first order dependence on $Fe(CO)_5$ concentration, the $Fe(CO)_5$ beam was operated such that the molecules entering the VUV interaction region were in the collisionless part of the beam, allowing the study of iron fluorescence under collisionless conditions. This was not the case in the experiments done with rare gas metastables in this lab,[1,2,3] although metastable-$Fe(CO)_5$ beam experiments have been reported from other groups.[4,5] Collisional relaxation played a part in the observed intensities of some long-lived iron states in the rare gas metastable excitation studies. The lifetime limit for detecting long-lived states in this experiment was imposed by the time required for iron atoms to move through the detection volume. An estimate of the maximum pathlength which these atoms can travel during detection is 5 cm. The most probable Maxwell-Boltzmann velocity is determined by[6]

$$V_{mp} = 12895 \ (T/M)^{1/2} \qquad \text{(IV-1)}$$

where T is the temperature in K, M is the molecular weight of the particle, and V_{mp} is in cm/sec. The mass used for the particle was 196, the mass of $Fe(CO)_5$, and not 56, the mass of iron, because the limited degrees of freedom statistical dissociation model was anticipated. This theory leaves the excited metal atom with the center of mass velocity of the dissociating system. (The model is discussed in detail later.) At room temperature, $V_{mp} = 1.6 \times 10^4$ cm/sec, corresponding to a capability for detecting states with lifetimes on the order of 3.1×10^{-4} sec or shorter. The spectral analysis of Hellner, et al.,[7] showed that only the quintet manifold of iron, for which all transition lifetimes in the near UV are well within the detection limit, is active.

The beam density in the interaction region was determined by comparing an experimental absorption measurement with the known extinction value for $Fe(CO)_5$ and an empirical model for the beam density profile. The experimental absorption value, I/I_o, was measured to be 0.925 at 2536.5 Å. Turning to the Beer-Lambert law:

$$\ell n(I/I_o) = -\varepsilon l d_{exp} \qquad \text{(IV-2)}$$

and substituting the known value of 5.2×10^{-3} cm^{-1} Pa^{-1}[8] for ε at 2536.5 Å yields

$$l d_{exp} = 15 \text{ cm Pa.} \qquad \text{(IV-3)}$$

If this total optical density over the profile had been compressed into one mm (a useful concept for calculations following), then

$$d_{exp} = 150 \text{ Pa.} \qquad \text{(IV-4)}$$

To determine the density on the beam axis, d_o, the beam profile has to be computed. The density varies along an axis orthogonal to the beam axis according to:[9]

$$\frac{\rho(r,x)}{\rho(0,x)} = \cos^2\theta\cos^2\left(\frac{\pi\theta}{2\phi}\right) \qquad \text{(IV-5)}$$

The geometrical variables are graphically shown in Figure IV-1. The parameter ϕ is a function of the specific heat ratio, γ. For $\gamma = 1.2857$, $\phi = 1.888$.[9] The beam profile is shown in Figure IV-2 as a function of both the distance on the beam axis and the distance orthogonal to this axis. The ratio of the on beam axis density to the apparent optical density as measured by the absorption experiment through the center of the interaction region is determined as

$$\frac{\rho(0,x)}{\int_o^z \rho(r,x)\ dr}\ , \qquad \text{(IV-6)}$$

where z is the distance between the beam axis and the edge of the interaction chamber along the absorption measurement's optical axis; $z \approx 100$ mm. The integral can be reduced to a summation for evaluation by numerical techniques, so that

$$d_\Sigma = \int_o^z \rho(r,x)\ dr = \sum_{r=0,1,2\ldots}^{z} \rho(r,x). \qquad \text{(IV-7)}$$

Here $z \approx 110$, and r is stepped in 1 mm intervals. The ratio is

$$\frac{d_o}{d_\Sigma} = 0.0415. \qquad \text{(IV-8)}$$

Combining this value with the result of (IV-4) yields the beam density to be

$$d_o = 6.3 \text{ Pa} = 0.047 \text{ torr} \qquad \text{(IV-9)}$$

at the center of the interaction region, 31.5 mm from the nozzle. This number is only a guide since the density profile changes with the amount of reserve $Fe(CO)_5$ liquid in the bulb, as described in Chapter III.

Since extinction coefficients are temperature sensitive, the beam temperature must be determined. Since there were little data available on the type of beam source used in this experiment, the unlikely possibility that $Fe(CO)_5$ cooled upon expansion from the nozzle was investigated. This was accomplished by obtaining an absorption curve for the $Fe(CO)_5$ beam from 2200 to 3500 Å. It was found to be qualitatively the same as presented in the literature[8] for $Fe(CO)_5$ at room temperature.

The absolute absorption spectrum of $Fe(CO)_5$ in the VUV region was determined during beam density analysis by comparing absorption at 1170 Å to that at 2536.5 Å. The extinction coefficient at 1170 Å for $Fe(CO)_5$ was determined to be 0.0034 cm^{-1} Pa^{-1}. The total spectrum was obtained by correcting the percent absorption during quantum fluorescence measurements for beam density changes, and is shown in Figure IV-3.

Having established that the energy transfer from the VUV photon to the $Fe(CO)_5$ molecule occurs via a direct mechanism which is similar to that observed when metastables carry the energy, one must try to determine if the statistical decomposition model, which was applied successfully to those experiments, can be applied here. The model will now be briefly discussed; for more detail, see Hartman.[1]

The energy balance which governs the dissociation process of $Fe(CO)_5$ is:

$$E_u = E_{vuv} - E_d - E_m \qquad \text{(IV-10)}$$

where E_{vuv} is the energy of the photon. E_d is the energy required to rupture all five metal-carbonyl bonds ($E_d \sim 6$ eV). E_m is the energy required for excitation of the metal atom to any one of the electronic states from which fluorescence is observed. Subtracting the latter two from the first yields E_u, the energy which has to be deposited into the various electronic, vibrational, rotational, and translational modes of the carbonyl fragments to preserve the energy balance. It is postulated that the rate of formation of a particular metal atom in state M^* of energy E_m is given by the proportionality

$$\text{Rate of Formation of } M^* \propto \rho(E_u), \tag{IV-11}$$

where $\rho(E_u)$ is the density of states for all appropriate degrees of freedom active in the decomposition. The quantity $\rho(E_u)$ is calculated by taking the inverse Laplace transform of the partition function, q_{total}, of all the active degrees of freedom:

$$\rho(E_u) = L^{-1}\{q_{total}\} \tag{IV-12}$$

Two models with different active degrees of freedom will be discussed and compared. The most obvious model allows all degrees of freedom to be available for deposition of the available energy, E_u. The degrees of freedom and their partition functions resulting from breaking of all metal-carbonyl bonds in $Fe(CO)_5$ are:

i) Three degrees of translational freedom for the metal atom,

$$q_t = \frac{(2\pi mkT)^{3/2} V}{h^2}$$

$$= k_1 (kT)^{3/2} = k_1 s^{-3/2} \tag{IV-13}$$

ii) Three degrees of translational freedom for each CO,

$$q_t = k_2\, s^{-3/2} \qquad \text{(IV-14)}$$

iii) Vibration of each CO as a harmonic oscillator (anharmonicity enters into the model later).

$$q_v = \frac{kT}{h\nu_o} = k_3\, s^{-1} \qquad \text{(IV-15)}$$

iv) Rotation of each CO in three dimensions,

$$q_r = \frac{8\pi IkT}{h^2} = k_4\, s^{-1} \qquad \text{(IV-16)}$$

v) Lack of CO electronic excitation or dissociation.

Choice (v) is assumed due to the lack of experimental evidence to the contrary. Since all degrees of freedom are treated as independent, the total partition function for $Fe(CO)_5$ is the product of these terms:

$$q_{total} = (k_1\, s^{-3/2})(k_2\, s^{-3/2})^5(k_3\, s^{-1})^5(k_4\, s^{-1})^5$$

$$= k_5\, s^{-19} \qquad \text{(IV-17)}$$

$$\rho(E) = L^{-1}\{q_{total}\}$$

$$= k_6\, E^{18}. \qquad \text{(IV-18)}$$

By substitution of an anharmonic oscillator into the vibrational partition function,

$$\rho(E) \propto e^{mE}(E^{18} - 0.7369\, mE^{19} + 0.2763\, m^2E^{20}) \qquad \text{(IV-19)}$$

where m is a constant in the vibrational partition function,

$$q_v = \frac{b}{s-m} \qquad \text{(IV-20)}$$

computed by a least squares fit to experimental data as described in Appendix II. This model, however, was found by Hartman to contain far too many active degrees of freedom.

The second model appears to represent the dynamics of the decomposition in Hartman's work well. It assumes that dissociation occurs either simultaneously or sequentially, but so rapidly that no rearrangement is possible. Based on this assumption,

i) CO's can be treated as one dimensional translators, i.e., they move radially away from the metal,

ii) the CO fragments carry away no rotational energy as no torque is applied during break up,

iii) the metal is expected to remain stationary in the center of mass system of $Fe(CO)_5$ and has no translational degrees of freedom associated with it,

iv) as in the previous model, the CO's are treated as anharmonic oscillators and

v) no electronic excitation is allowed in the CO's.

With these assumptions, the only active partition functions are:

i) each CO is a one dimensional translator, and

$$q_t = k_1^{\,1}\, s^{-1/2} \qquad \text{(IV-21)}$$

ii) each CO is an anharmonic oscillator

$$q_v = \frac{b}{s-m} \qquad \text{(IV-22)}$$

such that

$$\rho(E_u) \propto e^{mE}(E^{6.5} - 0.3333\ mE^{7.5} + 0.06863\ m^2\ E^{8.5}). \qquad \text{(IV-23)}$$

The application of this model to the VUV work will be discussed.

The first evidence that the limited degrees of freedom model is applicable to VUV photon induced iron fluorescence is the analysis of data by Hallner, et al.,[7] in which VUV induced fluorescence of $Fe(CO)_5$ was first observed. In this simple experiment, a rare gas discharge tube was mated via a LiF window to a cell containing $Fe(CO)_5$. Excitation energies in this experiment were limited to Xe, Kr, and Ar VUV resonance lines. However, the major problem in analyzing these data was that the iron emission line intensities cited are suspect for two reasons. First, the VUV light reaching $Fe(CO)_5$ was not monitored and certainly changed during the experiment due to F center formation in the LiF window.[7] Secondly, the deposition of iron formed a film on all surfaces causing a change not only in the VUV photon flux, but also in the UV photon collection efficiency.

However, if their data are converted to rates of depletion of upper iron states by the equation:

$$\text{rate of depletion} \propto \frac{I(\ell,u)}{A(\ell,u)/\sum_x A(x,u)} \qquad \text{(IV-24)}$$

where $I(\ell,u)$ is the observed intensity of the emission line, $A(\ell,u)$ is the Einstein A coefficient[10] for that emission line and $\sum_x A(x,u)$ is the sum of Einstein A coefficients of all radiative modes of decay of the iron state, u, the data show good agreement with our limited degrees of freedom dissociation model. These data are plotted in Figure IV-4, and exhibit somewhat more spread than the metastable data acquired by Hartman, as was expected. Interestingly, only the quintet iron manifold is active in the VUV induced fluorescence. This is in contrast to

metastable excitation, for which all spin manifolds (singlet, triplet, quintet, and septet) are active.

The first way of applying the limited degrees of freedom model to the VUV work reported here is through direct comparison of dispersed fluorescence recorded from VUV excitation and the dispersed chemiluminescence recorded from metastable excitation. This is done easily even under low resolution because the comparison is done only in the region 3500 - 3900 Å, where the contribution to both data sets stems only from the quintet manifold. For quantitative comparison, both data sets must be gathered under identical conditions. The results were shown in Figures II-7 and II-8 for neon and argon, respectively. The small difference between the energy of the VUV photons and the metastables, shown in Table IV-1, can be ignored. Overall, the data sets agree very well within statistical error.

Simulations of the spectra using the limited degrees of freedom dissociation model were also made. The intensity of each emission line was computed with the formula

$$I(\ell,u) = \rho(E_u) \times \left(\frac{A(\ell,u)}{\sum_x A(x,u)}\right) \qquad \text{(IV-25)}$$

which is an analogue of Equation (IV-24). The density of states was computed by Equation (IV-23), using all emission lines from all energetically accessible quintet iron states. The value of E_d used was 6.10 eV. The choice of a value slightly greater than the thermochemical value of 5.98 eV will be discussed later. The resultant simulated spectra are shown in Figures IV-5 and IV-6 for 11.6 and 16.6 eV photons, respectively. These are the approximate energies of argon and neon VUV photons (or metastables), respectively. In order to compare the simulations with the experimental results, the resolution of the monochromator

was convoluted into the calculation. The monochromator line width used was the experimentally measured slit function shown in Figure III-5. This slit function was convoluted with each emission line and the resultant spectrum was divided into 20 Å sections to parallel the 20 Å/channel width of the experiment. The results, shown in Figure IV-7 for argon and Figure IV-8 for neon, show that the same major features appear in both data sets, giving further support to the validity of the limited degrees of freedom dissociation model. (The comparison to Figures III-7 and III-8 is only qualitative, since the experimental data were not corrected for monochromator-PMT response.)

In the limited degrees of freedom dissociation model, there is an adjustable parameter, E_d, the $Fe(CO)_5$ dissociation energy. The experimental results discussed up to this point have not been accurate enough to allow fine tuning of this parameter. However, this is not the case with the undispersed fluorescence and photoionization quantum yield data.

The value of E_d has been a source of minor controversy for many years. Cotton, et al.,[11] measured E_d for $Fe(CO)_5$ by thermochemical means and reported a value of 138.3 ± 1.7 kcal/mole (5.977 ± 0.074 eV). This is in contrast to the value of 1.25 ± 0.03 eV per bond obtained by Distefano[12] in a photoionization study. The discrepancy has been blamed on a failure to account for the kinetic energy possessed by the fragments of photoionization. This problem is circumvented in our work because the limited degrees of freedom dissociation model takes all the energies into consideration.

In our analysis, it is assumed that neutral iron formation is the predominant product channel, an assumption which will be justified later. First one must establish the true fluorescence quantum yield by extrapolating the statistically accurate experimental measurement into the region

where the errors in the experimental data become large, using the theory as a guide. If one assumes that neutral production is the only product channel, all absorbed photons will produce either excited or ground state iron atoms with unit efficiency. To find the ratio of the number of total neutral iron atoms, N, to the number of photons emitted, F, the following formula was used:

$$\frac{N}{F} = \frac{\Sigma\rho(E_u)}{\Sigma\rho(E_u)\times(\Sigma PMTQE(\lambda)\times(\frac{A(\ell,u)}{\sum_x A(x,u)}))} \quad . \qquad \text{(IV-26)}$$

The first summation in the denominator and the summation in the numerator are over all energetically accessible neutral iron quintet levels.[13] The second summation in the denominator corrects the intensity of any emitted radiation for the manufacturer's quoted quantum efficiency for the photomultiplier (shown in Fig. IV-1). The results of this computation are shown for various E_d values in Figure IV-10. It can be seen that the model is most sensitive to the value of E_d at low photon energies. The calculations terminate at 14 eV because higher energies can deposit energy in excess of iron's first ionization potential. Fortunately, the statistical error in the experimental data is least where the model is the most sensitive to the value of E_d.

Since a unit production efficiency is assumed over the available energy range, multiplying the N/F ratio by the experimental quantum fluorescence yield curve (or adding their $\log_{10}$ values) should lead to a constant value at all relevant photon energies (10 to 12 eV). In order to achieve this constant value (a flat line in Fig. IV-11), the value of 6.10 ± 0.05 eV was chosen for E_d. To achieve the flat line above 12 eV, where the theory is less sensitive to the choice of E_d, an interpolated

quantum fluorescence yield curve was used, as shown in Figure IV-12. This interpolated curve fits the experimental data well in the region between 10 to 12.5 eV and at the two neon points, the region where the statistical error is <3%. It also fits the data in the region between 12.5 and 15 eV within the experimental error as is shown in Figure III-4.

We now compare in Figure IV-13, the interpolated quantum fluorescence yield curve, to the theoretical quantum fluorescence yield defined by

$$F = \Sigma\rho(E_u) \times (\Sigma PMTQE(\lambda)) \times \left(\frac{A(\ell,u)}{\sum_x A(x,u)}\right) \qquad \text{(IV-27)}$$

(which is simply the denominator in Equation (IV-26)). For simplicity, the data plotted are only for E_d = 6.10 eV. The quantum fluorescence yield predicted by the all degrees of freedom model is included for comparison (curve B). The curves are normalized arbitrarily at a photon energy of 10 eV. It is obvious that the model allowing all degrees of freedom to be active gives a much poorer fit, as it did with the metastable work. However, the limited degree of freedom model does not correspond to the composite experimental fluorescence quantum yield curve either. One's first instinct might be to believe that too many degrees of freedom are still allowed, but the evidence discussed earlier makes this untenable.

Our application of the theory thus far has depended on the hypothesis that the only way an excited $Fe(CO)_5$ can lose energy is through decomposition into a metal atom (which may be excited) and five free COs. However, an alternate competing non-radiative channel could explain the discrepancy, and ionization appears to be a good candidate. By looking at the list of appearance potentials of $Fe(CO)_5$ ion fragments as measured

by electron impact:[14]

$Fe(CO)_5^+$	8.53 eV
$Fe(CO)_4^+$	10.0 eV
$Fe(CO)_3^+$	10.3 eV
$Fe(CO)_2^+$	11.8 eV
$FeCO^+$	14.0 eV
Fe^+	16.1 eV

it is clear that the energies involved in this experiment are sufficient for ionization. The VUV photoionization experiment measured the total ion flux in order to see if ionization could make up the difference between our model and the interpolated quantum fluorescence yield data. There was no attempt to study the individual ion fragments. The data were shown in Figure III-10.

A comparison of the experimental photoionization yield data and the difference between the interpolated fluorescence quantum yield and the limited degrees of freedom theoretical fluorescence quantum yield as a parametric function of E_d is shown in Figure IV-14. Again the curve corresponding to E_d = 6.10 eV is the most consistent with the data.

Based on all the information presented thus far, the following dissociation scheme is postulated:

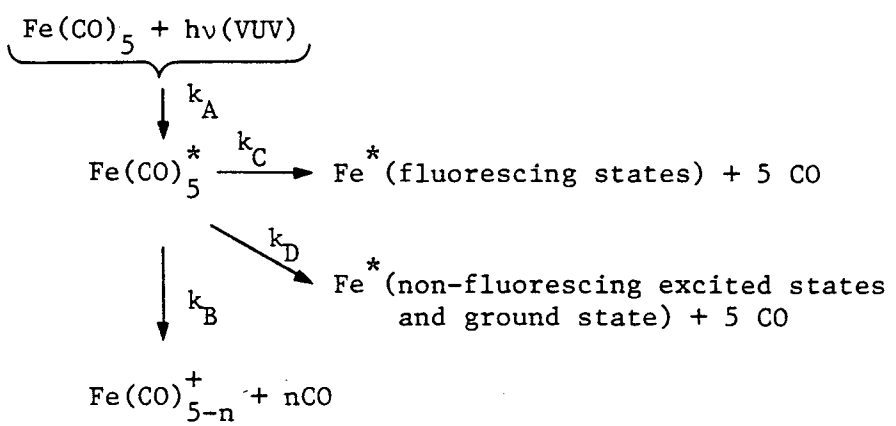

The rate constants, k_B, k_C, and k_D are of greatest interest here. k_A is related to the VUV absorption cross-section of $Fe(CO)_5$. Since our model completely accounts for both fluorescence and photoionization quantum yields, the fate of the $Fe(CO)_5^*$ intermediate excited state is also accounted for. This conclusion indicates that each singular $Fe(CO)_5^*$ intermediate state, i.e., an intermediate completely described by a particular set of quantum numbers, is adiabatically connected to a unique product state of Fe^* and COs. It should be pointed out that the density of states in $Fe(CO)_5^*$ is so high that a given absorbed energy can couple to any excited metal state consistent with this energy. In this manner the rate of formation of a particular $Fe(CO)_5^*$ is governed by the rate of formation of Fe^*, which is purely statistical.

Ionization seems to consist of a simple potential surface hopping from neutral to ionized surfaces. If the experimental photoionization yield curve falls exactly onto the predicted curve in Figure IV-14, which it does to within the experimental error, then the surface hopping would be insensitive to the state of the metal atom to which the neutral surface correlates. While we do not know the absolute branching ratio between ion and neutral production, we can calculate the absolute change in the relative branching ratio as a function of VUV photon energy, as

is shown in Figure IV-14. In order to make the branching ratios absolute, estimates of the VUV photon flux were needed. Using experimental fluorescence and photoionization quantum yields as well as absorption measurements, estimates of the VUV photon flux were obtained. The computation was carried out for 1170 Å (10.60 eV), the energy of the absorption cross-section measurement. Using the value of 5.2×10^{-3} cm^{-1} Pa^{-1} for the $Fe(CO)_5$ extinction coefficient at 2537 Å, and the value of 0.153 for the ratio of $(I-I_o)/I$ values at 2537 Å to that at 1170 Å yielded an extinction coefficient of 0.034 ± 0.005 cm^{-1} Pa^{-1} (1.3 ± 0.2 $Å^2$) at 1170 Å. The following data and efficiency factors had to be considered:

i) the detected UV photon flux was 440 counts/sec (at this wavelength);

ii) the geometrical collection efficiency of the detection system, based on a homogeneously dispersed point light source being detected by an active photocathode 5 x 15 mm in size located 250 mm from the light source, was 9.6×10^{-5};

iii) the number of neutrals produced per emitted UV photon was obtained from a theoretical computation using E_d = 6.10 eV and the limited degrees of freedom dissociation model, giving 24,400 VUV photons/detected UV photon; and

iv) the fraction of the VUV photons absorbed in the experiment was 0.38.

Combining these factors:

$$\frac{440 \dfrac{\text{detected UV photons}}{\text{sec}} \times 24{,}400 \dfrac{\text{photons absorbed}}{\text{detected UV photons}}}{9.6 \times 10^{-5} \times 0.38 \dfrac{\text{VUV photons absorbed}}{\text{VUV photons incident}}}$$

yields 3.0 x 10^{11} incident VUV photons/sec. This number has to be considered an absolute lowest estimate since the photomultiplier efficiency used was the manufacturer's optimum efficiency which will decrease with time by an unknown amount. Moreover, no estimates were included for losses associated with the two quartz windows in the optical detection path.

The number of VUV incident photons at 10.60 eV needed to produce the observed photoion current of 2.7 x 10^{-10} A at 42% absorption of VUV photons is 2.0 x 10^{10} VUV photons/sec. A unit photoion collection efficiency is assumed here due to the high collection potential. From 10.6 to 14 eV the theoretical branching ratio for ions to neutrals increases by a factor of 73 (assuming E_d = 6.10 and using the data shown in Fig. IV-14). This increase implies that a photon flux of 1.5 x 10^{11} VUV photons/sec would be sufficient to produce only ionization. This again is a lower limit considering the fact that fluorescence is still a very strong product channel. This leads to an estimate of the actual photon flux at 1170 Å, one of the most intense regions of the hydrogen pseudocontinuum, of 4-8 x 10^{11} photons/sec. This estimate is consistent with fluxes obtained by other groups using a similar lamp design when slit sizes are taken into account.

With the help of the VUV photon flux, estimates of the absolute branching ratios and cross-sections can now be made. They will be listed only at the photon energy of 10.60 eV (1170 Å), but using Figures IV-10, IV-12, and IV-14, estimates can be broadened to the region between 10 and 14 eV.

The branching ratio between fluorescence and neutral production rate constants, $k_C/(k_C + k_D)$ is calculated theoretically to be 1.33 x 10^{-4},

and the ratio between ionization and neutral production rate constants, $k_B/(k_C + k_D)$, is between 0.0048 and 0.0024. The latter number justifies our previous assumption that ionization is not a major product channel at this excitation energy.

The branching ratios above, in conjunction with the 1.3 ± 0.2 $\mathring{A}^2$ VUV absorption cross-section, lead to cross-sections of 1.3 ± 0.2 $\mathring{A}^2$ for neutral production, between 0.006 and 0.003 $\mathring{A}^2$ for the ionization process, and 1.7 ± 0.3 x 10^{-4} $\mathring{A}^2$ for fluorescence. The small cross-section for fluorescence is due to preferred production of ground and low lying iron levels which produce no observable emission in the UV and visible parts of the spectrum.

The following conclusions can be drawn:

1) The application of the limited degrees of freedom statistical dissociation model can be expanded to include VUV photon induced iron pentacarbonyl dissociation as well as metastable atom collisional electronic energy transfer, but the iron excited states are limited here to the quintet manifold in contrast to the lack of spin differentiation seen with metastables.

2) The dissociation model is expanded to include photoionization as is shown below:

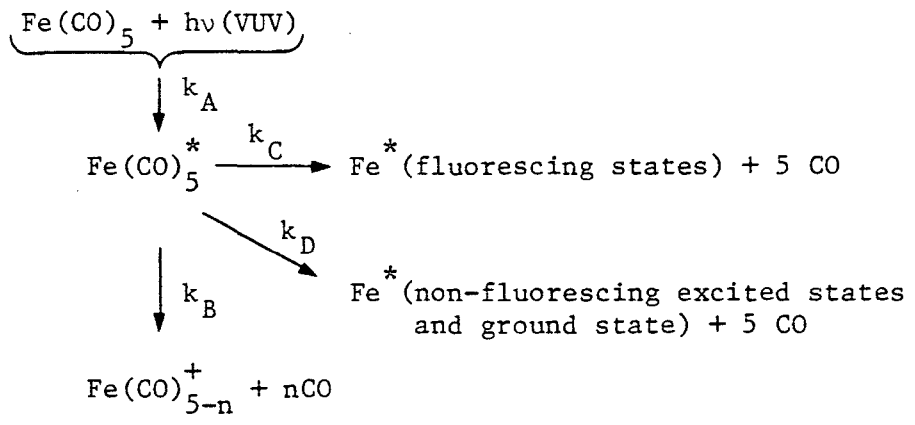

3) The branching ratio between fluorescence and neutral production rate constants, $k_C/(k_C + k_D)$, is calculated theoretically to be 1.33×10^{-4} at 1170 Å (10.60 eV) photon wavelength, and the ratio between ionization and neutral production rate constants, $k_B/(k_C + k_D)$, is between 0.0048 and 0.0024 at this wavelength.

4) The absorption cross-section at 1170 Å for $Fe(CO)_5$ is 1.3 ± 0.2 Å^2. The cross-sections for the remaining processes at 1170 Å are 1.3 ± 0.2 Å^2 for neutral production, between 0.006 and 0.003 Å^2 for the ionization process, and $1.7 \pm 0.3 \times 10^{-4}$ Å^2 for fluorescence.

5) The limited degrees of freedom statistical dissociation model was verified quantitatively over the range of excitation energies from 10 to 14 eV.

6) Through the application of the model to experimental data, the total metal-ligand bond dissociation energy of $Fe(CO)_5$ was determined to be 6.10 ± 0.05 eV.

The ideal experiment for the future with regard to iron fluorescence from VUV photolysis would be to look under high resolution at a single iron line and to observe its intensity as a function of VUV photon energy. A series of such experiments would serve to verify the statistical model with respect to a series of excited state thresholds, some of which could be chosen to lie in an energy region which is in competition with photoionization. However, this experiment is unlikely to be successful without a VUV light source several orders of magnitude more intense than ours.

One of the most intriguing unanswered questions associated with $Fe(CO)_5$ decomposition is the spin manifold selectivity of the photolysis compared to the lack of selectivity in the metastable excitation. Some insight into this difference could be gained from an electron impact

activated $Fe(CO)_5$ decomposition experiment. Such an experiment is under way in our laboratory.

Two examples of applications of metal carbonyl decomposition to other research areas are translational cooling and novel gas phase molecule production.

The former process stems from the fact that the studies given in this thesis show that the metal atom remains at the center of mass of the dissociating system. This implies that it retains the translational velocity of the parent molecule, which was much heavier than the atom itself. The heavier and more numerous the ligands, the cooler the liberated atoms' translational motion will be.

The latter application would be exemplified by dissociating molecules such as ferrocene for which there becomes a reasonably high concentration of C_5H_5 in the gas phase as well as free (and highly reactive) metal atoms.

REFERENCES for CHAPTER IV

1. D. C. Hartman, Ph.D. Thesis, University of California, Berkeley, LBL Report 11208 (1980).

2. D. C. Hartman, W. E. Hollingsworth, and J. S. Winn, J. Chem. Phys. 72, 833 (1980).

3. D. C. Hartman and J. S. Winn, J. Chem. Phys. 68, 2990 (1978).

4. H. L. Snyder, T. P. Parr, D. H. Parr, B. T. Smith, and R. M. Martin, Chem. Phys. Lett. 73, 487 (1980).

5. J. Kobovitch and J. Krenos, J. Chem. Phys. 74, 2662 (1981).

6. Norman Davidson, Statistical Mechanics (McGraw-Hill Book Company, Inc., 1962) p. 158.

7. L. Hellner, J. Masanet, and C. Vermeil, Nouveau Journal de Chimie, 3, 721 (1979).

8. G. Nathanson, B. Gitlin, A. M. Rosan, and J. T. Yardley, J. Chem. Phys. 74, 361 (1981).

9. J. H. DeLeeuw, Rarefied Gas Dynamics, Vol. II (Academic Press, N.Y., 1966).

10. C. H. Corliss and J. L. Tech, Nat. Bur. Stand. (U.S.) Monogr. 108 (1968).

11. F. A. Cotton, A. K. Fischer, and G. Wilkinson, J. Am. Chem. Soc. 81, 800 (1959).

12. G. Distefano, J. Res. Nat. Bur. Stand. (U.S.) 74A, 233 (1970).

13. C. E. Moore, Nat. Stand. Ref. Data Ser., Nat. Bur. Stand., 35 (1971).

14. R. E. Winters and R. W. Kiser, Inorg. Chem. 3, 699 (1964).

Table IV-1

Energies and Radiative Transition Probabilities of the Lowest Excited States of He, Ne, and Ar

Atom	Level	Energy (eV)[d]	Radiative Transition Probability (sec^{-1})
He	$(1s2p)^1P^o$	21.217	1.8×10^{9}[a]
	2^1S	20.615	45[c]
	2^3S	19.819	4×10^{-5}[c]
Ne	$^1P_1$	16.848	6.64×10^{8}[a]
	$^3P_0$	16.716	metastable
	$^3P_1$	16.671	0.476×10^{8}[a]
	$^3P_2$	16.619	0.5[c]
Ar	$^1P_1$	11.828	5.1×10^{8}[b]
	$^3P_0$	11.723	metastable
	$^3P_1$	11.624	1.19×10^{8}[b]
	$^3P_2$	11.548	0.12[c]

[a] W. L. Wiese, M. W. Smith, and B. M. Glennon, Natl. Stand. Ref. Data Ser. Natl. Bur. Stand. 4 (1966).

[b] W. L. Wiese, M. W. Smith, and B. M. Miles, Natl. Stand. Ref. Data Ser. Natl. Bur. Stand. 22 (1969).

[c] D. H. Stedman and D. W. Setser, Chemical Application of Metastable Rare Gas Atoms (Pergamon Press Ltd. (1971)).

[d] C. E. Moore, Natl. Stand. Ref. Data Ser. Natl. Bur. Stand. 35 (1971).

"for number sequence only"

Figure IV-1. A diagram of the geometries involved in a semieffusive nozzle beam labelled with variables used in the text.

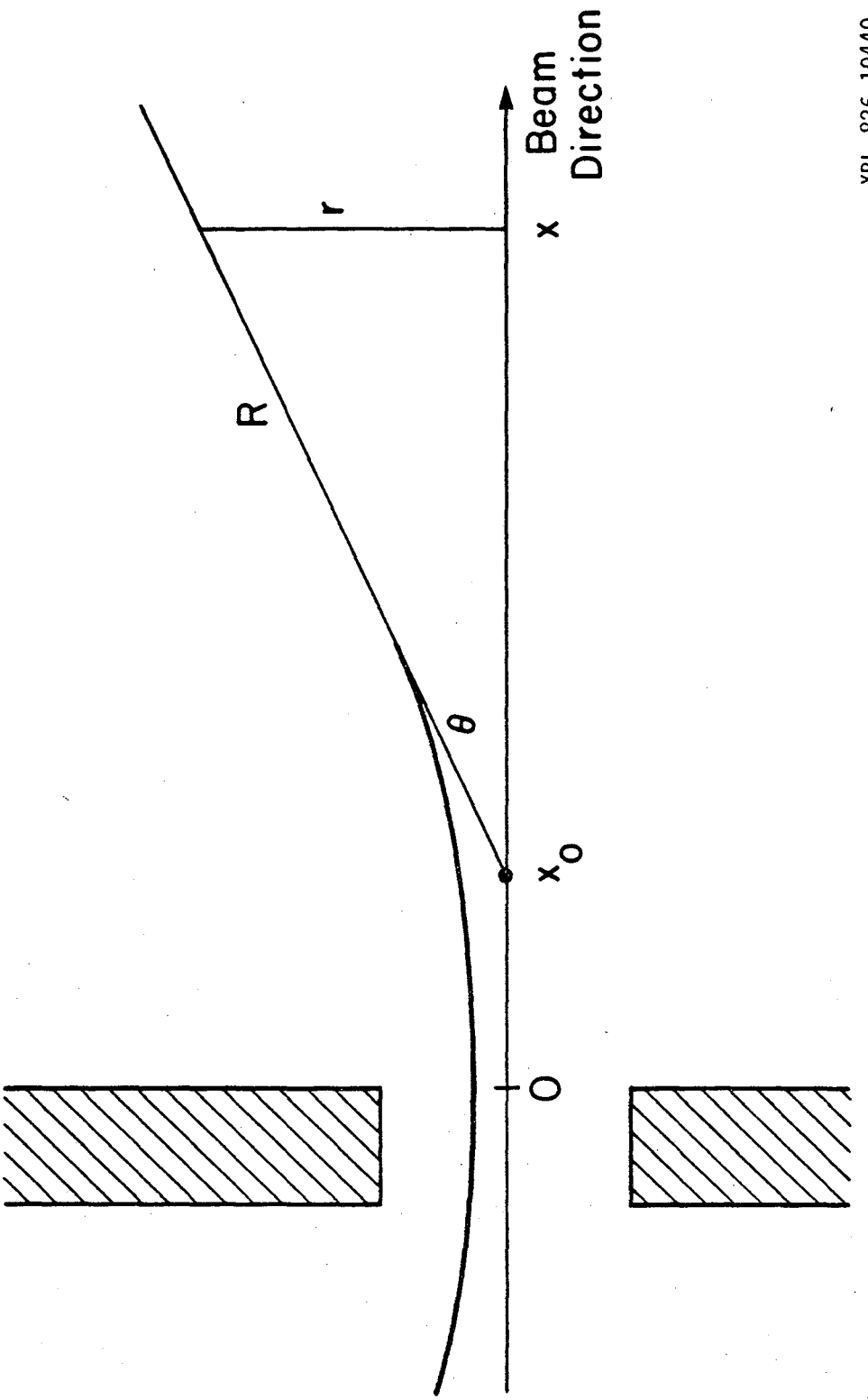

XBL 826-10440

Figure IV-1

Figure IV-2. A theoretical beam density profile plotted as a function of the orthogonal distance from the beam axis. Densities are indicated at distances of 23, 31.5 and 40 mm from the nozzle, corresponding to the top, middle, and bottom sections of the interaction region. The ordinate is based on experimental centertime densities.

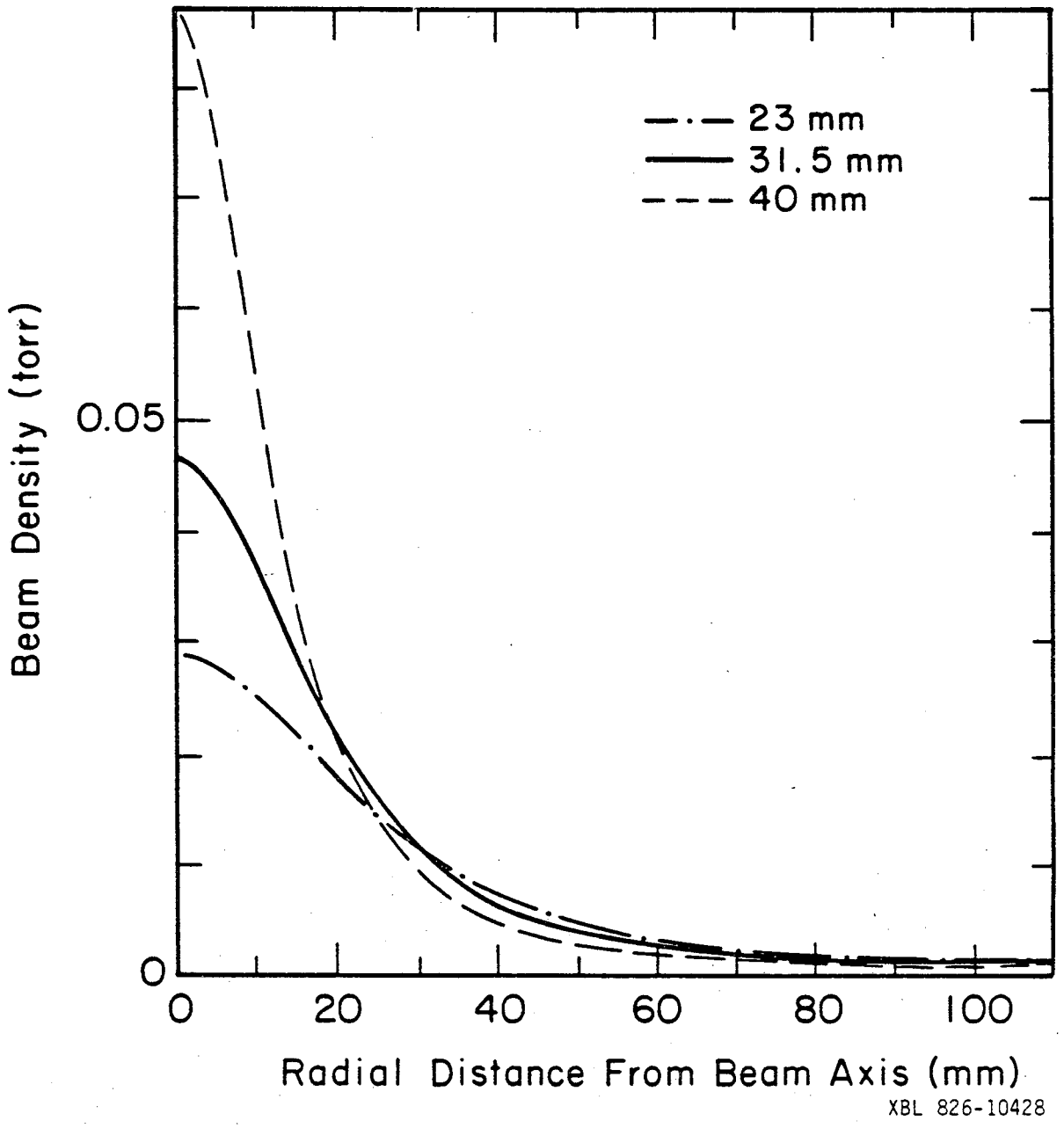
23 mm
31.5 mm
40 mm
Beam Density (torr)
0.05
0
0
20
40
60
80
100
Radial Distance From Beam Axis (mm)
XBL 826-10428

Figure IV-2

Figure IV-3. The absorption cross-section of iron pentacarbonyl in the 900 to 1300 Å region of the vacuum ultraviolet spectrum.

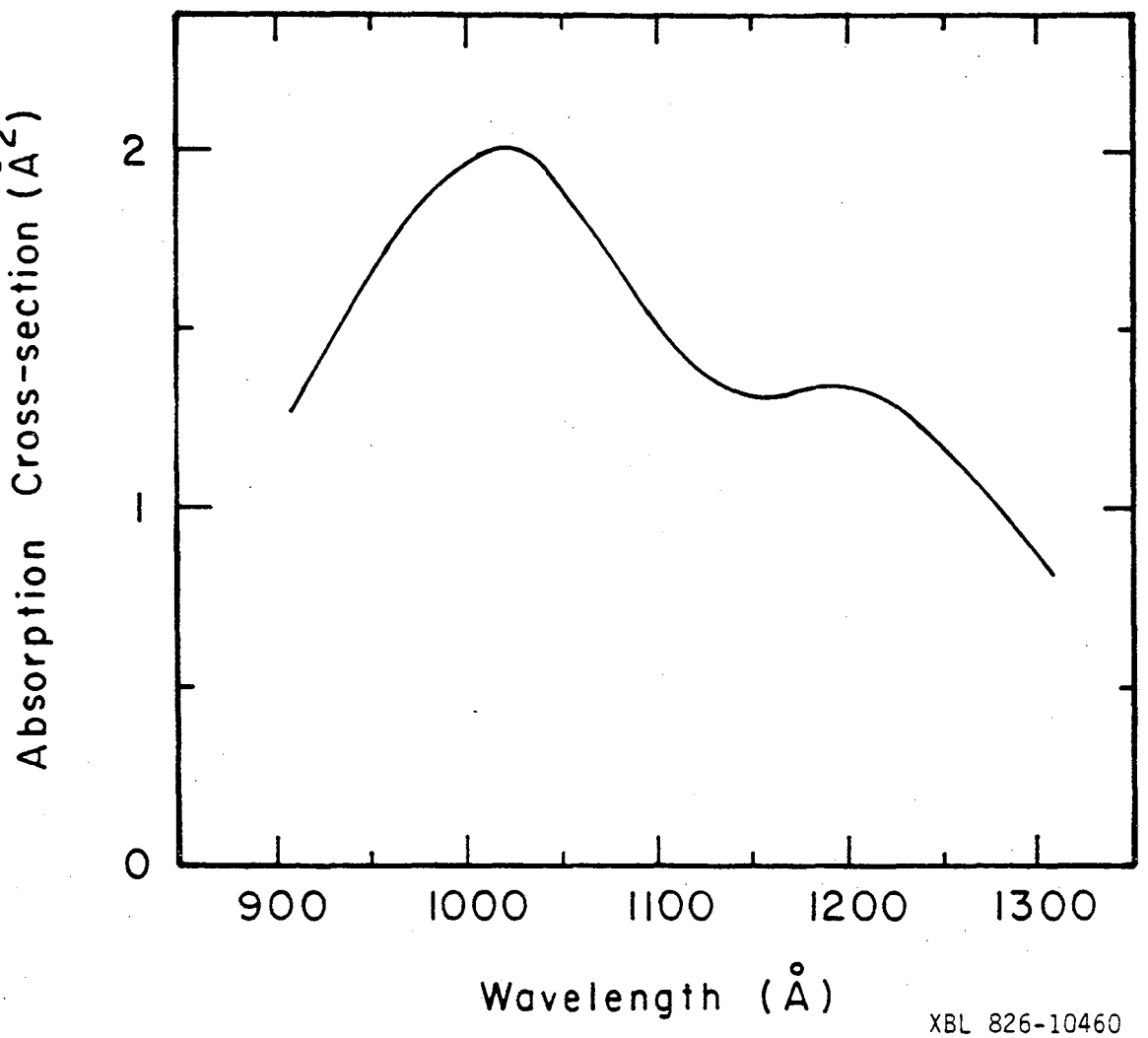
Absorption Cross-section (Å²)
2
1
0
900
1000
1100
1200
1300
Wavelength (Å)
XBL 826-10460

Figure IV-3

Figure IV-4. The relative rates of formation of Fe excited states from VUV photolysis of $Fe(CO)_5$. The data of Hellner, et al., are plotted versus the energy of the emitting state. The solid and dashed curves are the predictions of the all and the limited active degrees of freedom statistical dissociation models, respectively.

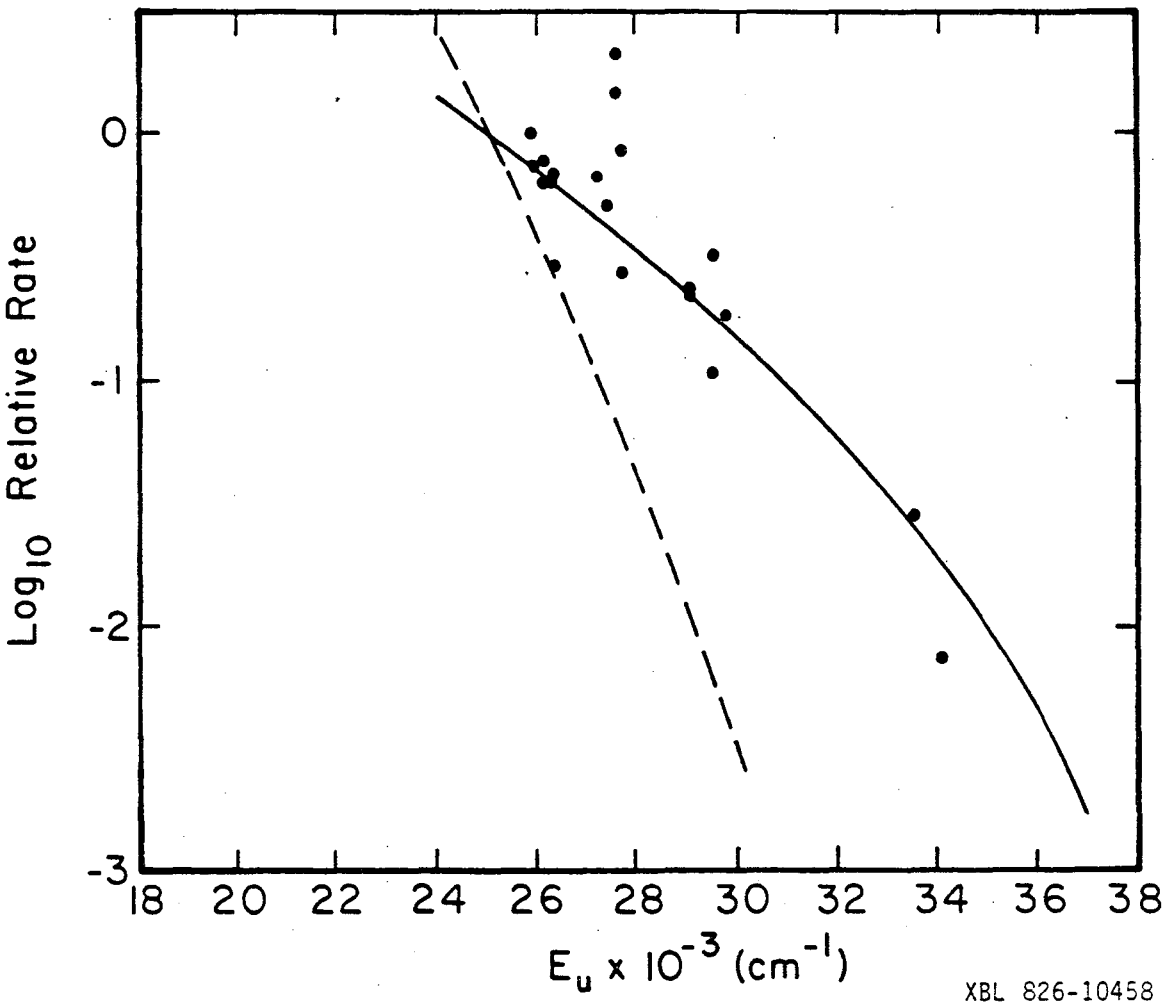
Log10 Relative Rate
0
-1
-2
-3
18
20
22
24
26
28
30
32
34
36
38
Eu x 10-3 (cm-1)
XBL 826-10458

Figure IV-4

Figure IV-5. A simulated iron emission spectrum from VUV photolysis of $Fe(CO)_5$ using 11.8 eV photons. The limited degrees of freedom statistical dissociation model was used.

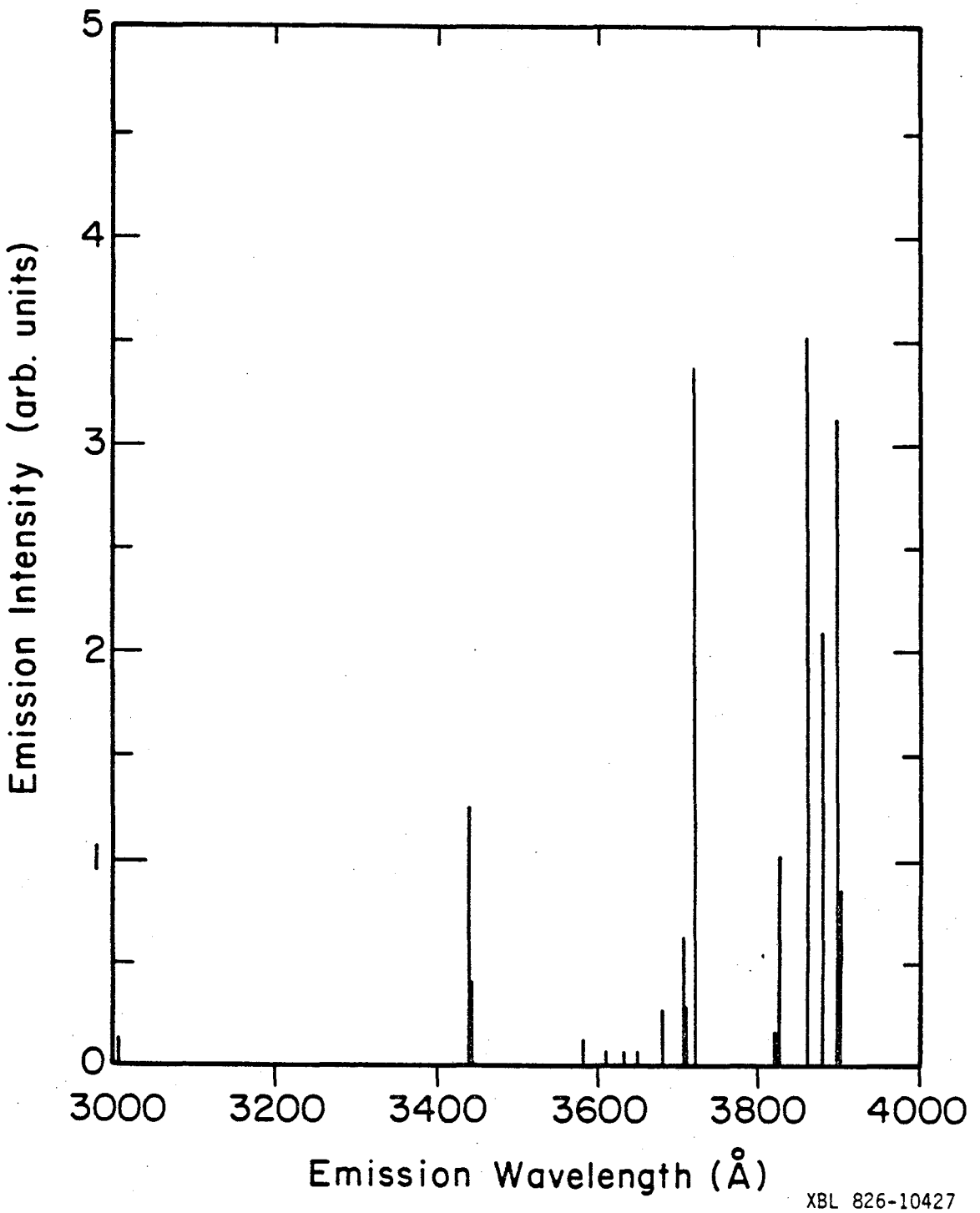
Emission Intensity (arb. units)
0
1
2
3
4
5
3000
3200
3400
3600
3800
4000
Emission Wavelength (Å)
XBL 826-10427

Figure IV-5

Figure IV-6. A simulated iron emission spectrum from VUV photolysis of $Fe(CO)_5$ using 16.7 eV photons. The limited degrees of freedom statistical dissociation model was used.

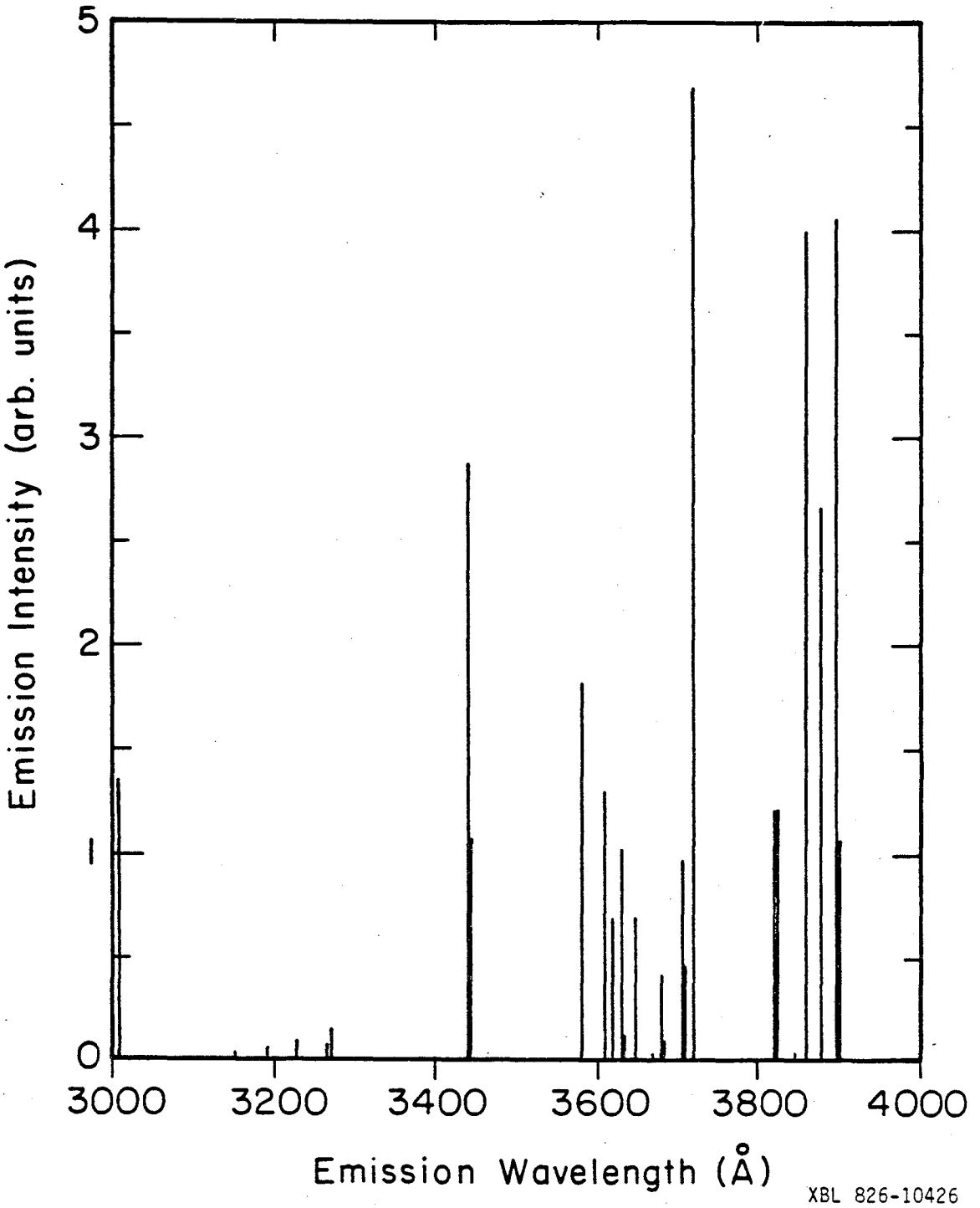
Emission Intensity (arb. units)
0
1
2
3
4
5
3000
3200
3400
3600
3800
4000
Emission Wavelength (Å)
XBL 826-10426

Figure IV-6

Figure IV-7. A simulated iron emission spectrum from VUV photolysis of $Fe(CO)_5$ using 11.8 eV photons and corrected for experimental monochromator band pass. The limited degrees of freedom statistical dissociation model was used.

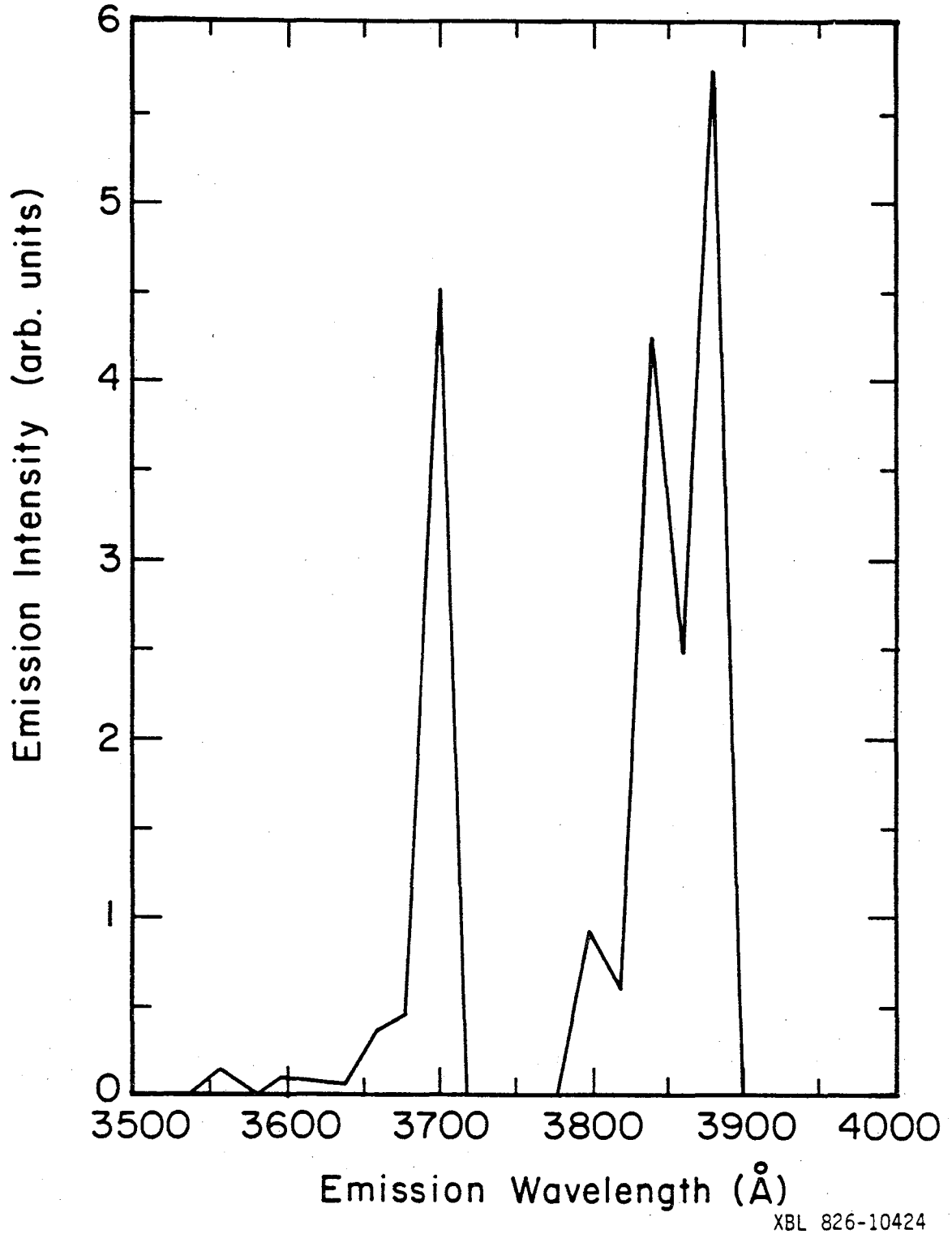
Emission Intensity (arb. units)
0
1
2
3
4
5
6
3500
3600
3700
3800
3900
4000
Emission Wavelength (Å)
XBL 826-10424

Figure IV-7

Figure IV-8. A simulated iron emission spectrum from VUV photolysis of $Fe(CO)_5$ using 16.7 eV photons and corrected for experimental monochromator band pass. The limited degrees of freedom statistical dissociation model was used.

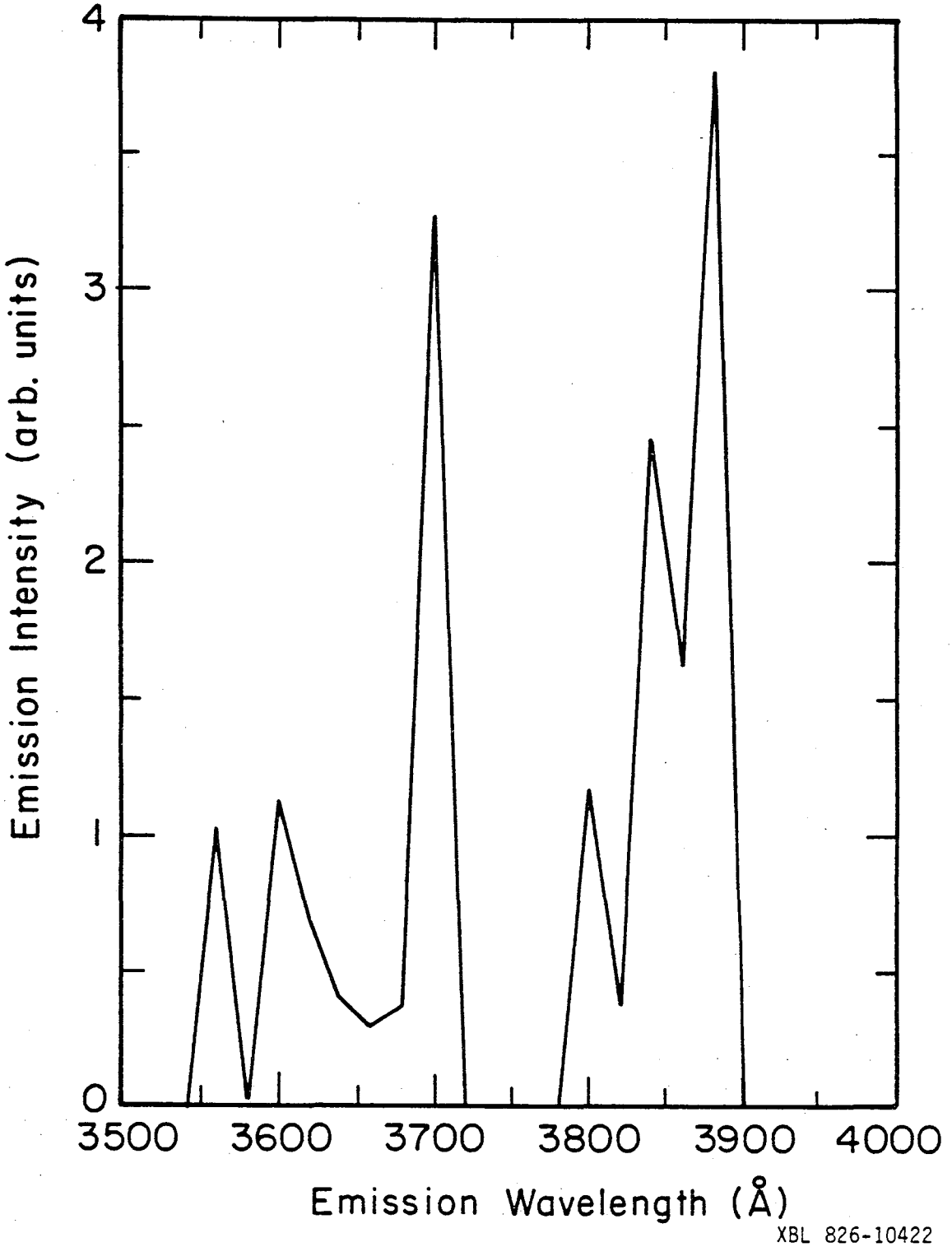
Emission Intensity (arb. units)
0
1
2
3
4
3500
3600
3700
3800
3900
4000
Emission Wavelength (Å)
XBL 826-10422

Figure IV-8

Figure IV-9. The manufacturer's fractional quantum efficiency of the RCA C31034 photomultiplier.

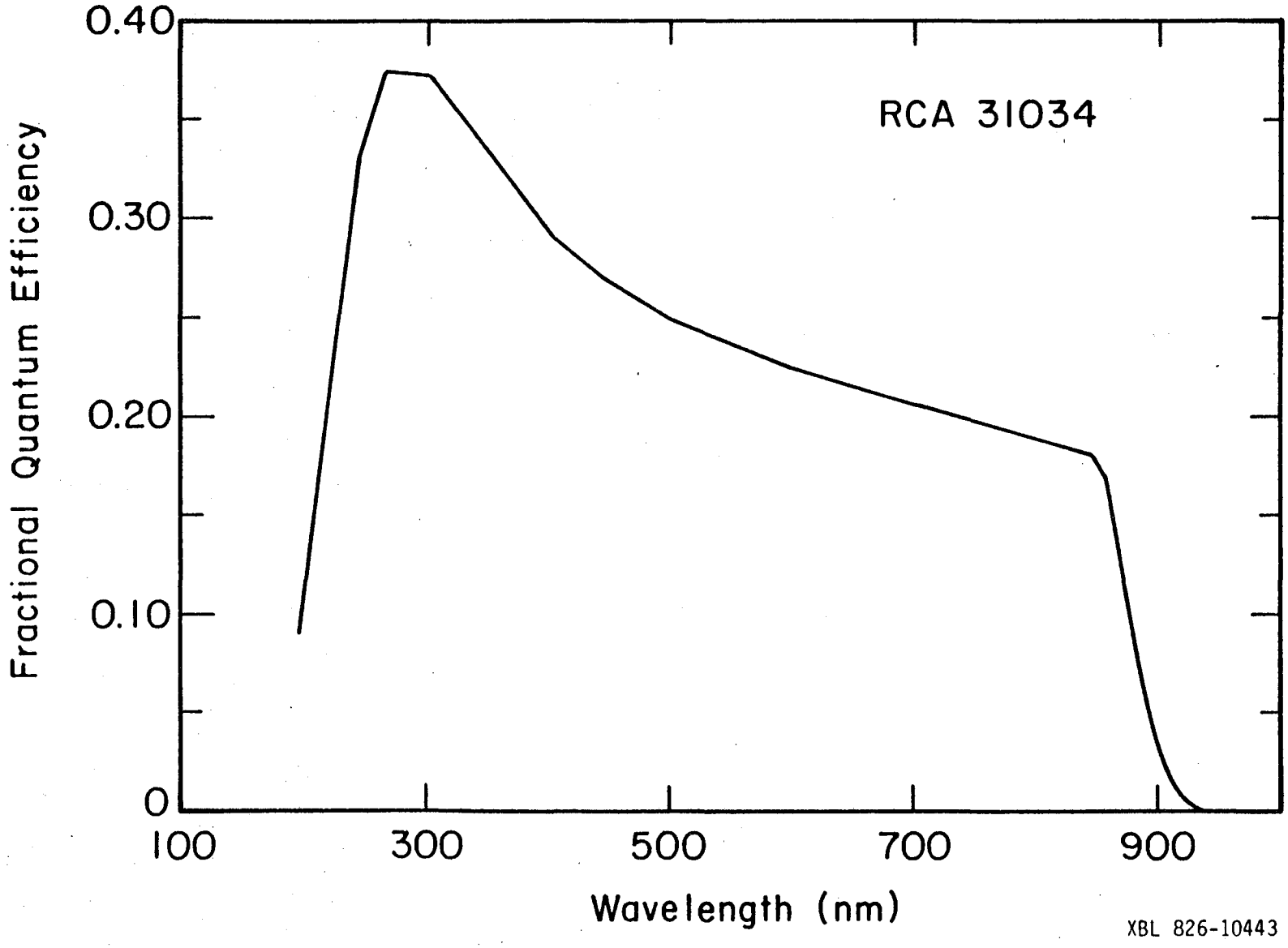
RCA 31034
Fractional Quantum Efficiency
0.40
0.30
0.20
0.10
0
100
300
500
700
900
Wavelength (nm)
XBL 826-10443

Figure IV-9

Figure IV-10. The absolute simulated branching ratio between neutral production and detectable fluorescence corrected for photomultiplier response plotted as a function of the VUV photon energy. Numbers indicate the values of E_d used in the simulation.

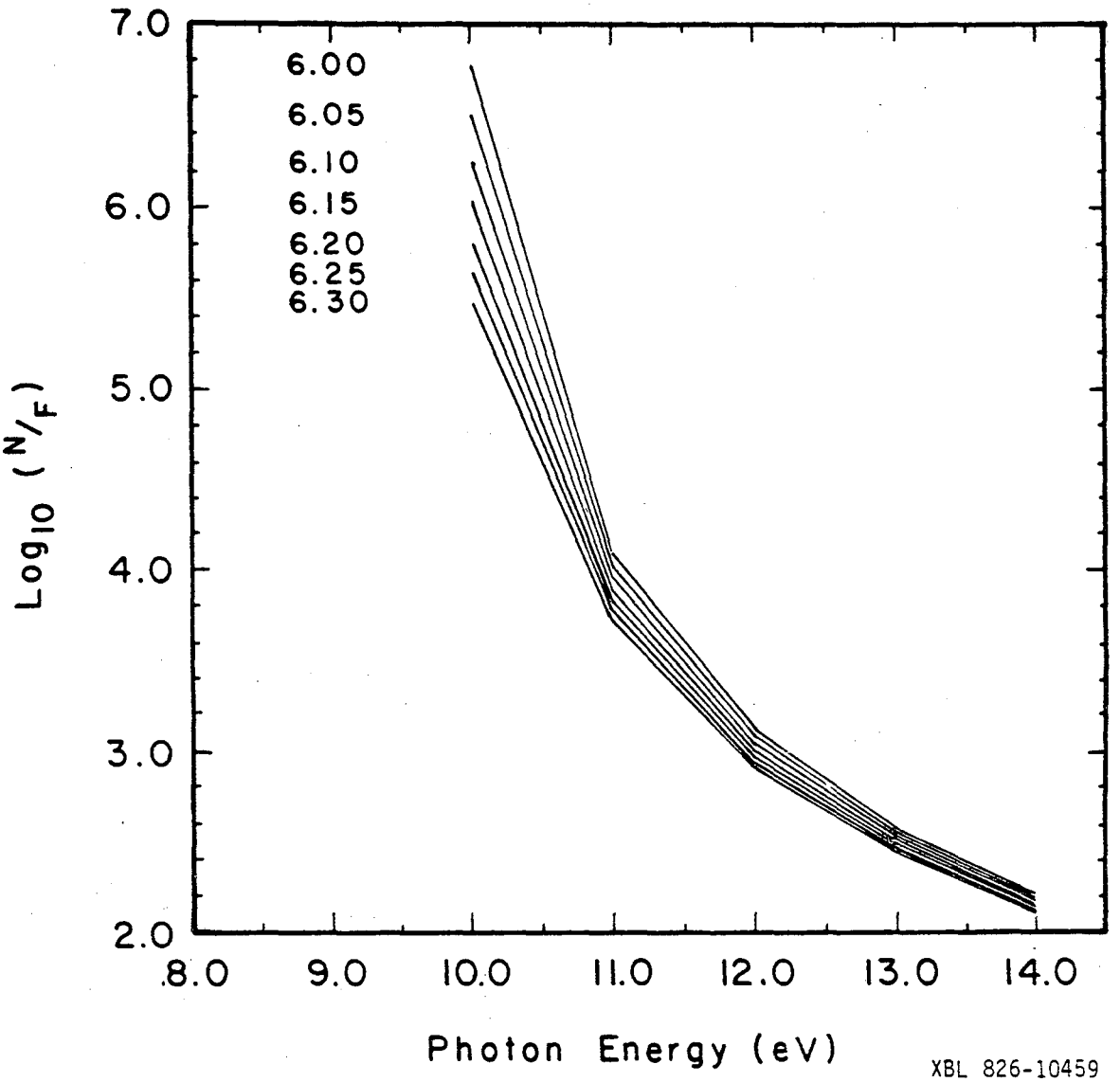
7.0
6.0
5.0
4.0
3.0
2.0
6.00
6.05
6.10
6.15
6.20
6.25
6.30
Log10 (N/F)
8.0
9.0
10.0
11.0
12.0
13.0
14.0
Photon Energy (eV)
XBL 826-10459

Figure IV-10

Figure IV-11. The difference between the $\log_{10}$ values of interpolated experimental quantum fluorescence yield and the $\log_{10}$ value of PMT corrected detectable fluorescence as a fraction of the total neutral production plotted as a function of the VUV photon energy. The individual curves are labelled according to the E_d values used in the simulation.

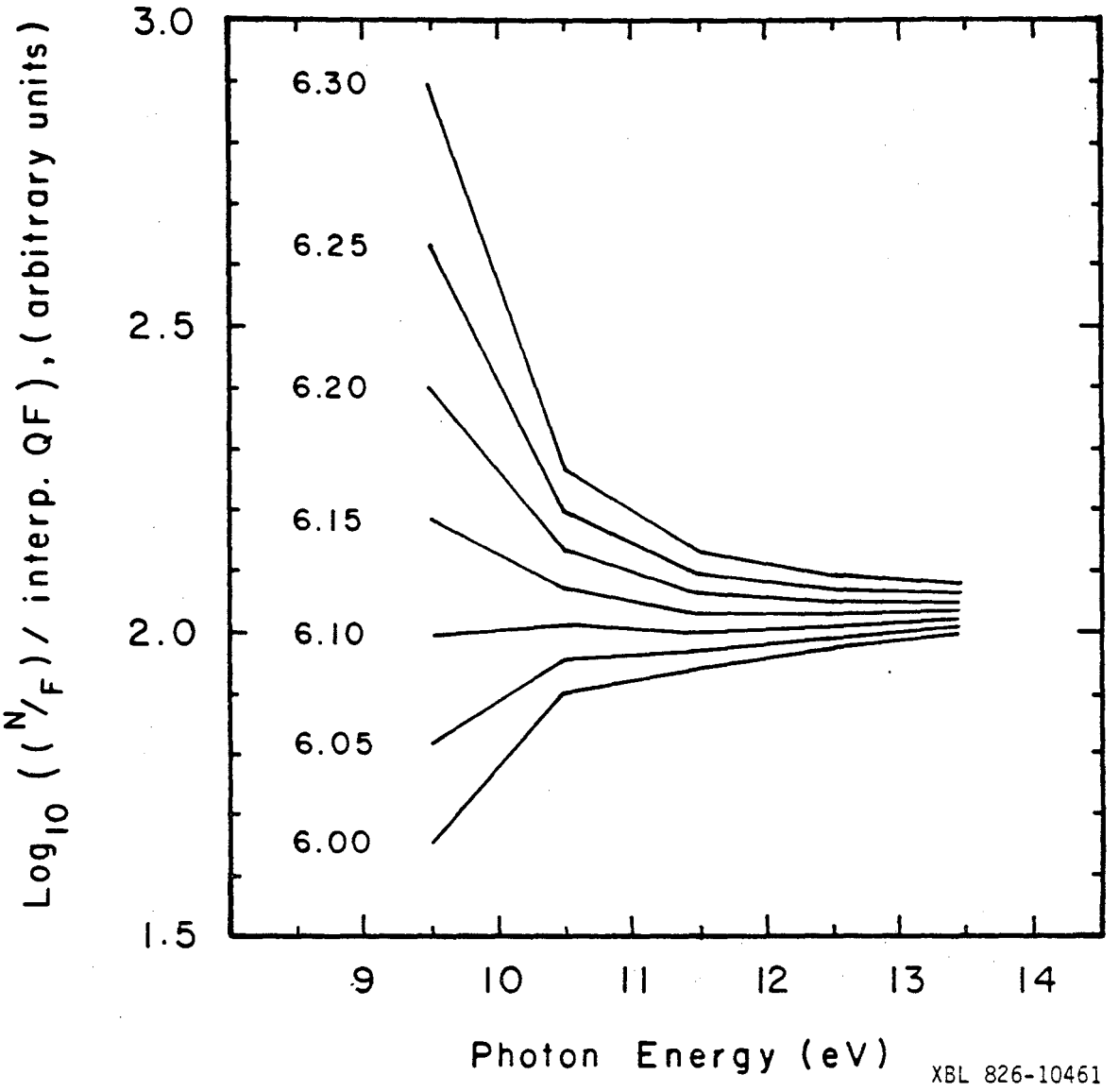
3.0
2.5
2.0
1.5
6.30
6.25
6.20
6.15
6.10
6.05
6.00
9
10
11
12
13
14
Log10 ((N/F) / interp. QF), (arbitrary units)
Photon Energy (eV)
XBL 826-10461

Figure IV-11

Figure IV-12. The comparison of the experimental quantum fluorescence yield (curve A) with the interpolated quantum fluorescence yield (curve B) plotted as a function of photon energy. The dashed part of curve B indicates extrapolation to coincide with the neon excited data points.

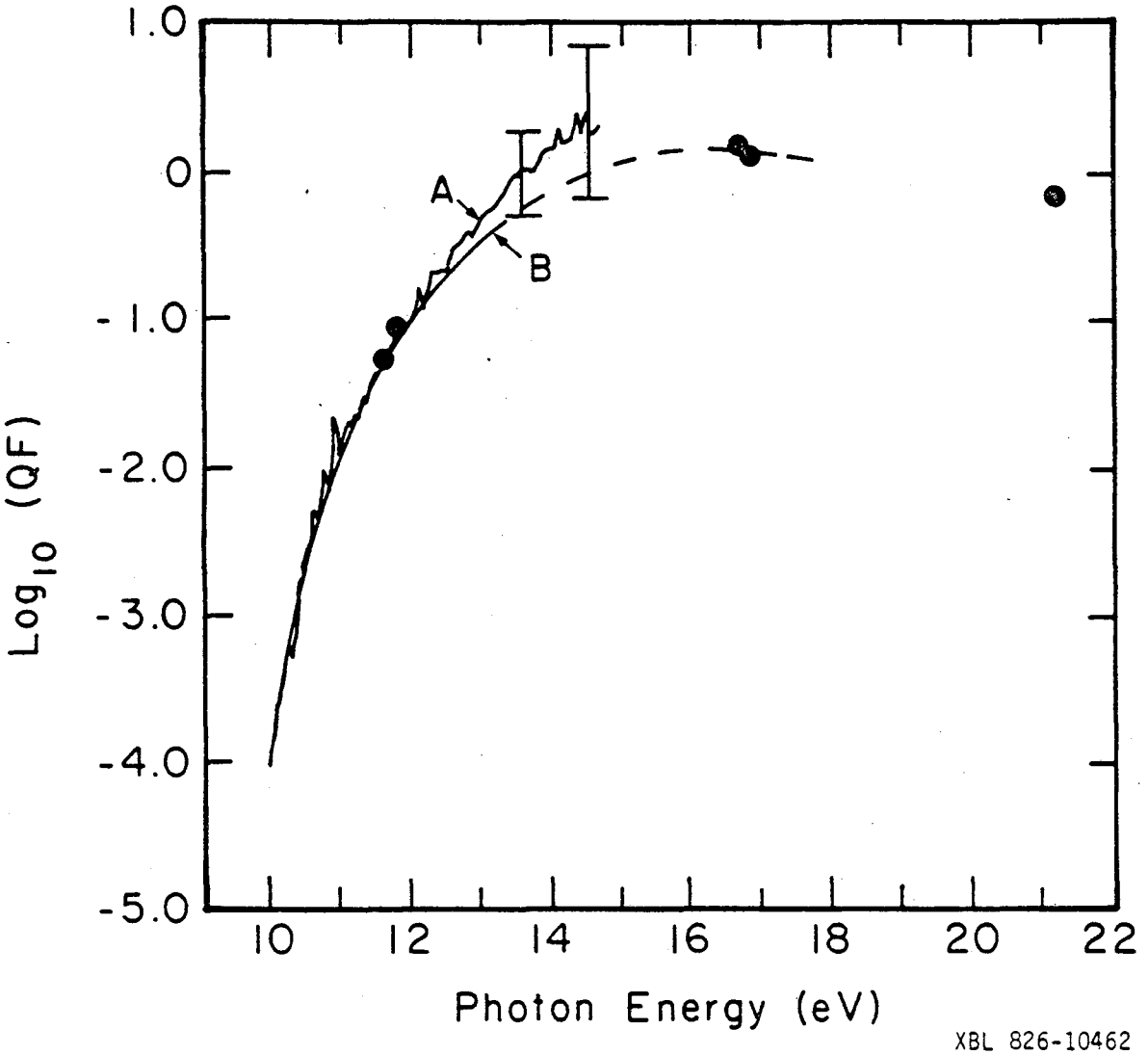
1.0
0
-1.0
-2.0
-3.0
-4.0
-5.0
Log10 (QF)
A
B
10
12
14
16
18
20
22
Photon Energy (eV)
XBL 826-10462

Figure IV-12

Figure IV-13. The comparison of the interpolated quantum fluorescence yield (curve C) with the theoretical quantum fluorescence yield curves using all (curve B) and limited (curve A) degrees of freedom active.

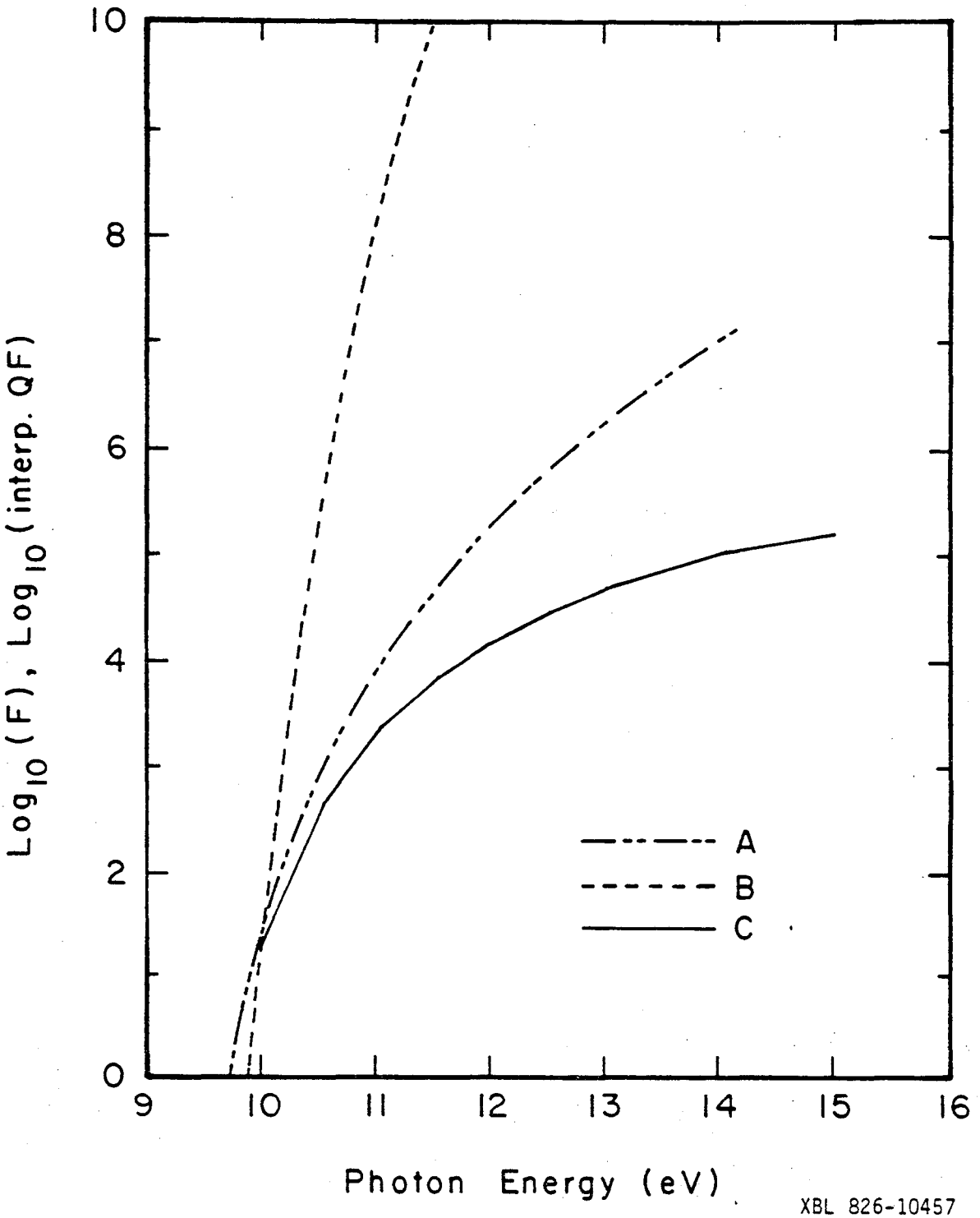
10
8
6
4
2
0
9
10
11
12
13
14
15
16
Log10 (F), Log10 (interp. QF)
Photon Energy (eV)
A
B
C
XBL 826-10457

Figure IV-13

Figure IV-14. The comparison between the experimental photoionization yield (o), and the difference between the interpolated quantum fluorescence yield and the theoretical quantum fluorescence yield plotted as a function of the VUV photon energy. The model used the limited degrees of freedom model with values of E_d indicated (in eV) for each theoretical curve.

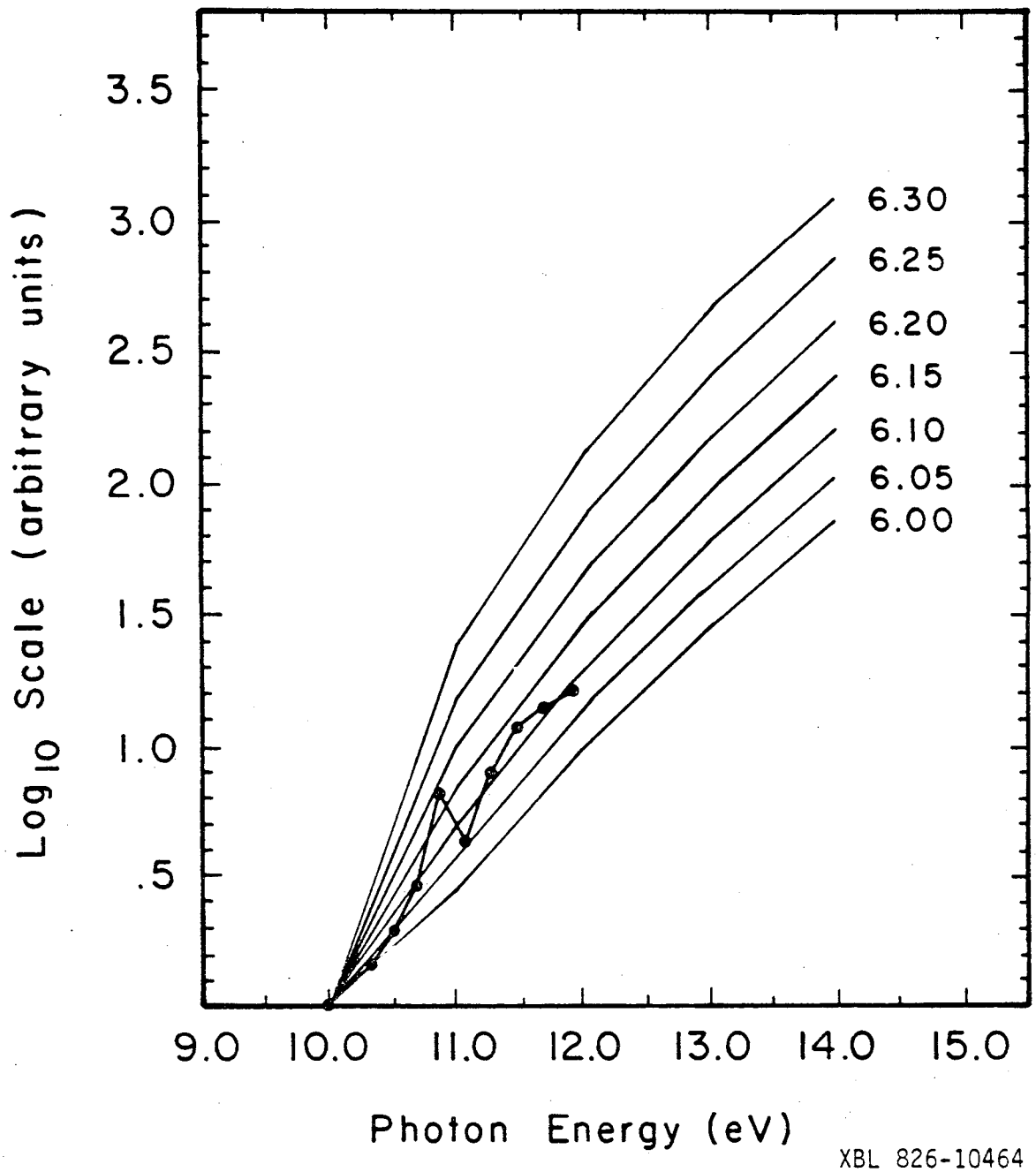
3.5
3.0
2.5
2.0
1.5
1.0
.5
Log10 Scale (arbitrary units)
6.30
6.25
6.20
6.15
6.10
6.05
6.00
9.0
10.0
11.0
12.0
13.0
14.0
15.0
Photon Energy (eV)
XBL 826-10464

Figure IV-14

APPENDIX I

This appendix contains a listing of the program used in data acquisition. It is designed to run on a PET 2001 8K microcomputer using the Commodore 2.0 BASIC operating system. In addition to the computer, the two interfaces described in the text are necessary for operation.

```
1 POKE  59459,255
5 Z5=65535:Z6=256
10 A2=28722:A5=28725:A6=28726
15 B8=18:B0=0:B9=19:B6=16:B5=255
20 AI=0:BI=0
25 I=0:J=0:Q=0:RD=0:NX=0:NY=0:DJ=0
30 XM=0:YM=0
35 DIM CN%(18)
40 DIM A( 90,1),B( 90,1),C(30),D$(4)
45 D$(0)="TITLE":D$(1)="H2 LAMP":D$(3)="FLUORESC MONOCH"
46 D$(4)="DATE"
50 GOSUB6000
55 FORI=826TO848:READJ:POKEI,J:NEXT
60 DATA173,2,2,133,1,96,169,4,208,2,169,0,24,101,1,133,1,205,2,2,208,251,96
90 GOTO1000
100 INPUT"IS DATA CLEARED AND SCAN CONDITIONS OK  ";A$
101 IF(A$<>"Y")THEN  RETURN
103 POKE59471,32
104 PRINT"TO START GATHERING DATA - PRESS ANY KEY"
110 POKE28723,146:POKE28722,0:POKE28727,48:POKE28727,112:POKE28727,176
120 POKE28722,16
130 POKE28725,255:POKE28725,255
140 POKE28726,255:POKE28726,255
145 AI=0:BI=0
200 L=0:I=-1
210 YM=0:NX=0:YM=0:NY=0
220 C2%=0:PR=0
240 C1%=CN%(L)
245 GETA$:IF(A$="")THEN245
250 SYS(826)
```

```
260 K=C1%AND32:POKE59471,K
280 POKEA2,B8:POKEA2,B0
282 AI=AI+Z5-XM*Z6-NX
284 BI=BI+Z5-YM*Z6-NY
286 PRINTM;PR;I;RR,AI,BI
290 K=K/32
300 IF(PR=0)THEN360
320 A(I,M)=A(I,M)+AI
340 B(I,M)=B(I,M)+BI
360 AI=0:BI=0
365 PR=(C1%AND64)/64
370 IF(C1%AND128)<>0THENL=-1
372 IF(L<>0)THEN380
375 I=I+1
376 PRINT
377 GETA$:IF(A$<>"")THEN950
378 PRINT"BM PR CH CMD          SCINT     FLUO"
380 M=K
400 C2%=C1%
420 SYS(836)
425 FOR RR=(C2%AND31)-1TO1STEP-1
440 POKEA2,B9
460 NX=PEEK(A5):XM=PEEK(A5)
480 NY=PEEK(A6):YM=PEEK(A6)
500 POKEA2,B6
520 POKEA5,B5:POKEA5,B5
540 POKEA6,B5:POKEA6,B5
560 SYS(832)
580 POKEA2,B8:POKEA2,B0
600 AI=AI+Z5-XM*Z6-NX
```

```
620 BI=BI+Z5-YM*Z6-NY
640 PRINTM;PR;I;RR,AI,BI
660 SYS(836)
680 NEXT
683 POKEA2,B9
686 NX=PEEK(A5):XM=PEEK(A5)
689 NY=PEEK(A6):YM=PEEK(A6)
692 POKEA2,B6
695 POKEA5,B5:POKEA5,B5
698 POKEA6,B5:POKEA6,B5
700 L=L+1
720 C1%=CN%(L)
730 SYS(832)
740 GOTO260
950 C(3)=0:C(4)=I-1:CS=I-1
1000 TI$="000000":Q=0:FL=0
1002 PRINT:PRINT
1004 PRINTCHR$(145);"ENTER COMMAND (?-HELP)":Q=Q+20
1006 GETCC$
1007 IF(CC$<>"")THEN1020
1008 IF(TI<Q)GOTO1006
1010 PRINTCHR$(145);"■ENTER COMMAND (?-HELP)■":Q=Q+20
1012 GET  CC$
1013 IF(CC$<>"")GOTO1020
1014 IF(TI<Q)GOTO1012
1015 GOTO1004
1020 IF(CC$="R")THENFL=1:GOSUB100
1025 IF(CC$="0")THENPOKE  59471,0:GOTO1000
1026 IF(CC$="1")THENPOKE 59471,32:GOTO1000
1030 IF(CC$="S")THENFL=1:GOSUB2000
```

```
1040 IF(CC$="D")THENFL=1:GOSUB3000
1050 IF(CC$="W")THENFL=1:GOSUB4000
1060 IF(CC$="A")THENFL=1:GOSUB5000
1070 IF(CC$="L")THENFL=1:GOSUB6000
1080 IF(CC$="C")THENFL=1:GOSUB7000
1090 IF(CC$="?")THENFL=1:GOSUB8000
1100 IF(FL=0)THEN PRINT"COMMAND >";CC$;"< IS NOT DECODABLE"
1110 GOTO1000
2000 REM SETUP
2040 INPUT"ENTER ■D■WELLTIME/CH - ■A■NGSTROMS/CH - ■E■ND";A$
2050 IF(A$="E")THENRETURN
2060 IF(A$<>"A"ANDA$<>"D")THEN2040
2070 C(23)=7:SS=0
2080 IF(A$="D")THEN INPUT"ENTER DWELL TIME(SEC/CH)";DT:AC=0
2095 IF(A$="A")THENINPUT"ENTER SCAN SPEED(A/MIN)";SS:C(23)=SS
2100 IF(A$="A")THEN INPUT"ENTER ANGSTROMS/CH";AC:DT=AC/SS*60
2110 GOSUB9000
2120 DJ=DT*60
2140 SJ=DJ/NS
2160 RD=SJ-4
2219 IF(RD<>INT(RD))THENPRINT"■ERROR DWELL";RD;"IS NONINTEGER":PRINT:GOTO2040
2220 IF(RD<20)THEN PRINT"■ERROR DWELL=";RD;"< 20 REDO■":PRINT:GOTO2040
2221 IF(RD>255)THEN PRINT"■ERROR DWELL=";RD;"> 255 REDO■":PRINT:GOTO2040
2230 POKE837,RD
2240 PRINT:PRINT"■PRESENT SCAN CONDITIONS■"
2250 PRINT
2260 PRINT"■ANGSTROMS/CH >■";AC
2280 PRINT"■DWELL TIME/CHANNEL■";DT;"■SEC■"
2300 PRINT"■SCANS PER CHANNEL■";NS
2320 PRINT"■REAL DWELL PER SCAN■";RD/60;"■SEC■"
```

```
2321 PRINT"                              ";RD;"JIFFIES"
2340 PRINT:INPUT"ARE THESE SCAN CONDITIONS OK (Y/N)";A$
2360 IF(A$="N")THEN2040
2380 C(2)=DT
2390 C(1)=NS
2395 C(8)=NS*RD/60
2400 C(7)=AC
2420 INPUT"ENTER STARTING WAVELENGTH";SW:C(22)=SW
2950 RETURN
3000 REM DISPLAY
3200 FOR I=0TOCS
3210 PRINT I;A(I,0);A(I,1);B(I,0);B(I,1)
3250 GETA$
3260 IF(A$="")THEN3400
3270 GETA$
3280 IF(A$="")THEN3270
3400 NEXT
3950 RETURN
4000 REM FORMATTED TAPE OUTPUT
4005 FOR K=0TO3
4009 OPEN 1,1,1
4010 IF(K=0)THEN PRINT#1,"RAW FLUORESCENCE BEAM-OFF"
4012 IF(K=1)THEN PRINT#1,"RAW SCINTILLATOR BEAM-OFF"
4014 IF(K=2)THEN PRINT#1,"RAW FLUORESCENCE BEAM-ON"
4016 IF(K=3)THEN PRINT#1,"RAW SCINTILLATOR BEAM-ON"
4019 FOR I=1 TO 4
4020 PRINT#1,D$(I)
4030 NEXT
4040 FOR I=0 TO 7
4050 PRINT#1,C(I)
```

```
4060 NEXT
4062 IFK<=1THEN PRINT#1,C(8)*B0/NS:PRINT#1,B0
4064 IFK>1THEN PRINT#1,C(8)*B1/NS:PRINT#1,B1
4066 FOR I=10TO30
4067 PRINT#1,C(I)
4068 NEXT
4070 FOR I=0 TO CS
4080 IF(K=0)THEN PRINT#1,B(I,0)
4081 IF(K=1)THEN PRINT#1,A(I,0)
4082 IF(K=2)THEN PRINT#1,B(I,1)
4083 IF(K=3)THEN PRINT#1,A(I,1)
4090 NEXT
4100 CLOSE1
4200 NEXT
4950 RETURN
5000 REM ACQUIRE
5001 POKE28723,146:POKE28722,0:POKE28727,40:POKE28727,112:POKE28727,176
5002 POKE59471,0:B$="OFF"
5010 POKE28722,16
5020 POKE28725,255:POKE28725,255
5030 POKE28726,255:POKE28726,255
5040 Q=TI
5100 POKE A2,B8:POKE A2,B0
5110 IF(Q+60>TI)THEN5110
5120 POKE A2,B9
5130 NX=PEEK(A5):XM=PEEK(A5)
5140 NY=PEEK(A6):YM=PEEK(A6)
5150 AI=Z5-XM*Z6-NX
5160 BI=Z5-YM*Z6-NY
5170 PRINT AI,BI,"BEAM ";B$
```

```
5180 GET A$
5185 IF(A$="1")THEN POKE59471,32:B$="ON":GOTO5200
5190 IF(A$="0")THEN POKE59471,0:B$="OFF":GOTO5200
5195 IF(A$<>"")THEN1000
5200 POKEA2,B6
5210 POKEA5,B5:POKEA5,B5
5220 POKEA6,B5:POKEA6,B5
5500 GOTO5040
6000 REM TIMING SEQUENCE
6001 PRINT"ENTER TIMING SEQUENCE"
6010 D$(2)=""
6020 FOR I=0TO20
6030 PRINT"INPUT COMMAND #";I
6040 INPUT CN%(I)
6045 D$(2)=D$(2)+STR$(CN%(I))
6050 IF(CN%(I)AND128)=128THEN 6100
6060 NEXT
6100 RETURN
7000 REM INTERNAL DATA CLEAR
7001 INPUT"WOULD YOU LIKE DATA CLEARED(■Y■/■N■)";CC$
7010 IF(CC$<>"Y")THEN7300
7020 FOR I=0 TO 80
7030 A(I,0)=0:A(I,1)=0
7040 B(I,0)=0:B(I,1)=0
7050 NEXT
7060 PRINT:PRINT"■DATA CLEARED■"
7500 RETURN
8000 PRINT"■R■UN ■S■ET-UP ■A■CTIVATE ■D■ISPLAY ■W■RITE"
8010 PRINT"■L■OAD ■C■LEAR"
8070 RETURN
```

```
9000 B1=0:B0=0:NS=0
9010 FOR I=0TO20
9013 IF((CN%(I)AND96)=96)THEN B1=B1+(CN%(I)AND31)
9015 IF((CN%(I)AND96)=64)THEN B0=B0+(CN%(I)AND31)
9020 NS=NS+(CN%(I)AND31)
9025 IF((CN%(I)AND128)=128)THEN9050
9030 NEXT
9050 RETURN
10000 END
```

APPENDIX II

In order to determine the variable m used in Equation (IV-23) which corrects for anharmonicity, the following procedure was implemented. The CO vibrational constants given by Herzberg[a] were used to calculate the vibrational energies. The density of states, $\rho(E)$, at the energy between two vibrational levels was taken as simply the reciprocal of the energy difference between these two levels. To scale $\rho(E)$ into a range of more convenient magnitude, the results were multiplied by 2500 so that $\rho(E)$ was defined as the number of vibrational states per 2500 cm^{-1}. The results are shown in Table AII-1, column 4.

A simple expression for $\rho_v(E)$ that was found to work well was

$$\rho_v(E) = be^{mE} \qquad \text{(AII-1)}$$

The numerical $\rho_v(E)$ from calculations above were least squares fitted to Equation (AII-1) and the results are shown in Table AII-1, columns 5-8. Since all the energetically accessible quintet iron states were included in the simulation, the value of m used depended on the maximum amount of energy available for deposition into a CO bond, i.e., E_u. It was found that the model calculations were very insensitive to the inclusion of anharmonicity. Physically, this is due to the large vibrational spacing in CO and the relatively little average amount of vibrational energy deposited in the CO bond. Nevertheless, all calculations reported here were done taking anharmonicity into account.

---

[a] K. P. Huber and G. H. Herzberg, Constants of Diatomic Molecules (Van Nostrand Reinhold Co., New York, 1979).

Table AII-1

Data in Table are for $X^1\Sigma^+$ State of CO

v	E	E_M	$\rho_v(E)$	R^2	b	m $\frac{1}{cm^{-1}} \times 10^{+6}$	m $\frac{1}{eV}$
0	0	1071.7	1.166				
1	2143.3	3201.7	1.181	1.0000	1.1585	6.0011	.048402
2	4260.0	5305.2	1.196	1.0000	1.1585	6.0006	.048398
3	6350.4	7382.5	1.211	1.0000	1.1585	6.0004	.048396
4	8414.5	9433.4	1.227	.9998	1.1582	6.0782	.049024
5	10452.2	11458.0	1.243	.9997	1.1579	6.1452	.049564
6	12463.8	13456.5	1.259	.9997	1.1577	6.1956	.049970
7	14449.2	15428.9	1.276	.9996	1.1573	6.2648	.050528
8	16408.5	17375.2	1.293	.9994	1.1568	6.3312	.051064
9	18341.9	19295.7	1.311	.9992	1.1562	6.4096	.051697
10	20249.4	21190.2	1.329	.9990	1.1556	6.4863	.052315
11	22131.0	23054.0	1.340	.9991	1.1558	6.4588	.052094
12	23986.9	24902.0	1.366	.9984	1.1548	6.5599	.05909
13	25817.1	26719.4	1.385	.9979	1.1539	6.6512	.053645
14	27621.7	28511.3	1.405	.9975	1.1528	6.7415	.054374
15	29400.9	30277.8	1.426	.9970	1.1517	6.8351	.055128
16	31154.6	32018.8	1.446	.9967	1.1506	6.9203	.055816
17	32883.0	33734.6	1.468	.9964	1.1494	7.0095	.056535
18	34586.2	34425.2	1.490	.9943	1.1475	7.1481	.057653
19	36264.2	37090.7	1.512	.9944	1.1464	7.2266	.058286
20	37917.1	38731.1	1.536	.9943	1.1450	7.3114	.058970
21	39545.0	40346.5	1.560	.9941	1.1436	7.3985	.059672
22	41148.0	41937.1	1.584	.9934	1.1422	7.4853	.060373
23	42726.2	43502.9	1.609	.9934	1.1406	7.5736	.061085
24	44279.6	45044.0	1.635	.9932	1.1390	7.6642	.061816
25	45808.4	46560.5	1.662	.9927	1.1373	7.7578	.062571
26	47312.5	48052.4	1.690	.9921	1.1354	7.8546	.063351
27	48792.2	49519.8	1.718	.9916	1.1334	7.9524	.064140
28	50247.4	50962.8	1.747	.9909	1.1314	8.0517	.064941
29	51678.2	52381.4	1.778	.9902	1.1292	8.1548	.065772
30	53084.6	53775.7	1.809	.9894	1.1270	8.2596	.066618

Table AII-1 (continued)

v	E	E_M	$\rho_v(E)$	R^2	b	$\frac{m}{\frac{1}{cm^{-1}} \times 10^{+6}}$	$\frac{m}{\frac{1}{eV}}$
31	54466.8	55145.8	1.841	.9886	1.1246	8.3662	.067478
32	55824.8	56491.7	1.874	.9878	1.1221	8.4747	.068353
33	57158.5	57813.4	1.909	.9868	1.1195	8.5865	.069254
34	58468.2	59111.0	1.945	.9858	1.1168	8.7011	.070179
35	59753.7	60384.4	1.982	.9848	1.1140	8.8183	.071124
36	61015.1	61633.8	2.021	.9836	1.1110	8.9388	.072096
37	62252.4	62859.0	2.061	.9824	1.1079	9.0621	.073091
38	63465.6	64060.2	2.102	.9812	1.1046	9.1878	.074104
39	64654.7	65237.3	2.146	.9798	1.1012	9.3174	.075149
40	65819.8	66390.3	2.191	.9784	1.0977	9.4501	.076220
41	66960.7	67519.1	2.239	.9768	1.0940	9.5870	.077324
42	68077.4	68623.6	2.289	.9752	1.0901	9.7280	.078461
43	69169.8	69703.9	2.341	.9735	1.0861	9.8730	.079631
44	70237.9	70759.8	2.395	.9716	1.0819	10.022	.080831
45	71281.7	71791.3	2.453	.9697	1.0775	10.176	.082071
46	72300.9	72798.2	2.514	.9675	1.0729	10.334	.083353
47	73295.5	73780.5	2.578	.9653	1.0681	10.498	.084675
48	74265.4	74737.9	2.646	.9629	1.0631	10.668	.086041
49	75210.3	75670.3	2.718	.9603	1.0578	10.843	.087455
50	76130.3	76577.5	2.795	.9576	1.0523	11.025	.088920
51	77024.8	77459.4	2.877	.9546	1.0466	11.213	.090439
52	77893.9	78315.6	2.965	.95146	1.0406	11.409	.092016
53	78737.2	79145.9	3.058	.94809	1.0343	11.611	.093651
54	79554.6	79950.1	3.161	.9444	1.0278	11.823	.095357
55	80345.6	80727.8	3.271	.9405	1.0209	12.043	.097133
56	81110.0	81478.8	3.390	.9363	1.0137	12.273	.098986
57	81847.5	82202.6	3.520	.9318	1.0061	12.513	.100920
58	82557.7	82898.9	3.664	.9268	0.9981	12.764	.102946
59	83240.1	83567.3	3.821	.9215	0.9898	13.027	.105069

This report was done with support from the Department of Energy. Any conclusions or opinions expressed in this report represent solely those of the author(s) and not necessarily those of The Regents of the University of California, the Lawrence Berkeley Laboratory or the Department of Energy.

Reference to a company or product name does not imply approval or recommendation of the product by the University of California or the U.S. Department of Energy to the exclusion of others that may be suitable.

TECHNICAL INFORMATION DEPARTMENT
LAWRENCE BERKELEY LABORATORY
UNIVERSITY OF CALIFORNIA
BERKELEY, CALIFORNIA 94720